PICOSECOND DEMODULATION AND

COHERENT ELECTRON BEAMS

FINAL REPORT

John Christopher Swartz
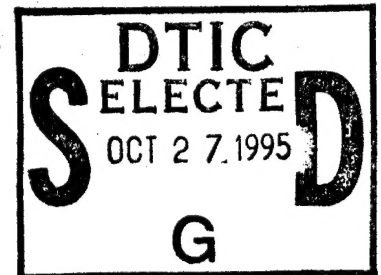
Bob D. Guenther

H. Craig Casey, Jr.

US ARMY RESEARCH OFFICE
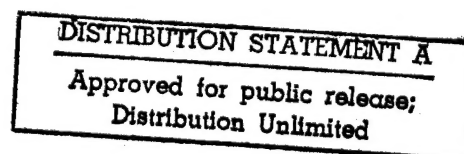
CONTRACT# DAAL03-89-D-0002

DUKE UNIVERSITY

DTIC
SELECTED
OCT 2 7 1995
G

APPROVED FOR PUBLIC RELEASE;
DISTRIBUTION UNLIMITED

19951026 035

DTIC QUALITY INSPECTED 5

REPORT DOCUMENTATION PAGE

1. AGENCY USE ONLY (Leave blank)	2. REPORT DATE	3. REPORT TYPE AND DATES COVERED FINAL REPORT

4. TITLE AND SUBTITLE
PICOSECOND DEMODULATION AND COHERENT ELECTRON BEAMS

5. FUNDING NUMBERS
Contract Number:
DAAL03-89-D-0002

6. AUTHOR(S)
John Christopher Swartz, Bob D. Guenther and
H. Craig Casey, Jr.

7. PERFORMING ORGANIZATION NAME(S) AND ADDRESS(ES)

DUKE UNIVERSITY
Physics Department
Box 90305
Durham, NC 27708-0305

8. PERFORMING ORGANIZATION REPORT NUMBER

9. SPONSORING/MONITORING AGENCY NAME(S) AND ADDRESS(ES)

U.S. Army Research Office
P. O. Box 12211
Research Triangle Park, NC 27709-2211

10. SPONSORING/MONITORING AGENCY REPORT NUMBER

ARO 27556.4-CH

11. SUPPLEMENTARY NOTES
The view, opinions and/or findings contained in this report are those of the author(s) and should not be construed as an official Department of the Army position, policy, or decision, unless so designated by other documentation.

12a. DISTRIBUTION/AVAILABILITY STATEMENT

Approved for public release; distribution unlimited.

12b. DISTRIBUTION CODE

13. ABSTRACT (Maximum 200 words) Fourier theory states that a time domain signal can be represented in the frequency domain with no loss of information. Because of this equivalence, it is possible to make frequency domain measurements on a signal and, using Fourier theory, determine the time domain parameters of the source. These principles form the basis for using frequency domain measurements to characterize the real time operational characteristics of the relativistic electron beam of a free electron laser (FEL). By using a Fourier transform spectrometer (FTS) to measure the millimeter/sub-millimeter spectrum emitted by a pulsed relativistic electron beam, the temporal electron beam pulse duration and shape are characterized. This technique is used to measure a 1.3 picosecond relativistic electron bunch. In addition, we are able to resolve changes in electron bunch characteristics between the beginning and end of a train of bunches. Preliminary work has begun correlating electron pulse shape to FEL optical operation. Finally, variations in the controls of the electron beam system are correlated with changes in the electron bunch measured using the FTS. Unlike other techniques that destructively interact with the electron beam, this technique is totally passive and results in negligible perturbation in the electron bunch; hence this technique can be used for direct real-time non-destructive electron bunch characterization.

14. SUBJECT TERMS
e-beam diagnostics

15. NUMBER OF PAGES
142

16. PRICE CODE

17. SECURITY CLASSIFICATION OF REPORT UNCLASSIFIED	18. SECURITY CLASSIFICATION OF THIS PAGE UNCLASSIFIED	19. SECURITY CLASSIFICATION OF ABSTRACT UNCLASSIFIED	20. LIMITATION OF ABSTRACT UL

GENERAL INSTRUCTIONS FOR COMPLETING SF 298

The Report Documentation Page (RDP) is used in announcing and cataloging reports. It is important that this information be consistent with the rest of the report, particularly the cover and title page. Instructions for filling in each block of the form follow. It is important to *stay within the lines* to meet *optical scanning requirements*.

Block 1. Agency Use Only *(Leave blank)*.

Block 2. Report Date. Full publication date including day, month, and year, if available (e.g. 1 Jan 88). Must cite at least the year.

Block 3. Type of Report and Dates Covered. State whether report is interim, final, etc. If applicable, enter inclusive report dates (e.g. 10 Jun 87 - 30 Jun 88).

Block 4. Title and Subtitle. A title is taken from the part of the report that provides the most meaningful and complete information. When a report is prepared in more than one volume, repeat the primary title, add volume number, and include subtitle for the specific volume. On classified documents enter the title classification in parentheses.

Block 5. Funding Numbers. To include contract and grant numbers; may include program element number(s), project number(s), task number(s), and work unit number(s). Use the following labels:

C	-	Contract	**PR** - Project	
G	-	Grant	**TA** - Task	
PE	-	Program Element	**WU** - Work Unit Accession No.	

Block 6. Author(s). Name(s) of person(s) responsible for writing the report, performing the research, or credited with the content of the report. If editor or compiler, this should follow the name(s).

Block 7. Performing Organization Name(s) and Address(es). Self-explanatory.

Block 8. Performing Organization Report Number. Enter the unique alphanumeric report number(s) assigned by the organization performing the report.

Block 9. Sponsoring/Monitoring Agency Name(s) and Address(es). Self-explanatory.

Block 10. Sponsoring/Monitoring Agency Report Number. *(If known)*

Block 11. Supplementary Notes. Enter information not included elsewhere such as: Prepared in cooperation with...; Trans. of...; To be published in.... When a report is revised, include a statement whether the new report supersedes or supplements the older report.

Block 12a. Distribution/Availability Statement. Denotes public availability or limitations. Cite any availability to the public. Enter additional limitations or special markings in all capitals (e.g. NOFORN, REL, ITAR).

DOD - See DoDD 5230.24, "Distribution Statements on Technical Documents."
DOE - See authorities.
NASA - See Handbook NHB 2200.2.
NTIS - Leave blank.

Block 12b. Distribution Code.

DOD - Leave blank.
DOE - Enter DOE distribution categories from the Standard Distribution for Unclassified Scientific and Technical Reports.
NASA - Leave blank.
NTIS - Leave blank.

Block 13. Abstract. Include a brief *(Maximum 200 words)* factual summary of the most significant information contained in the report.

Block 14. Subject Terms. Keywords or phrases identifying major subjects in the report.

Block 15. Number of Pages. Enter the total number of pages.

Block 16. Price Code. Enter appropriate price code *(NTIS only)*.

Blocks 17. - 19. Security Classifications. Self-explanatory. Enter U.S. Security Classification in accordance with U.S. Security Regulations (i.e., UNCLASSIFIED). If form contains classified information, stamp classification on the top and bottom of the page.

Block 20. Limitation of Abstract. This block must be completed to assign a limitation to the abstract. Enter either UL (unlimited) or SAR (same as report). An entry in this block is necessary if the abstract is to be limited. If blank, the abstract is assumed to be unlimited.

PICOSECOND DEMODULATION AND

COHERENT ELECTRON BEAMS

FINAL REPORT

John Christopher Swartz

Bob D. Guenther

H. Craig Casey, Jr.

Accesion For		
NTIS CRA&I		X
DTIC TAB		☐
Unannounced		☐
Justification		
By		
Distribution /		
Availability Codes		
Dist	Avail and / or Special	
A-1		

Abstract

Fourier theory states that a time domain signal can be represented in the frequency domain with no loss of information. Because of this equivalence, it is possible to make frequency domain measurements on a signal and, using Fourier theory, determine the time domain parameters of the source. These principles form the basis for using frequency domain measurements to characterize the real time operational characteristics of the relativistic electron beam of a free electron laser (FEL). By using a Fourier transform spectrometer (FTS) to measure the millimeter/sub-millimeter spectrum emitted by a pulsed relativistic electron beam, the temporal electron beam pulse duration and shape are characterized. This technique is used to measure a 1.3 picosecond relativistic electron bunch. In addition, we are able to resolve changes in electron bunch characteristics between the beginning and end of a train of bunches. Preliminary work has begun correlating electron pulse shape to FEL optical operation. Finally, variations in the controls of the electron beam system are correlated with changes in the electron bunch measured using the FTS. Unlike other techniques that destructively interact with the electron beam, this technique is totally passive and results in negligible perturbation in the electron bunch; hence, this technique can be used for direct real-time non-destructive electron bunch characterization.

i

Acknowledgments

To invent, you need a good imagination and a pile of junk. - Thomas A. Edison

Looking back over this project (and my entire graduate work at Duke), I find that very little of this would have been possible without the help and support of many people. First, I am most grateful to my advisor, Bob Guenther. He has been a constant source of jovial enthusiasm, unflappable patience, good advice and deep insight. He has not only let me work in his lab but has welcomed my interest in teaching and encouraged my participation in related optics research. It has been a great joy for me to work with someone who has both a great understanding and love of science.

I must also thank Dr. Frank De Lucia. Much of this project grew out of work he started 15 years ago on pulsed laser microwave sources. In addition, he has enthusiastically lent both material support and technical advice at critical points in this project. His understanding of experimental techniques, and generosity in sharing his expertise has been significant, not only to this project, but to all the work I have done at Duke. He has taught me much about research and I am very lucky to have been able to work with him, both here at Duke and at Ohio State.

I owe a great deal of thanks to several other professors. First, I am grateful to the members of my research committee for their advice and support throughout this project. They have all shown a great deal of interest in my work even though it did not always overlap with their own areas of research. I very much appreciate their encouragement, patience, and commitment. In addition to the members of my committee, I would like to thank the faculty of both the Department of Electrical Engineering and the Department of Physics . Although officially an electrical engineer, I have been shown great hospitality, generosity, and support by Physics. Both this project, and my education owe much to the informal camaraderie between these two departments.

I would like to thank Dr. John Madey and the members of the Duke Free Electron Laser Lab for their hospitality and efforts to support this project. This project would not have been possible without the help and advice of Dr. Eric Szarmes, Dr. Dave Straub, Dr. Ping Wang, Gary Swift, Jim Winogred, Jim Gustavsson, Mark Emamian, Genni Barnett, Chad McKee, Brett Hooper, and Bentley Burnham. Also I must thank Dr. Ron Jones, Dr. Joe Dutta, and Dr. Hero Kosai not only for their sound advice but also for collaborating on the measurements on their Picosecond Electron Beam System.

Many others have helped on this project not only as colleagues but as good friends. I wish to especially thank Guo Wei, for teaching me the about Fourier transform spectrometers; Dr. Travis Pape, for his generous contributions of equipment, advice and good humor; The (Duke) OSU Microwave group (Dr. Tom Goyette, John Pearson, Dan Flatin, Dr. Henry Everitt, and Dr. Jerome Holton) for teaching me the art and science of microwaves and cryogenics; Jennifer Truman-Bernhard, for being a great sounding board for some pretty odd ideas; Dr. Marian Peters, for always having good advice; Dr. Harry Cartland, for moving a lot of equipment and teaching me a bit of chemistry; Eric Smith, Judy Bailey, and Mary Ann Southern, for their patient help navigating the Duke libraries.

In retrospect I am very lucky; I love science and engineering and have been given the opportunity to participate daily in research and teaching. I will always be in debt to my parents for their early encouragement of my interests and their continued support and love. Finally, my greatest thanks goes to my wife, Kim. During my entire graduate career she has been caring, supportive, and patient. I am much indebted to her for her sacrifices and love.

<div align="right">J.C.S.   May 1994</div>

Contents

iv

List of Figures

vi

List of Tables

Glossary

a^* .... complex conjugate of a

c.c. .... complex conjugate of previous term

$f(t)$ .... a time domain function, f

$G(\omega)$ .... a frequency domain function, G

$\otimes$ .... convolution operator defined as $g(t) \otimes h(t) \equiv \int\limits_{t=-\infty}^{\infty} g(t) h(\tau - t) dt$

$\oplus$ .... correlation operator defined as $g(t) \oplus h(t) \equiv \int\limits_{t=-\infty}^{\infty} g(t) h^*(t - \tau) dt$

FT .... Fourier transform operator, $\mathrm{FT}\{f(t)\} = F(\omega) \equiv \int\limits_{t=-\infty}^{\infty} f(t) e^{-i\omega t} dt$

Chapter 1
Introduction

This project began as both a search for new sub-millimeter sources and as a further attempt at characterizing picosecond and sub-picosecond phenomena. The two tasks are directly interrelated by Fourier transform theory which states that any phenomena in the time domain can be equally well measured and characterized in the frequency domain. Originally, this project had focused on the use of sub-picosecond optically pulsed electro-optics as submillimeter sources and detectors. However, last fall, a unique opportunity developed to characterize the pulsed electron beam driving the Duke free electron laser (FEL). Although our original goal had been to investigate the potential of using the FEL beam as a source of millimeter and submillimeter radiation, we quickly realized that we could provide real-time diagnostic information to the FEL operators. Currently, only limited diagnostics are available to measure the performance of the electron beam and very little is known about the temporal structure of the electron pulses that make up the beam. As this paper will show, it is possible to use techniques borrowed from the areas of ultra-fast optics and microwave spectroscopy to measure the operational characteristics of picosecond pulsed electron beams.

The next two sections provide the background for this research, with descriptions of designs of submillimeter sources, electron beam monitors, and ultrashort pulse measurement systems. In the next chapters, we will develop the theory of pulsed electron beam measurements. Subsequent chapters describe the actual experimental system used to characterize the Duke FEL electron beam, and analysis of the collected data.

1.1 Basic Fourier Theory Background

Fourier theory states that a phenomenon measured and characterized in the time domain can be equally well measured and characterized in the frequency domain, with no loss of information about the underlying phenomenon. There is a considerable literature that discusses and applies this principle, and we will not duplicate that literature here. However, to set the stage for subsequent sections, a simple example is useful: consider an infinite train of gaussian pulses (figure 1-1). Mathematically[††], the pulse train is described in the time domain by,

$$\operatorname{rep}_T\left(\exp(-t^2/\tau^2)\right) \tag{1.1}$$

The Fourier transform of this function yields the frequency domain representation,

$$\frac{\tau^2}{T}\operatorname{comb}_{1/T}\left(\exp(-\tau^2\omega^2)\right) \tag{1.2}$$

If the signal is from a laboratory pulse generator, then by using either an oscilloscope (in the time domain) or a spectrum analyzer (in the frequency domain), we may measure and characterize the source. As shown in figure 1-1, in the time domain one can easily observe the pulse shape, pulse repetition rate (T), and the pulse width. Likewise, in the frequency domain, the spectral rolloff is unique to a particular pulse shape, the comb spacing yields the pulse repetition frequency ($1/T$) and the pulse spectral extent is characterized by $1/\tau$. Table 1.1 shows the Fourier transform of other common pulse shapes.

[††] The following definitions are borrowed from systems' theory:

$$\operatorname{rep}_T(f(t)) \equiv f(t) \otimes \sum_{n=-\infty}^{\infty} \delta(t-nT) \qquad \operatorname{comb}_T(f(t)) \equiv f(t) * \sum_{n=-\infty}^{\infty} \delta(t-nT)$$

These functions form a Fourier transform pair, i.e.,

$$\operatorname{rep}_T(f(t)) \Leftrightarrow \frac{1}{T}\operatorname{comb}_{1/T}(F(\omega)) \qquad \operatorname{comb}_T(f(t)) \Leftrightarrow \tfrac{1}{T}\operatorname{rep}_{1/T}(F(\omega))$$
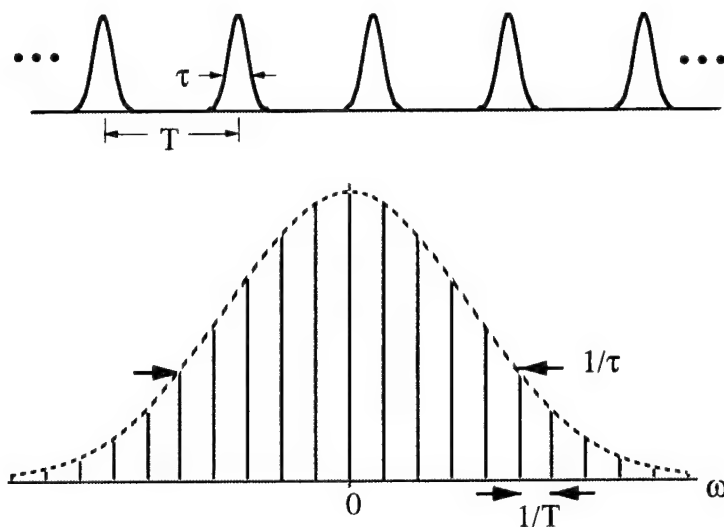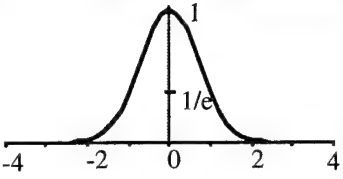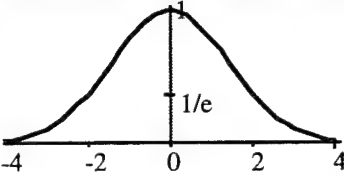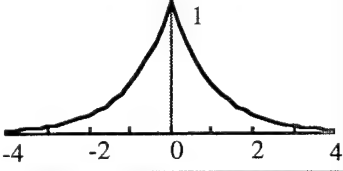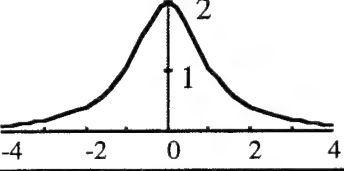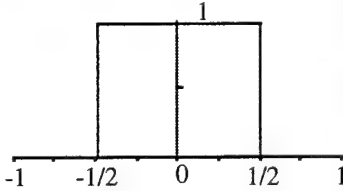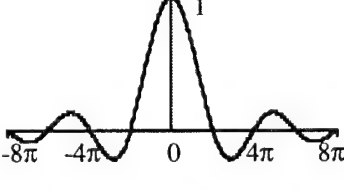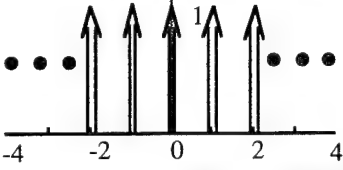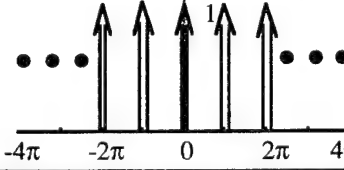
Fig. 1-1. A gaussian pulse train and its Fourier Transform.

This simple application of Fourier theory has considerable application in the design of both ultra-short pulse measurement electronics and ultra-high frequency signal sources. The next sections review general techniques for generating and measuring ultrafast/ ultra-high frequency signals. A third section will consider specific solutions to the problem of measuring bunched electron beams. The last section will highlight those aspects of time and frequency domain systems used to measure the picosecond electron bunches studied in this project.

Table 1.1 Various pulse shapes and their Fourier transforms.

$f(t) = \dfrac{1}{2\pi} \displaystyle\int_{-\infty}^{\infty} F(\omega)e^{j\omega t}\,d\omega$		$F(\omega) = \displaystyle\int_{-\infty}^{\infty} f(t)e^{-j\omega t}\,dt$	
e^{-t^2}		$\pi^{1/2}\,e^{-\omega^2/4}$	
$e^{-|t|}$		$\dfrac{2}{1+\omega^2}$	
$\mathrm{rect}(t)$		$\dfrac{\sin(\omega/2)}{\omega/2}$	
$\Sigma\,\delta(t-n)$		$\Sigma\,\delta(\omega-n)$	

1.2 Millimeter/Submillimeter Sources

There currently exist a wide variety sources which generate signals in the picosecond/ terahertz range. Of particular relevance to this paper are sources which use pulsed electron beams such as klystrons, linear accelerators, and free electron lasers (FELs). Also, we will briefly review the characteristics of pulsed laser systems, because they share many characteristics of pulsed electron beams.

Klystrons are simple electron beam devices, shown schematically in figure 1-2, in which a continuous stream of electrons with initial velocity, v_o, is bunched due to an imposed time variable electric field, $V_1 \sin \omega t$. The direction of this applied electric field is parallel to electrons' velocity. This electric field modulates the velocity of the electrons as they pass; depending on the interaction phase angle, some electrons acquire a higher velocity, while some will be slowed. Figure 1-3 shows the effect of the velocity modulation on the electron's trajectory; if allowed to drift, the velocity modulated electron beam will form bunches. Analyzed in the frequency domain, the electron beam at the catcher contains considerable high frequency content. If these bunches are passed through a waveguide region or resonator, they will couple energy of similar frequency content into the RF field supported by the cavity or guide.
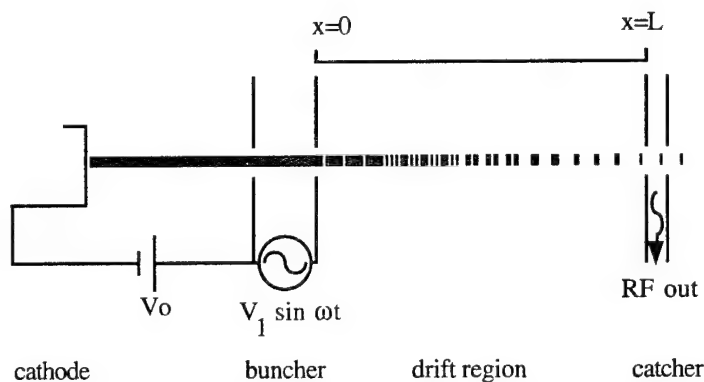
Fig. 1-2. Schematic representation of a klystron.
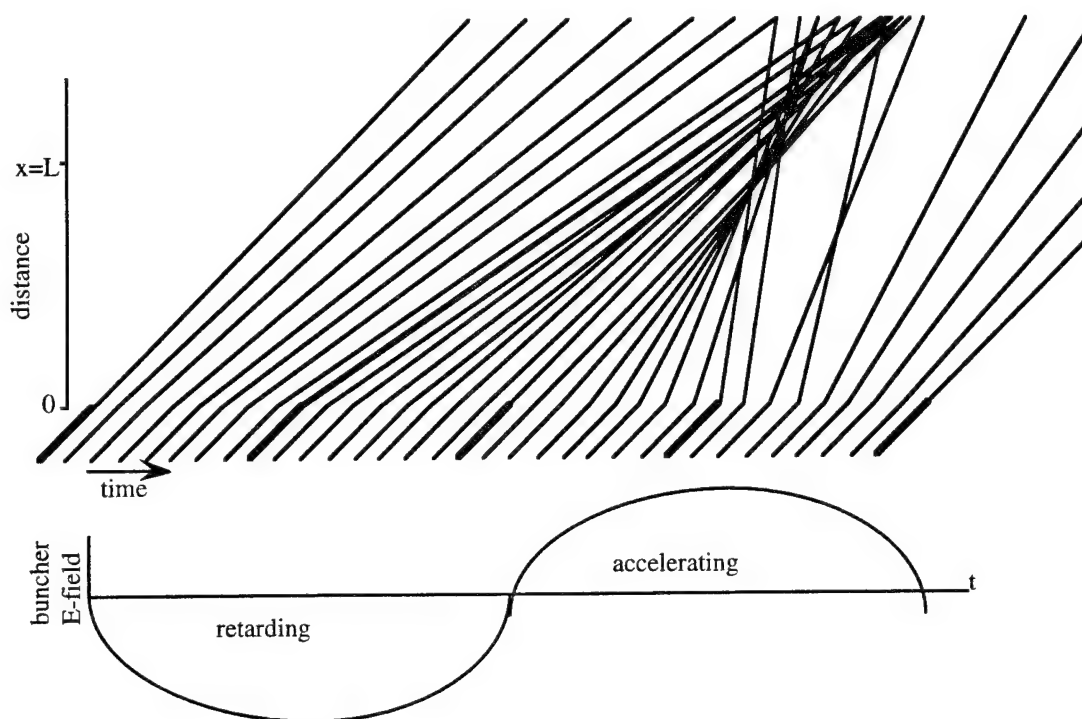
Fig. 1-3. Bunch of electrons by velocity modulation.

Klystrons operating in excess of 50 GHz are currently commercially available. The high frequency operation is limited by the duration and density of the bunch generated in the drift region and the transit time required for the electron bunch to cross the catcher gap.

One method of controlling and improving the electron bunching is to allow the electrons to leave the cathode during only short time intervals. This approach, called "pre-bunching", has been implemented using a pulsed laser to cause photoemission of electron bunches off a photocathode [De Lucia, 1983; De Lucia, et al., 1985; Swartz, 1989]. Figure 1-4 shows a schematic of a simple laser driven source. In one configuration (figure 1-4a), the electrons couple energy into the waveguide modes as they transit from the cathode to the anode grid. A variation on this arrangement has the "catcher" waveguide (or more efficient structures) beyond the anode (figure 1-4b). In either approach, the electron bunch has the same temporal profile as the generating laser

pulse; a picosecond pulsed laser will produce picosecond duration electron bunches. Although optically pre-bunched sources have generated signals to 30 GHz, their performance is limited by low photoemission currents (a few milliamps, peak) and, like the conventional klystron, waveguide transit time.
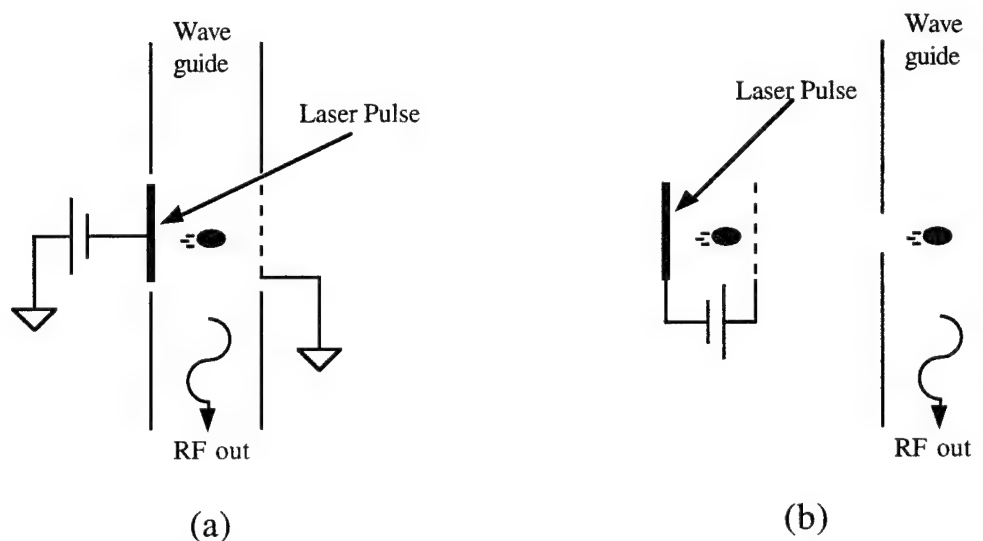
Fig. 1-4. Laser driven photocathode based pre-bunched electron sources. (a) Photocathode and anode integrated in waveguide produce RF as electron bunch crosses waveguide gap. (b) Photocathode electron source is removed from the waveguide; electrons pass through wire mesh anode and drift across waveguide gap.

One method of improving the current produced by pre-bunched sources uses field enhanced thermionic emission instead of photoemission. In this technique [Westenskow and Madey, 1984], a thermionic cathode is placed at the center of an RF cavity as shown in figure 1-5. The electric field in the cavity will drive electrons off the cathode during half the RF cycle. During the second half of the RF cycle, the electric field in the cavity will accelerate any electrons still in the cavity back toward the cathode, causing cathode heating. The energy of the electrons leaving the cavity is clearly a function of RF phase. A properly designed cavity and cathode will emit

electrons over only a portion of the RF drive cycle at an average current of 0.1 - 1 amp.
Unfortunately the electron bunches emitted by the gun have a wide range of energies
(high energy electrons near the beginning of the RF phase, low energy electrons later)
over a large portion of the RF phase, and are therefore not well bunched in time.
Fortunately, because the electron energies change with RF phase, a energy filter will
pass only electrons with only a narrow energy spread, which corresponds to a fraction
of the RF phase, or a short time period. In the Duke Mark III FEL, an alpha magnet is
employed as the energy filter and produces electron bunches of a few picoseconds
duration [Benson, et al., 1986].

TM_{010} Cavity

Cathode

Electron beam

RF feed
wavguide
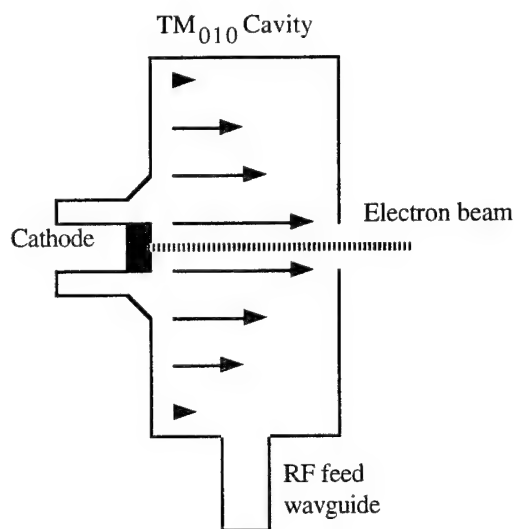
Fig. 1-5. Schematic of electron gun using field enhanced thermionic
emission. The cavity is shown during the emission phase of the RF drive
signal.

Having generated the bunched electron beam as discussed in the previous
paragraphs, a variety of techniques may be used to couple high frequency energy from
the electron bunches. One approach is to accelerate the electron bunches (using a
LINAC) to relativistic energies and pass the bunch through a reduced height waveguide

or cavity, similar in geometry to the klystron catcher. At relativistic energies, the electron bunch will have the minimum possible transit time crossing any gap. Coleman [Coleman, 1957; Coleman and Sirkis, 1955; Kaufman and Coleman, 1957; Sirkis and Coleman, 1957] has used megavolt potentials to accelerate electron bunches through high order mode (TM_{018}) cavities and subsequently produce near millimeter radiation (1 watt at ≈ 80 GHz). Another approach to producing millimeter and submillimeter radiation (MM/SMM), pursued by Motz and later adapted by the FEL community, is to pass the relativistic electron bunch through a region of alternating magnetic field (figure 1-6) [Motz, 1951; Motz and Mallory, 1955; Motz, et al., 1953]. The magnetic field will cause the electron bunch to accelerate back and forth, or "undulate", transverse to its direction of travel. The "undulating" bunch will radiate RF. Motz has used such an series of 25 magnets to generate light in the visible spectrum and broadband millimeter radiation (1 watt at 158 GHz). The modern FEL is a direct descendent of this device.
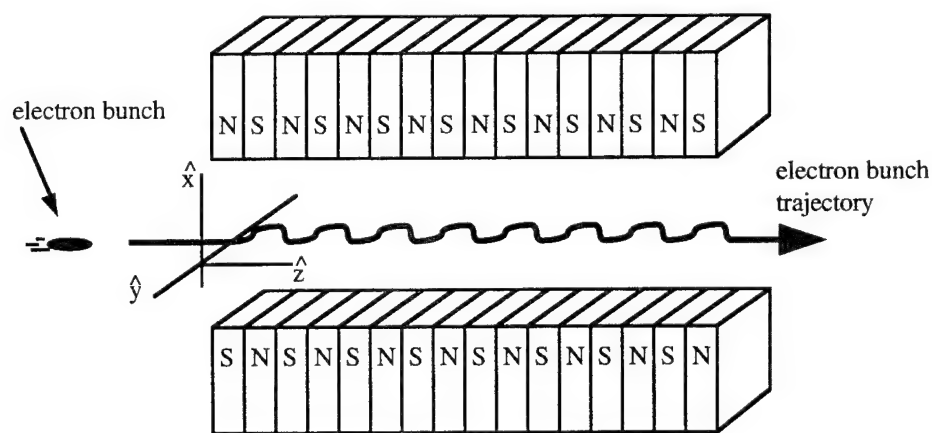
Fig. 1-6. Schematic of an electron bunch undulator. The alternating magnetic field causes the electron bunch to oscillate, or undulate, in the y-z plane.

Whereas, all the previously discussed devices have been based solely on the ability to bunch electrons as they travel through free space, an entire class of solid state devices rely on the ability to optically generate short duration currents in semiconductors. The

basic design of such a device is shown in figure 1-7. Electrically, the device is a biased transmission line connected to a dipole antenna. An electro-optical switch centered between the dipole arms is normally open; however, when struck by a sub-picosecond optical pulse (from either a Ti:Sapphire or CPM laser), the switch conducts briefly, generating a current on the dipole and producing a radiated sub-picosecond EM transient. Although the currents are much smaller, this general approach to generating current pulses and EM transients is similar to the laser pre-bunched klystron; both systems rely on the pulse characteristics of the laser to create short electron bunches, and both systems have the electron bunches couple energy onto radiating structures. As discussed in the next section, a variety of methods exist for measuring these generated EM transients.
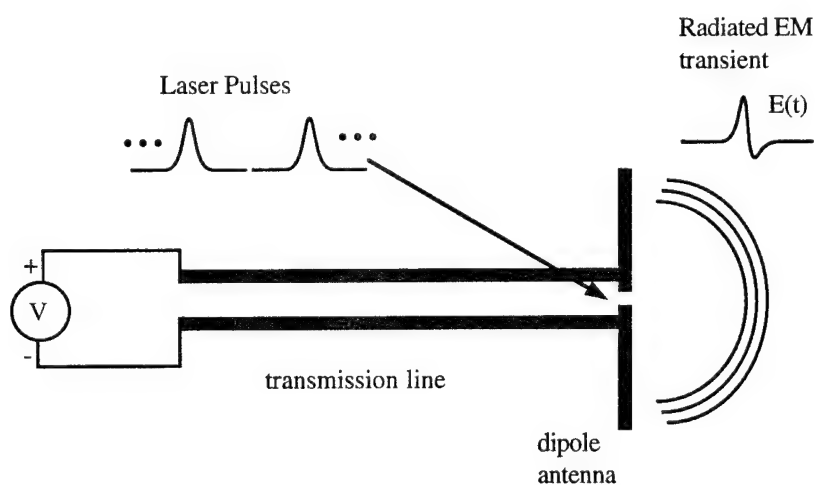
Fig. 1-7. Auston electro-optic dipole source. The transmission line and antenna are fabricated on an electro-optical material. A laser pulse causes the electro-optical material to conduct and generate an EM transient, subsequently radiated by the dipole. For material with sufficiently short carrier lifetime, the radiated EM transient will have the same time profile as the laser pulse.

1.3 Ultrafast/ Ultra-high Frequency Measurement Techniques

Ideal instrumentation will accurately analyze the signal in either time or frequency domain, however, real instruments may reduce the amount of signal information presented. If the slew rate of a signal is greater than the response time of an oscilloscope, then the displayed signal will have a slower rise and fall than that of the original signal. If the signal pulse period is less than the spectrum analyzer scan time, or if the pulse is very short (yielding spectral content outside the scan range) then the displayed signal will only partially represent the input. Conventional oscilloscopes have risetimes of a few hundred picoseconds, whereas most spectrum analyzer have an upper limit scan frequency of 10's of gigahertz. For signals with short pulse widths (< 100 pS) and wide bandwidths (> 10 GHz) other measurement techniques must be used.

A variety of time domain techniques are available for analyzing ultrashort (< 100 pS) optical and EM pulses. These techniques include correlative sampling, streak scanning, and autocorrelation.

1.3.1 Time Domain Correlative Sampling

High speed sampling of repetitive electrical signals requires a fast switch, a capacitor, and a pulse generator with variable delay (figure 1-8a). During each occurrence of the repetitive signal (figure 1-8b), the pulse generator causes the switch to sample the signal for a short time; the sampled voltage is stored on the capacitor where it is subsequently measured and the measurement stored (a relatively slow process). Varying the delay of the sampling pulse relative to the signal allows the sampling circuit to progressively capture the shape of the repetitive signal. Several different types of time domain sampling systems have been successfully built. Grove [Grove, 1966] built and tested a sampling head with a 28 pS sampling duration (12.8 GHz signal bandwidth). Merkelo [Merkelo and Hall, 1972] extended the sampling head

performance to a sampling duration of $\approx$12 pS (30 GHz signal bandwidth). More recently, Bloom's group at Stanford has used non-linear transmission line pulse generators and integrated beam lead sampling diodes to build a 2.5 pS sampling unit (130 GHz bandwidth) [Marsland, et al., 1989; Van Der Weide, et al., 1992]. In 1983, Auston presented a method for using subpicosecond pulsed lasers to electro-optically generate and sample electrical signals propagating on transmission lines [Auston, 1983; Auston, 1984; Auston, 1988; Auston and Nuss, 1988; Auston and Smith, 1983]. Valdmanis [Valdmanis and Mourou, 1984; Valdmanis, et al., 1983] has extending the electro-optical technique and has developed several electro-optical sampling devices including one system with subpicosecond sampling (1 THz bandwidth) [Valdmanis, 1987].

The only drawback to these devices is the requirement that the sampling trigger needs to be synchronized to the signal source. Although this is not a generally a problem for electrically based pulse generators, synchronizing pulsed lasers to external references is a difficult problem, as a result the electro-optical based samplers have limited use.

(a)

(b)
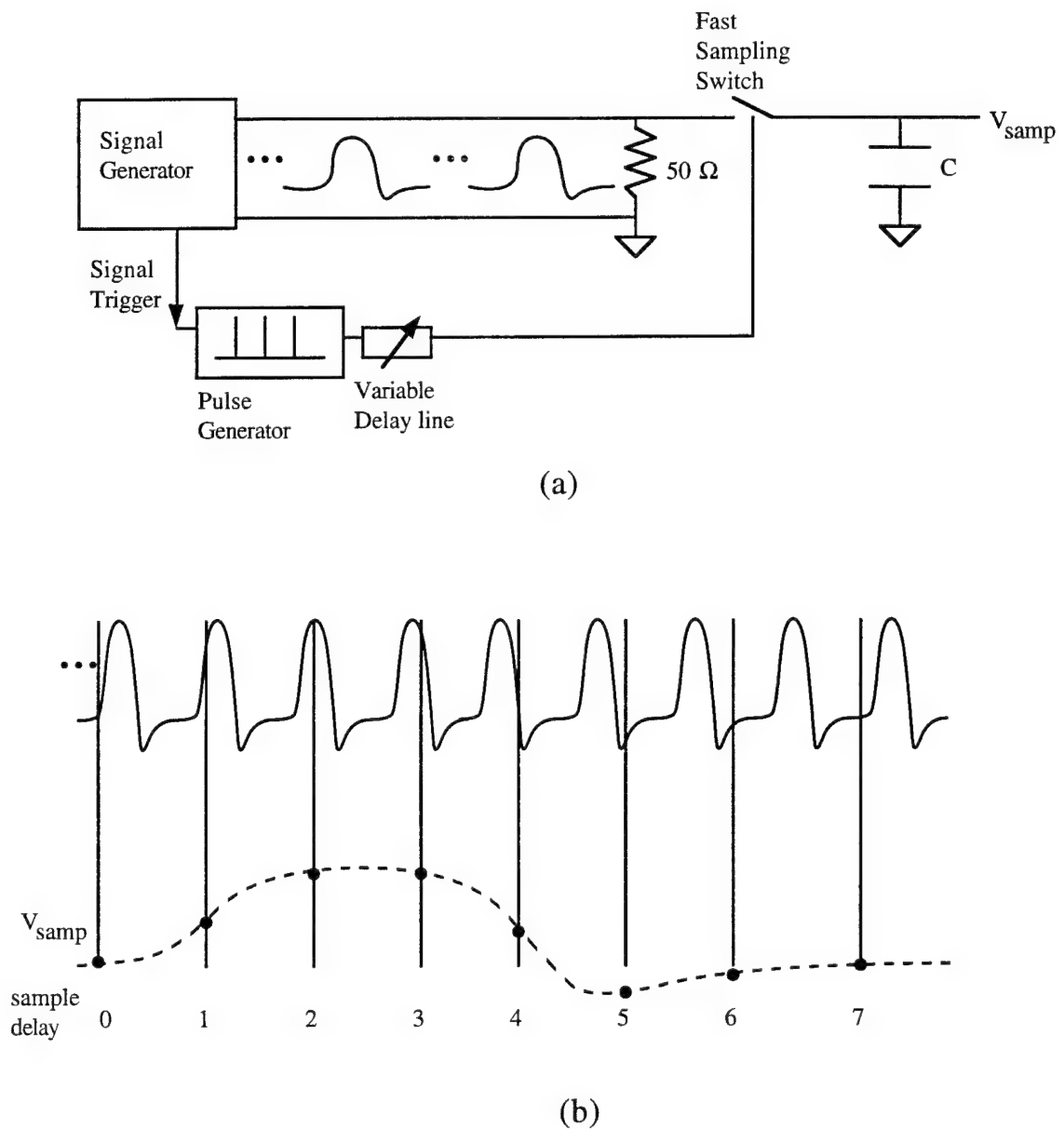
Fig. 1-8. Sampling circuit schematic. Simplified circuit design (a) and sampling operation (b) .

1.3.2 Streak Cameras and Scanning
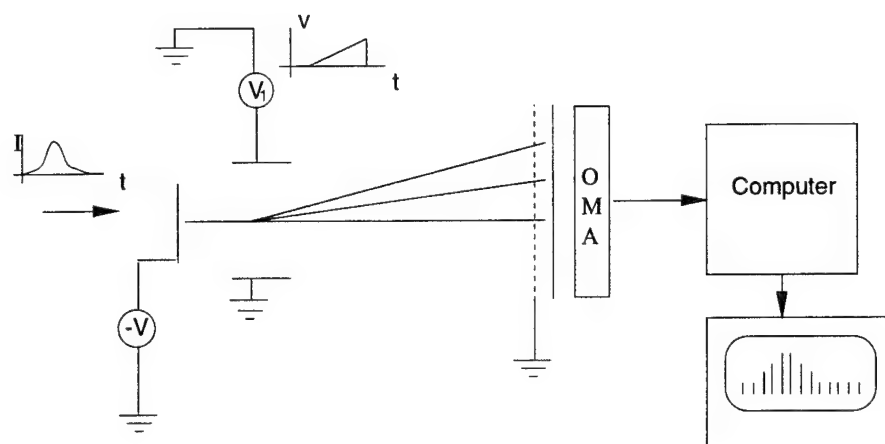
Fig. 1-9. Schematic of a simple streak camera: V_1, sweep generator; V, photocathode supply; P, photocathode; OMA, optical multichannel analyzer.

Streak cameras are another time domain instrument capable of recording picosecond duration events; unlike the sampling systems in the previous section, streak cameras are capable of recording one-shot events. Streak cameras are electro-optical devices; a simple streak camera is shown schematically in figure 1-9. In operation, a short optical pulse hits the photocathode and simultaneously triggers the electrode sweep voltage. The time profile of the electron density corresponds to the optical intensity time profile. As the photoelectrons travel from the photocathode to the anode, the time varying electrode potential V_1 will produce a time varying force, deflecting the electron beam. Electrons generated early in the sample time will hit near the bottom of the display anode, while electrons generated later will strike the anode higher. The electron density, proportional to the input optical beam intensity, generates light when it strikes the phosphor on the anode. The phosphor display will produce an intensity proportional to the time intensity of the input beam.

Current state-of-the-art streak cameras have a limiting time resolution from 0.7 picoseconds [Baggs, et al., 1985] to 0.5 picoseconds [Kominami, et al., 1985]. Baggs et al. state that the limiting resolution of 0.2 picoseconds is potentially realizable. Streak cameras have also been built to collect multiple channels of data simultaneously [Majumdar, et al., 1988]. An early demonstration of this technique by Seymour and Alfano [Seymour and Alfano, 1980] simultaneously measured the left and right circular polarization profile of semiconductor lasers.

Although quite useful, the use of streak cameras is limited for three reasons. First, the input signal must be an optical signal; electrical signals must be first converted to either an optical pulse or an electron stream. Second, streak cameras (and the associated drive and analysis electronics) are quite expensive. Finally, streak cameras are also limited by the dynamic range and spectral sensitivity of the phototube; operation at infrared requires a different phototube than operation in the visible [Doukas, et al., 1982].

1.3.3 Autocorrelation

Another widely used method of short time measurement is autocorrelation. The autocorrelator produces an output modeled by,

$$A_f(\tau) = \int f(t)f(\tau + t)d\tau \qquad (1.3)$$
$$= f(t) \oplus f(t)$$

where $f(t)$ is the optical input intensity, τ is the optical delay, and $A_f(\tau)$ is the autocorrelation ($\oplus$ denotes the correlation operator). It is important to note that the integrand of equation (1.3) is dependent on the initial pulse shape. As a result, the autocorrelator, in general, generates a pulse shape dependent, non-linear measurement of the pulse width. The autocorrelation for a gaussian pulse is shown in figure 1-10.

g(t) $A(\tau) = g(t) \oplus g(t)$

τ_w $2\tau_w$
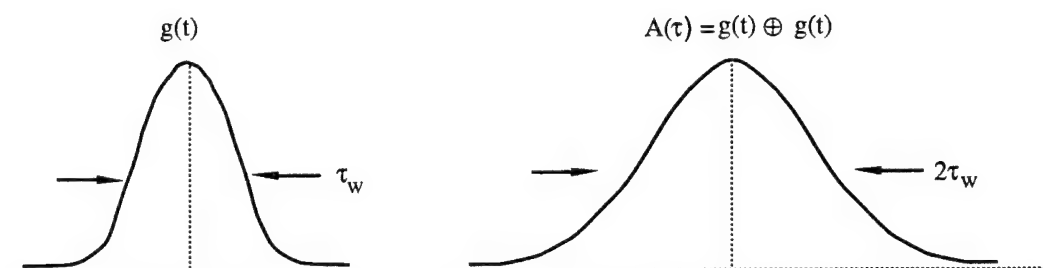
Fig. 1-10. Autocorrelation of a gaussian pulse.

A variety of optical phenomena have been used to build autocorrelators, including phase conjugation [Bouchert, et al., 1985], two-photon fluorescence [Giordmaine, et al., 1967], and second harmonic(SH) generation. Of these, the typical hardware implementation uses SH crystal and a Michelson interferometer (figure 1-11). The input optical beam is split, and half of the beam is delayed by the variable length arm, l. The two beam components are slightly offset (by the roof-top prisms) and focused through the SH media. When photons coincide in time and space in the SH media, frequency doubling occurs and a photon of 2ω is generated. The intensity of the doubled photons correspond to the integral of equation (1.3), where τ is the delay imposed by the variable arm ($\tau = 2l/c$). The readout electronics measure the detector response as the delay arm length varies and displays the result.

CR

BS   SH   F

CR 2ω D

Input
Beam
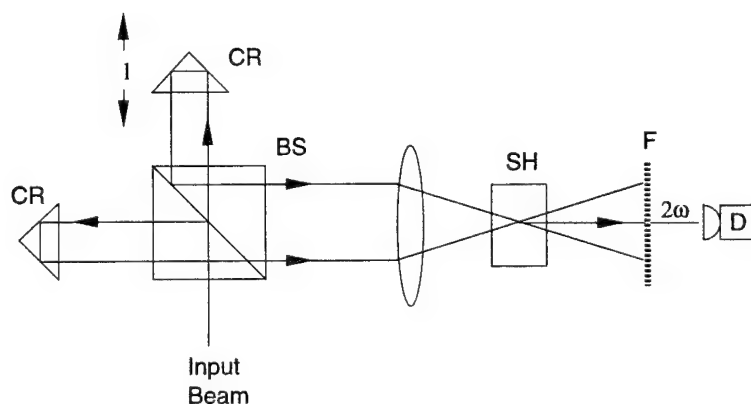
Fig. 1-11. Autocorrelator schematic: <u>CR</u>, corner reflector; <u>BS</u>, beam splitter; <u>SH</u>, second harmonic crystal; <u>F</u>, high pass optical filter; <u>D</u>, detector; <u>l</u>, optical delay path.

Autocorrelators have been built around several designs. Commercial models are available but are quite expensive. Due to limits imposed by the SH media available, autocorrelation is generally limited to visible and infrared light. Also, in practice the autocorrelation function requires an *a priori* knowledge of the pulse shape to accurately determine its width; conversion factors for several shapes are shown in Table 1.2. Autocorrelation measurements are also possible using only a detector and no SH media; this technique is closely related to frequency domain Fourier Transform Spectroscopy, reviewed in the next section and discussed in detail in subsequent chapters.

Table 1.2. Comparison of full width at half maximum of a function and its autocorrelation. t_{FW} is the full width at half maximum of the original function and τ_{FW} is the full width at half maximum of the autocorrelation of the function. The values for sech^2 were obtained in closed form, based on results given by Sala [Sala, et al., 1980]and Yariv[Yariv, 1985].

$f(t)$	$t_{FW} =$ FWHM$\{ f(t) \}$	$\tau_{FW} =$ FWHM$\{f(t) \oplus f(t)\}$	τ_{FW}/t_{FW}
$\exp(-t^2/a^2)$	$2a\sqrt{\ln 2}$	$2a\sqrt{2}\sqrt{\ln 2}$	$\sqrt{2}$
$\text{rect}(t/a)$	a	a	1
$\exp(-t/a),\ t \geq 0$	$a \ln 2$	$2a \ln 2$	2
$\text{sech}^2(t/a)$	$2a\cosh^{-1}(\sqrt{2})$	$\approx 4a\left(\cosh^{-1}(\sqrt{2})\right)^3$	$\approx \dfrac{1}{2}a\left(\cosh^{-1}(\sqrt{2})\right)^2$

1.4 Frequency Domain MM/SMM Measurement Techniques

The previous sections have considered time domain techniques for characterizing phenomena with durations << 100 pS. In the frequency domain this corresponds to signals with bandwidths > 30 GHz , or the MM/SMM range of the spectrum (>1 cm⁻¹, or λ < 1 cm). Historically, MM/SMM frequency domain measurements have been

restricted to specialized laboratories. The primary reason for this restriction is the lack of convenient detectors (or mixers) of MM/SMM radiation. A secondary reason has been the limited availability of MM/SMM sources, necessary for heterodyne detection. Over the past forty years these problems have been overcome, so that now there are detectors, sources, and measurement techniques for characterizing signals from DC to over two terahertz. This section reviews these devices and techniques, starting with a review of practical MM/SMM detectors, followed by a discussion of MM/SMM measurement systems.

1.4.1 MM/SMM Detectors

Three types of detectors are typically used in work beyond 30 GHz: Golay cells, bolometers, and detector diodes.

Golay cells [Golay, 1947a; Golay, 1947b; Golay, 1949] are simple infrared detectors made from a gas filled cylinder containing an infrared (IR) absorber (figure 1-12). One end of the cylinder is fitted with an IR transparent window, the other end has a flexible membrane, mirrored on its outside surface. Any radiation ($> \sim 1$ cm^{-1}) focused onto the IR absorber will heat the cell, increasing the temperature and pressure of the gas. The pressure increase flexes the mirrored membrane, deflecting an optical beam which is sensed by appropriate electronics. The walls of the cell form a thermal ground so that when the thermal source signal is removed, the gas temperature and membrane flexure decrease, restoring the output signal to its zero point. Golay cells have an noise equivalent power (NEP) of $\sim 10^{-10}$ watts/Hz$^{1/2}$, however their response time is limited to ~50 milliseconds (response time will be important later in the design of the FEL electron pulse monitor). Golay cells are also relatively fragile and sensitive to vibration and ambient noise, therefore, their use is typically restricted to controlled laboratory conditions. Golay cells are insensitive to γ-rays and neutron beams, hence, these detectors may be used in high radiation environments.
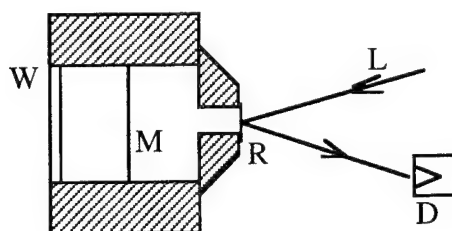
Fig. 1-12. Golay Cell Design. W: IR transparent window; M; IR absorbing membrane inside gas filled cell; R: mirrored membrane; L; optical monitor beam; D: optical displacement detector.

Detector diodes are widely used in commercial and industrial applications [Bhartia and Bahl, 1984, pp. 421-31]. Although several practical designs have been described, most commercially available detectors use either a point contact (cat's whisker) or beam lead contact. Either approach produces a metal-to-semiconductor diode junction. The diode acts as a square law detector where the cutoff frequency, f_c, is

$$f_c = (\ 2\pi\ C_{jo}R_s)^{-1} \tag{1.4}$$

where C_{jo} is the zero bias diode junction capacitance. Typical cutoff values are ~100 GHz for silicon point contact diodes, >1 THz for point contact GaAs diodes, ~ 800 GHz for beam lead GaAs contacts. Detector diodes have video bandwidths determined by packaging capacitance from 10 to 1000 MHz, making them useful for monitoring modulated signals.
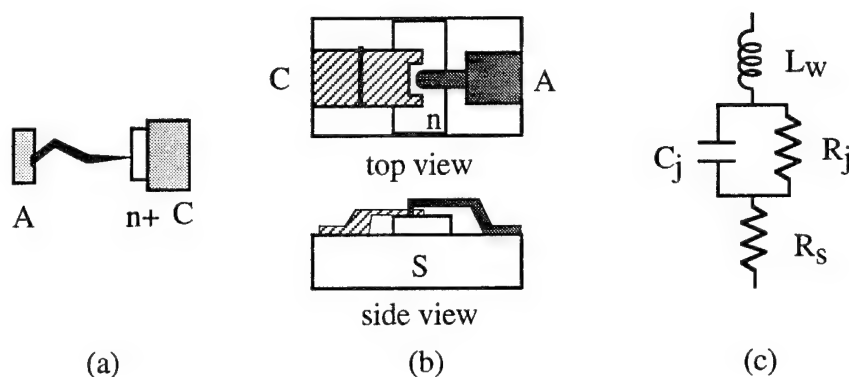
Fig. 1-13. Typical microwave detector diode designs. a) Point contact detector and b) Beam lead detector: C, cathode contact; n^+, n-type semiconductor; A, anode contact connection; S, support substrate. c) Detector equivalent circuit: C_j junction capacitance; R_j junction nonlinear resistance; L_w contact inductance; R_s contact series resistance.

Bolometers are the final type of detectors widely used in mm/sub-mm work (and used in the experiments discussed in this thesis). In general a bolometer is a detector whose carrier mobility, and hence conductivity, is a strong function of thermal temperature [Kogan, 1963; Putley, 1977]. Although the thermal sensitivity is small for most materials, for some semiconductors, under special conditions, this dependence is significant. One such material is InSb operated at 4 K. At cryogenic temperatures the carriers are loosely coupled to the lattice and may have a temperature different from that of the lattice. The theoretical sensitivity of InSb hot-electron bolometers is ~2000 V/W with a NEP of ~ 10^{-13} W $Hz^{-1/2}$ [Rollin, 1961]. When properly matched to an amplifier, the response time of the InSb bolometer is < 1 μs. InSb bolometers are sensitive to mm-waves with frequencies as high as 2 THz [Sakai and Sakai, 1976; Shivanandan, et al., 1975]. InSb detectors are rugged, and relatively easily constructed. The only drawback to their use is the need for cryogenic cooling (liquid nitrogen and liquid helium). A helium cooled InSb hot-electron bolometer is used in this project.

1.4.2 MM/Sub-MM Measurement Systems

General MM/SMM measurement systems are concerned with determining how much radiation exists in a given frequency interval; hence most spectroscopic techniques are applicable to MM/SMM signal characterization. In this section, will review four spectroscopic techniques: filtered straight detection, heterodyne conversion, grating spectrometry, and Fourier transform spectrometry.

Straight detection is the simplest type of measurement to implement, requiring only a detector and bandpass filter (or filters). The MM/SMM signal travels through the filter and onto the detector. The detector receives only energy passed by the filter in the frequency range. In the MM/SMM region a wide variety of filters are available, such as material filters, grid and mesh filters, and Fabry-Perot etalons. By changing filters one may change the frequency range measured. Although simple, there are several drawbacks to this approach. First, much of the MM/SMM signal is wasted in any given measurement and so a very sensitive detector is required. Second, the spectral resolution of this approach is limited by the filters which is typically > 1 GHz. Finally, the time required to switch filters makes this technique useless for characterizing single transients.

Another approach, on which the RF spectrum analyzer capitalizes [Peterson, 1989], is heterodyne down conversion. The signal to be measured is mixed on a square law detector with a signal (not necessarily the fundamental) derived from a frequency adjustable local oscillator (LO). Through appropriate filtering, the output of the mixer is the sum and difference of the LO and the input signal in the frequency range of interest. Spectrum analyzers have only two drawbacks. First, one needs a mixer that is sensitive in the spectral range of interest; because mixer and detector technology are similar a MM/SMM detector often make an appropriate mixer. The second problem, is the requirement for a tunable narrow bandwidth LO in the spectral range of interest.

Backward wave oscillators, fill this requirement but are very expensive. Multiplied frequency sources are sometimes used, however, because the efficiency of these sources drops by at least the square of the harmonic number, multiplied sources are useful to few hundred gigahertz.

Grating spectrometers have found wide use in the sub-millimeter and far infrared. Like their optical counterpart, the MM/SMM grating spectrometer brings radiation through a slit and onto a grating. The grating, shown in figure 1-14 disperses the different spectral components, which make up the signal, into different wavelength dependent angles [Guenther, 1990, pg. 385] predicted by,

$$m\lambda = 2\,d\,\sin\,\theta_B\,\cos(\phi_i + \theta_B) \tag{1.5}$$

where m is the diffraction order, θ_B is the grating blaze angle, and ϕ_i is the angle of the incident radiation relative to the blaze angle, and d is the grating spacing. The grating can be constructed (θ_B selected) so that at a wavelength λ_B most of the energy will diffract into a given order m. Typically gratings are blazed so this condition is met for $m=1$ and θ_B is between 15° and 30°.

In a spectrometer, radiation diffracts off the grating and is focused onto an array of detectors, located at these different angles, or, a single detector may be used and the grating rotated. The former approach allows broad spectral measurements to be made with resolution determined by the size and spacing of the detectors. The later approach yields higher resolution, but requires longer time to scan the source spectrum. A major problem in either case (and grating spectrometers in general) is that the grating disperses energy in a periodic fashion; signals at one frequency may be dispersed into multiple orders. Because of this, energy at a higher frequency ($\lambda/2$, $m=2$) can be dispersed at the same angle as energy at a lower frequency (λ, $m=1$). To avoid this problem, band pass filters must be used on the broadband signals before characterization by the grating spectrometer. Chantry also indicates [Chantry, 1971,

p. 21] that a grating can only be used over a range of $^2/_3\lambda_B$ to $^3/_2\lambda_B$, with $\lambda_B \approx d$ in the range of use. As a result, measurement of a broad spectra requires multiple gratings.
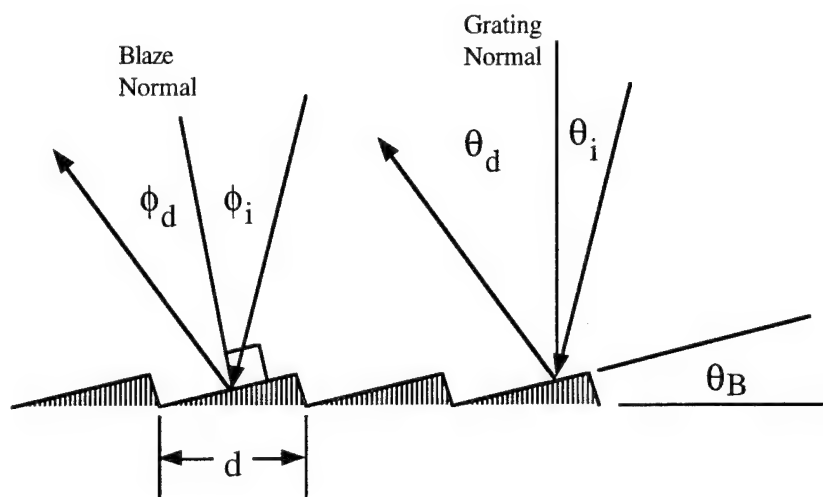
Fig. 1-14. Blazed diffraction grating geometry. Blaze angle is θ_B.

Fourier transform spectroscopy (FTS) is the final spectroscopic technique to be reviewed. Fourier transform spectroscopy uses a Michelson interferometer and a single detector to measure the interferogram of a signal. The Fourier transform of the interferogram is the power spectrum of the signal. Fourier transform spectrometers are easy to construct, work over a large bandwidth (5 cm^{-1} to > 100 cm^{-1}) with good resolution (< 0.1 cm^{-1}), and are very efficient. A drawback of FTS is that high resolution and broad bandwidth require long interferometer scan lengths, with corresponding long scan times which are not well suited for signals with rapidly varying spectra. Nonetheless, the FTS is the spectrometer used for most of the work in this dissertation; a more thorough discussion of FTS construction and operation is left for a later chapter.

1.5 FEL E-beam Diagnostics Overview

At this point, we have discussed general techniques for generating and measuring picosecond/terahertz signals. We may now focus on the purpose of this research which is to measure the temporal characteristics of the relativistic electron bunches which drive the Duke Mark III FEL. The characterization of this type of system has considerable history. The first part of this section will briefly review prior techniques of electron beam monitoring. The last part of this section, and the chapter will outline the approach used in this project to measure the picosecond characteristics of the electron beam.

1.5.1 Previous Electron Beam Measurement Techniques

It is useful to review traditional electron beam diagnostics and their limitations. Current diagnostics fall into three categories: beam position monitors, synchrotron radiation monitors, and energy spectrometers.

Beam position monitors (BPM) have been used in a variety of configurations for over 30 years [Bergere, et al., 1962; Billing, 1988; Coombes and Neet, 1967; Denard, et al., 1983; Farinholt, et al., 1967; Jachim, et al., 1981; Kulke, et al., 1988; Neal, 1968; Shafer, 1985; Simpson (conference chair), 1985]. The typical BPM, shown in figure 1-15, uses an RF pickup (loop antenna, stripline coupling structure, or resonant cavity pickup) to sense the electromagnetic (EM) transient generated by an electron bunch as it passes the BPM location. The signal produced by the BPM is proportional to the distance between the beam and the pickup. Hence, by using an array of these monitors, one may determine the location of the center of the electron beam. BPMs are normally sensitive to the low frequency radiation (< 10 GHz) produced by the EM transient. In addition, the video bandwidth of the typical detector provides only a few tens of megahertz response. Therefore, the time response of a BPM is limited to monitoring

temporal evolution of the signal due to trains of electron bunches, and not the individual electron bunch signal.
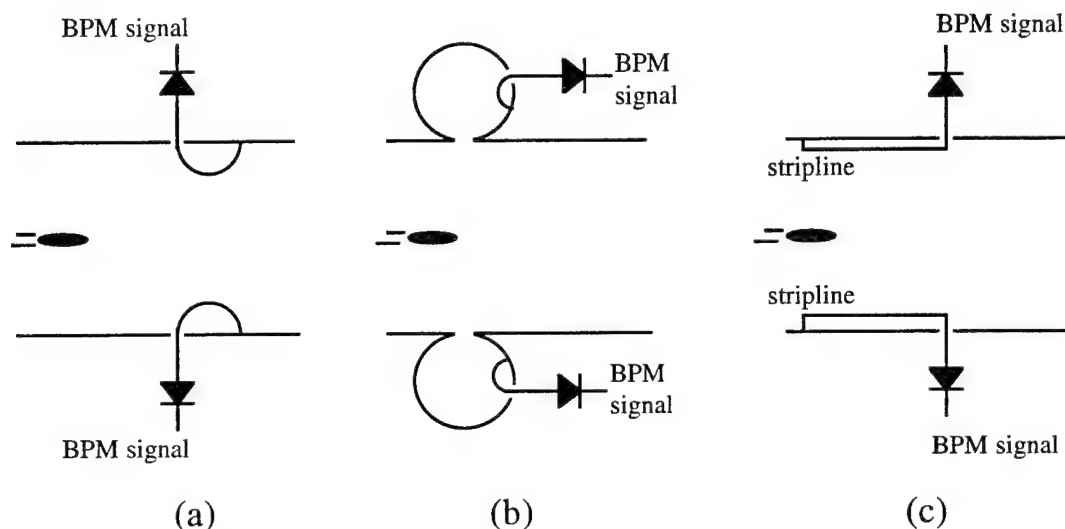
Fig. 1-15. Conventional electron beam position monitors. (a) BPM using simple loop pickup, (b) using resonant cavity pickup, (c) using stripline pickup.

Synchrotron radiation monitors (SRM) are based on the principle that a relativistic electron beam radiates a narrow cone of radiation as the beam is accelerated (e.g., by turning magnets) [Jackson, 1975; Motz, 1951; Motz, et al., 1953]. By using appropriate optical detector arrays, researchers have used synchrotron radiation from relativistic electron bunches [Billing, 1988; Brodsky, et al., 1992; Coombes and Neet, 1967; Kleman, 1988] as a means of determining electron beam positions. The response time of the typical detector arrays (e.g., < 1 nS) is insufficient for picosecond bunch measurement. However, one group has used a streak camera to measure Cherenkov radiation emitted by a relativistic electron bunch to determine pulse length of 34 pS bunches [Sheppard, et al., 1985]. A limitation of all these methods is that they do not allow simultaneous beam use and monitoring.

Although not a direct tool for monitoring bunched electron beam temporal characteristics, accelerator operators often used the energy spectrometer to infer electron beam parameters [Neal, 1968]. The energy spectrometer is simply a magnet which bends the high energy electrons through a greater angle than lower energy electrons. Because the electron bunch length and energy spectrum are related, the spectrometer indirectly yields an indication of pulse length. Again, this analysis technique is indirect, and destructively interferes with the electron beam.

By modifying the bending magnet power supply on the energy spectrometer it is possible to sweep the beam over time in a fashion analogous to the operation of a streak camera. Again this technique destructively interferes with the electron beam; in addition, temporal resolution is disrupted due to the energy spread on a typical relativistic electron beam.

1.5.2 Electron Beam Measurement in this Project

Although widely used, traditional electron beam monitoring techniques have poor temporal resolution, and may destroy the electron beam they seek to measure. However, a simple extension of the BPM concept allows the use of standard microwave spectroscopic techniques to measure the electron beam transient and determine the pulse shape and width. Instead of a narrow band coupling structure and detector, this projects uses a broadband pickup and a Fourier transform spectrometer to monitor the electron bunches. The theory and experimental results of such a measurement are developed in the next chapters.

Chapter 2
Theory

The goal of this chapter is to understand the signals produced by the electron beam emitted by the Mark III LINAC and subsequently measured by the FTS system. To achieve this goal, it is first best to start by reviewing the operation of the signal source, in this case the Mark III electron beam accelerator. The total operation of the Mark III can be understood by breaking the problem into smaller parts, developing the theory for each part, then finally assembling the individual theoretical components to produce a complete model of the signals produced. Once the RF source is modeled, we must consider a model for the transmission system that carries the RF signal to the FTS system. Finally, the FTS measurement system is discussed and the measurement results correlated to the Mark III electron beam characteristics.

2.1 FEL E-Beam Theory

The signal measured in these experiments is produced by a beam of bunched electrons with relativistic velocities traveling down a conductive pipe. An understanding of the RF signal produced by this beam can be achieved by first analyzing the signal produced by a sinusoidal charge density. The sinusoidal results are then used to analyze the signal produced by a bunch (i.e., a weighted sum of sinusoid densities). Finally, in this section, the single bunch results are generalized for a periodic train of bunches.

2.1.1 Field produced by single charge with relativistic velocity

In the next sections it is useful to know how the coordinates and fields transform from a moving frame to a stationary frame. This section uses the results from [Wangsness, 1986] which is a particularly lucid discussion of the effects of relativity on

Maxwell's equations. Assume we place an electron at the origin of a frame moving with velocity $\vec{v}=v\,\hat{x}$ relative to the coordinate frame of the lab. For fields in the electron's frame (primed variables), the fields in the lab frame are found by the transformations [Wangsness, 1986]:

$$E_{\parallel} = E_{\parallel}' \quad E_{\perp} = \gamma\left(E_{\perp}' - \vec{v}\times B_{\perp}'\right)$$

$$B_{\parallel} = B_{\parallel}' \quad B_{\perp} = \gamma\left(B_{\perp}' + \frac{\vec{v}}{c^2}\times E_{\perp}\right) \tag{2.1}$$

where $\parallel$ and $\perp$ indicate parallel and perpendicular to the coordinate system velocity, $\vec{v}$. In addition, the coordinate transforms from the electron frame to the lab frame are,

$$x'= \gamma(x-vt), \qquad y'=y, \qquad z'=z, \qquad t'=\gamma(t-vx/c^2) \tag{2.2}$$

where $\gamma= (1-(v/c)^2)^{-1}$, and c is the speed of light.

The field measured at location r' of a charge q located at the origin in the moving frame is

$$\vec{E}'(x',y',z',t) = \frac{q}{4\pi\varepsilon_o}\frac{\vec{r}'-\vec{r}_e'}{\left|\vec{r}'-\vec{r}_e'\right|^3}$$

$$= \frac{q}{4\pi\varepsilon_o}\frac{x'\hat{x}+y'\hat{y}+z'\hat{z}}{\left[x'^2+y'^2+z'^2\right]^{3/2}} \tag{2.3}$$

Using the transformation equations, the field in the lab frame is,

$$\vec{E}_{\parallel}(x,y,z,t) = \frac{q}{4\pi\varepsilon_o}\frac{\gamma(x-vt)\hat{x}}{\left[\gamma^2(x-vt)^2+y^2+z^2\right]^{3/2}}$$

$$\vec{E}_{\perp}(x,y,z,t) = \gamma\frac{q}{4\pi\varepsilon_o}\frac{y\hat{y}+z\hat{z}}{\left[\gamma^2(x-vt)^2+y^2+z^2\right]^{3/2}}$$

$$\vec{B}_{\perp}(x,y,z,t) = \frac{\gamma v}{c^2}\frac{q}{4\pi\varepsilon_o}\frac{-z\hat{y}+y\hat{z}}{\left[\gamma^2(x-vt)^2+y^2+z^2\right]^{3/2}} \tag{2.4}$$

These equations show that as the charge nears the speed of light, the field measured in the lab frame appears to flatten in the direction of travel. Consider an observer in the

lab frame, located at $x=y=0$, $z=z_o$, measuring the field produced by the relativistic electron as it goes past. As γ increases, the observer will see the temporal extent of the fields produced by the electron decrease.

2.1.2 Field produced by relativistic sinusoidal charge density

The electron beam driving the FEL is a pulsed beam of relativistic electrons. To understand the fields produced by this beam (and hence its characteristic RF spectrum) first consider the fields produced by a periodic charge density traveling through a cylindrical conductive pipe as shown in figure 2-1. In the frame of the electrons (primed coordinates), the line charge density Λ', in cylindrical coordinates is

$$\Lambda'(z') = q\Lambda'_o \cos(\kappa'z')\delta(r') = \text{Re}\{q\Lambda'_o \exp(j\kappa'z')\delta(r')\} \tag{2.5}$$

where $\delta(r')$ indicates the line charge is located in the center of the pipe, κ' is the charge density spatial frequency modulation, and $q\Lambda_o$ is the peak charge density. Assuming a solution periodic in z', yields,

$$\vec{E}(r',z') = \text{Re}\left\{\hat{r}\frac{q\Lambda_o}{2\pi\varepsilon_o}\frac{1}{r'}\exp(j\kappa'z')\right\} \tag{2.6}$$

The charge density terminating the field lines on the surrounding conductive wall is,

$$\Lambda'_w(z') = \frac{q\Lambda'_o}{2\pi b}\cos(\kappa'z')\delta(r' - b)$$

Equation (2.6) is transformed from the electron rest frame to lab coordinate frame using,

$$z' = \gamma(z - \text{v}t) \qquad\qquad r' = r \qquad\qquad E_r = \gamma E_{r'} \tag{2.7}$$
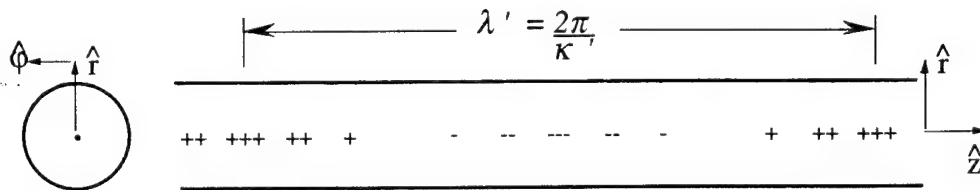
Fig. 2-1. Sinusoidal line charge inside a conductive pipe.

where $\gamma = (1 - (v/c)^2)^{-1/2}$, v is the velocity of the electrons, and c is the speed of light. Applying (2.7) to (2.6) yields the lab frame fields in terms of κ',

$$\vec{E}(r, z, t, v, \kappa') = \text{Re}\left\{\hat{r}\, \frac{\gamma q \Lambda'_o}{2\pi\varepsilon_o}\frac{1}{r} \exp(j\kappa'\gamma(z - vt))\right\} \tag{2.8}$$

$$\vec{H}(r, z, t, v, \kappa') = \text{Re}\left\{\hat{\varphi}\, \frac{\gamma q \Lambda'_o}{2\pi\varepsilon_o\eta}\frac{1}{r} \exp(j\kappa'\gamma(z - vt))\right\} \tag{2.9}$$

Recalling from transmission line theory [Shen and Kong, 1983], the fields for a wave propagation along a coaxial transmission line are,

$$\vec{E}(r,z) = \text{Re}\left\{\hat{r}\frac{V_o}{r}\exp(j(kz - \omega t))\right\} \tag{2.10}$$

$$\vec{H}(r,z) = \text{Re}\left\{\hat{\varphi}\frac{V_o}{r}\exp(j(kz - \omega t))\right\} \tag{2.11}$$

The important thing to note about equations (2.8) and (2.9) is that they are of the same form as (2.10) and (2.11), with the substitutions,

$$\kappa'\gamma v = \omega \tag{2.12}$$

$$\kappa'\gamma = k \tag{2.13}$$

$$\frac{\gamma q \Lambda'_o}{2\pi\varepsilon_o} = V_o \tag{2.14}$$

Therefore, the propagation of the fields generated by a relativistic electron beam may be analyzed using all the tools available from transmission line theory.

When interpreting (2.8) and (2.9) it is important to understand that the linear accelerator preserves temporal differences in the lab frame. This means that if an two electrons are launched into the LINAC at times t_1 and t_2, then the electrons will emerge from the output of the LINAC at times $t_1 + t_{acc}$ and $t_2 + t_{acc}$, i.e., the time delay between electrons, measured in the lab frame, is preserved by the acceleration process.

2.1.3 Field produced by an arbitrary shaped line charge density

By generalizing the results of the previous section, the field from a single arbitrary shaped bunch moving with relativistic velocity can be analyzed using Fourier transform techniques. A line charge density function (in the electron frame) $\Lambda'(z')$ can be equivalently represented by its spatial frequency density, $\tilde{\Lambda}'(\kappa')$,

$$\Lambda'(z') = \frac{1}{2\pi} \int_{-\infty}^{\infty} \tilde{\Lambda}'(\kappa') e^{j\kappa' z'} d\kappa'$$

$$\tilde{\Lambda}'(\kappa') = \int_{-\infty}^{\infty} \Lambda'(\xi) e^{-j\kappa' \xi} d\xi$$

(2.15)

Using superposition and (2.6), the field (observed in the electron frame) produced by the bunch is,

$$\vec{E}(r', z') = \int_{\kappa = -\infty}^{\infty} \hat{r} \frac{q\tilde{\Lambda}'(\kappa')}{2\pi\varepsilon_o} \frac{1}{r'} \exp(j\kappa z') d\kappa$$

$$= \frac{q\Lambda'(z')}{2\pi\varepsilon_o r'} \hat{r}$$

(2.16)

Transforming (2.16) into the lab frame yields,

$$\vec{E}(r, z, t) = \frac{\gamma q \Lambda'(\gamma(z - vt))}{2\pi\varepsilon_o r} \hat{r}$$

(2.17)

A few aspects of equation (2.17) are worth emphasis. Observed in the lab frame, Λ' is a wave traveling in the $+\hat{z}$ direction. Also, the field in the lab frame produced by the bunch has a temporal extent that is scaled by γ from the electron frame. As electron bunch energy increases (larger γ), an observer in the electron frame would see objects in the lab frame contract in the direction of apparent travel. In the lab frame, an observer would see objects in the electron frame contract by γ in the direction of travel. This is a consistent restatement of Lorentz contraction: an object of length $L\gamma$, in the moving frame, will have a length L when measured in the rest frame. Finally, the leading factor

γ in the numerator is a result of charge conservation; even though the charge density appears to change from transforming from the electron frame to the lab frame, the overall number of charges remains constant. Therefore, as the charge density function, Λ', is contracted in the lab frame by γ, the total charge density must increase proportionally by γ. Using these three factors, the charge density function, Λ', in the electron frame can be related to a charge density function, Λ, in the lab frame,

$$\Lambda(t\text{-}z/v) = \gamma\Lambda'(\gamma(z\text{-}vt)) \tag{2.18}$$

Hence, (2.17) expressed entirely in lab frame functions becomes,

$$\vec{E}(r, z, t) = \frac{q\Lambda(t - z/v)}{2\pi\varepsilon_o r}\,\hat{r} \tag{2.19}$$

$$\vec{H}(r, z, t) = \frac{q\Lambda(t - z/v)}{2\pi\varepsilon_o \eta r}\,\hat{\varphi} \tag{2.20}$$

Equations (2.19) and (2.20) relate the fields measured in the beam guide to the time dependent traveling charge density observed in the lab frame.

If we now sit at $z=0$, the frequency domain representation of field produced by the electron beam is given by Fourier transforming (2.19),

$$\begin{aligned}
\tilde{E}(r,\omega) &= \int_{t=-\infty}^{\infty} \vec{E}(r,t)\exp(-j\omega t)dt \\
&= \frac{q}{2\pi\varepsilon_o r}\int_{t=-\infty}^{\infty} \Lambda(t)\exp(-j\omega t)dt \\
&= \frac{q}{2\pi\varepsilon_o r}\tilde{\Lambda}(\omega) \tag{2.21}
\end{aligned}$$

Equation (2.21) predicts that the frequency spectrum of the electron bunch observed in the lab frame is directly related to the lab frame spatial frequency charge distribution; therefore electron beam charge distribution can be characterized by measuring the associated E or H fields in the beam guide. Figure 2-2 shows the field spectra, $\tilde{E}(r,\omega)$, for rectangular bunches with duration of one, two and five picoseconds.
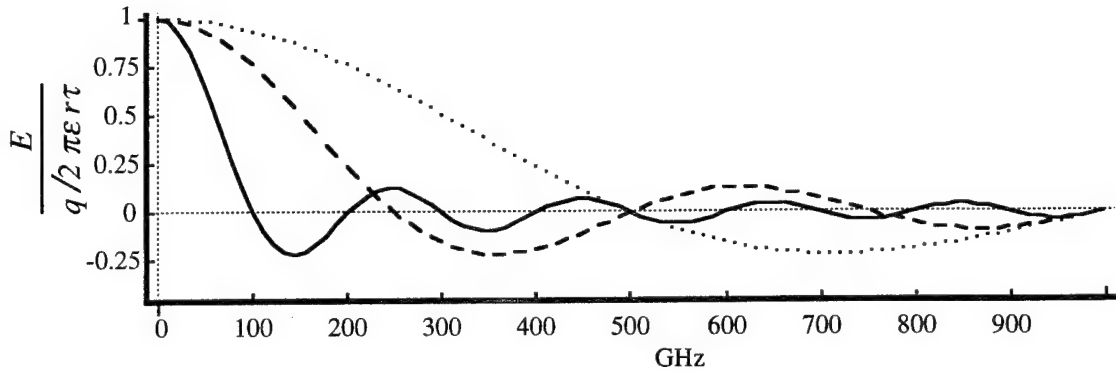
Fig. 2-2. Fourier transform of rectangular picosecond charge bunches. Bunch duration, τ_b, are 5 pS (solid,——), 2 pS (dashed,- - -), 1 pS (dotted,···).

2.1.4 Field produced by periodically launched charge bunches

The results of the previous section can now be extended to the case where, instead of just one bunch, bunches are launched down the beam pipe at periodic intervals. Mathematically, the field in the beam pipe (at $z=0$) is the convolution of (2.20) with an impulse train of period T_p,

$$\vec{H}_m(r,t) = rep_{T_p}\left(\vec{H}(r,t)\right) = \frac{q}{2\pi\varepsilon_o\eta r}\hat{\varphi}\sum_{n=-\infty}^{\infty}\Lambda\left(t - nT_p\right) \tag{2.22}$$

where $\vec{H}(r,t)$ is the field of single bunch, (2.20) (the subscript m means the field is due to a train of single bunches). The Fourier transform of a periodic field is no longer continuous, as in the single pulse case (figure 2-2), but is instead made up of discrete impulses, spaced by $2\pi/T_\pi$, mathematically the spectrum is written as,

$$\tilde{H}_m(\omega) = \frac{1}{T_p}comb_{1/T_p}\left(\tilde{H}(\omega)\right) = \frac{1}{T_p}\frac{q}{2\pi\varepsilon_o\eta r}\hat{\varphi}\tilde{\Lambda}(\omega)\sum_{n=-\infty}^{\infty}\delta\left(\omega - \frac{2\pi n}{T_p}\right) \tag{2.23}$$

This spectrum is periodic, hence we obtain a Fourier series; the original periodic signal is now represented as the weighted sum of sine or cosine functions of frequency $2\pi n/T_\pi$. This result is illustrated in figure 2-3 which uses the results from the previous section

where each bunch is five picoseconds long and bunches are launched every 350 picoseconds.
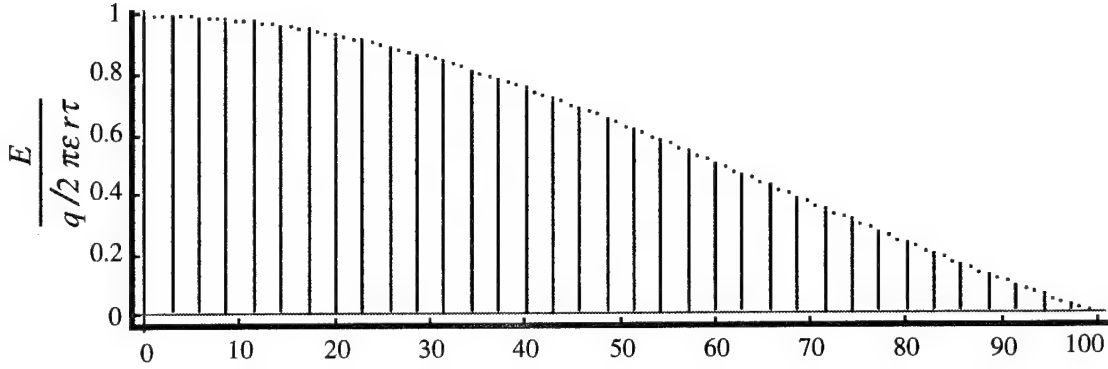
Fig. 2-3. Fourier transform of a periodic train of electron bunches. The duration of each bunch is 5 pS. The bunch launch period, T_p, is 350 pS, yielding a spectral spacing, δf, of 2.85 GHz. For clarity, the spectrum is shown only to 100 GHz; true spectral content would extend to infinity (see figure 2-2).

2.1.5 Field produced by groups of bunches

In the actual FEL, the train of electron bunches is not produced continuously, instead, the bunch train is chopped as shown in figure 2-4. Because the timing of individual electron bunches is controlled by a master clock, between pulse trains, the individual phase is preserved. Because the individual electron bunch is sometimes called a "micro pulse", the group of electron bunches is called a "macro pulse". Therefore, macro pulse formation is equivalent to an envelope function, $M(t)$, periodically modulating the pulse train[†],

$$\vec{H}_M(r,t) = rep_{T_M}\big(M(t/b)\big) * \vec{H}_m(r,t) \tag{2.24}$$

with the transform,

[†] At the Duke Mark III FEL, macro pulses are one to four microseconds in duration and are generated at a rate of one to sixty Hertz.
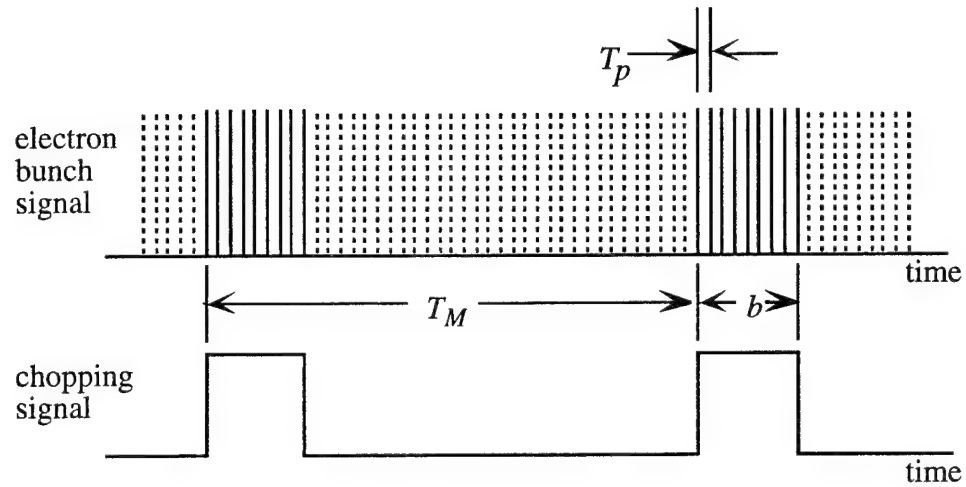
Fig. 2-4. Timing of chopped train of electron bunches. Each group of bunches has a duration b and the group period is T_M. The period between electron bunches is T_p. Because the individual electron bunches are called "micro pulses", the groups are called "macro pulses".

$$\tilde{H}_M(\omega) = \frac{1}{T_M} comb_{1/T_M}\left(\frac{1}{b}\tilde{M}(b\omega)\right) \otimes \tilde{H}_m(\omega) \qquad (2.25)$$

where T_M is the macro pulse period and b is the macro pulse duration.

In real measurements performed on actual beam systems, $T_M \gg b$. In the Duke Mark III, $T_M \approx 0.1$ -1 S, $b \approx 1$ to 4 µS, and $T_p \approx 350$ pS. The large timing difference between T_M and b coupled with the resolution limits of most spectrometers means that for practical measurements (2.25) simplifies to

$$\tilde{H}_M(\omega) \approx \frac{1}{b}\tilde{M}(b\omega) \otimes \tilde{H}_m(\omega) \qquad (2.26)$$

Figure 2-5 illustrates the results of (2.26) for a four microsecond long macro bunch.
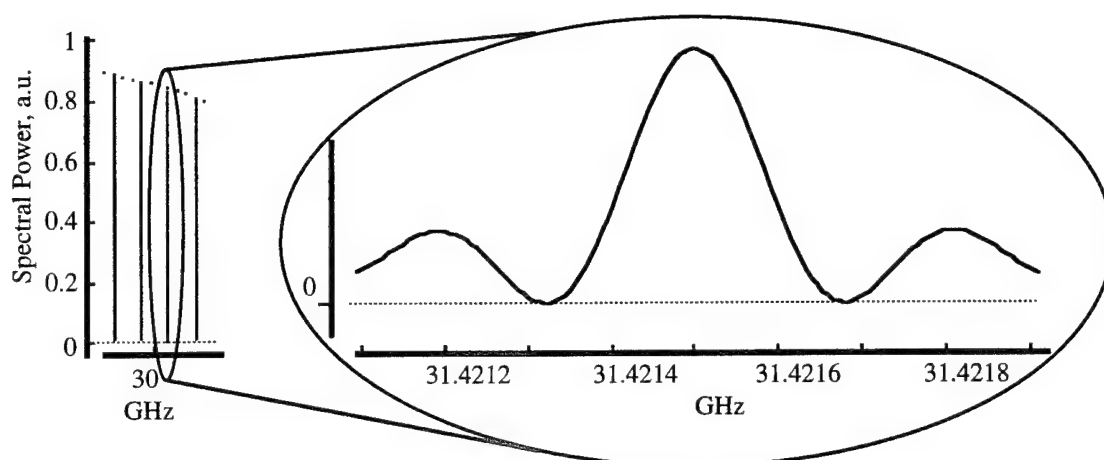
Fig. 2-5. Spectrum due to finite bunch train length. Enlargement of spectrum for 5 pS bunches in a 4 µS duration bunch train. The eleventh harmonic component of a 2.8565 GHz fundamental is shown.

2.1.6 Summary of RF from relativistic electron bunches

Equations (2.22), (2.23), and (2.26) relate the longitudinal charge distribution of the electron bunches to the electromagnetic field propagating with them along the beam pipe. Hence, measuring the propagating field is equivalent to measuring the longitudinal charge distribution. The next two sections address how the propagating field may be coupled out of the beam pipe, and how the field is actually measured.

2.2 Waveguide Coupling and Signal Transmission Theory

As discussed in the first chapter, a variety of methods have been applied to problem of sampling the field of an electron beam. These prior techniques have been relatively narrow band in nature, yielding only average macro pulse information. For this project a wide bandwidth coupling is required. Fortunately, a simple rectangular waveguide pickup, shown in figure 2-6, yields sufficient bandwidth for this project. In addition, a low loss beam line is required to the bring the signal from the pickup to the measurement system. Overmoded circular waveguide fits the electrical requirements

and is inexpensive and easy to use. This section will analyze the characteristics of both the coupling waveguide and the transmission waveguide.

2.2.1 Sampling waveguide pickup analysis

Calculating the exact nature of the frequency dependence of the coupling is a difficult problem, however it is possible, using waveguide theory, to calculate the nature of frequency response of the rectangular waveguide pickup shown in figure 2-6.
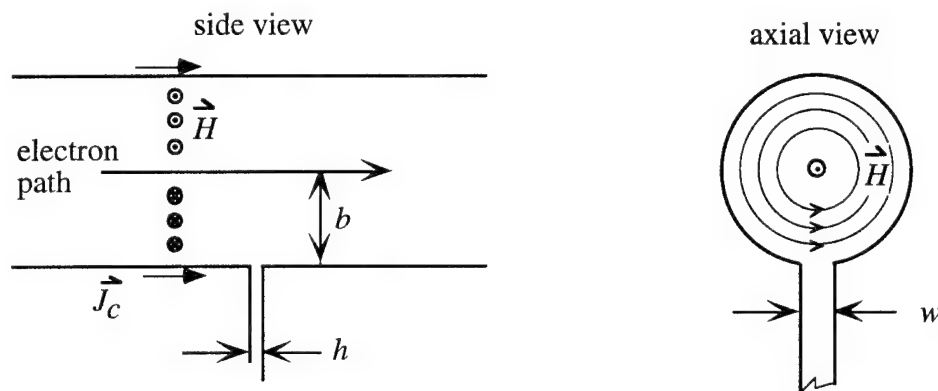
Fig. 2-6. Waveguide geometry for coupling RF from cylindrical electron beam pipe into rectangular pickup. The rectangular waveguide has height, h, and width, w, and extends to a short horn section (not shown). The electron bunch generates an EM transient that propagates down the beam pipe. The boundary conditions at the conducting wall of the beam pipe require a conduction current, J_c, which also travels with the electron bunch.

As shown in figure 2-7, the tangential magnetic field will be distorted by the opening of the waveguide pickup. To satisfy the boundary conditions imposed by the aperture, a field must propagate in the waveguide pickup. By using a theory of field equivalence at an aperture [Collin, 1960, pp. 285-8; Jackson, 1975, pp. 409-11] the waveguide field must satisfy,

$$\hat{n} \times \vec{H}_{wg} = \vec{J}_c = \hat{n} \times \vec{H}_{electron\_beam} \tag{2.27}$$
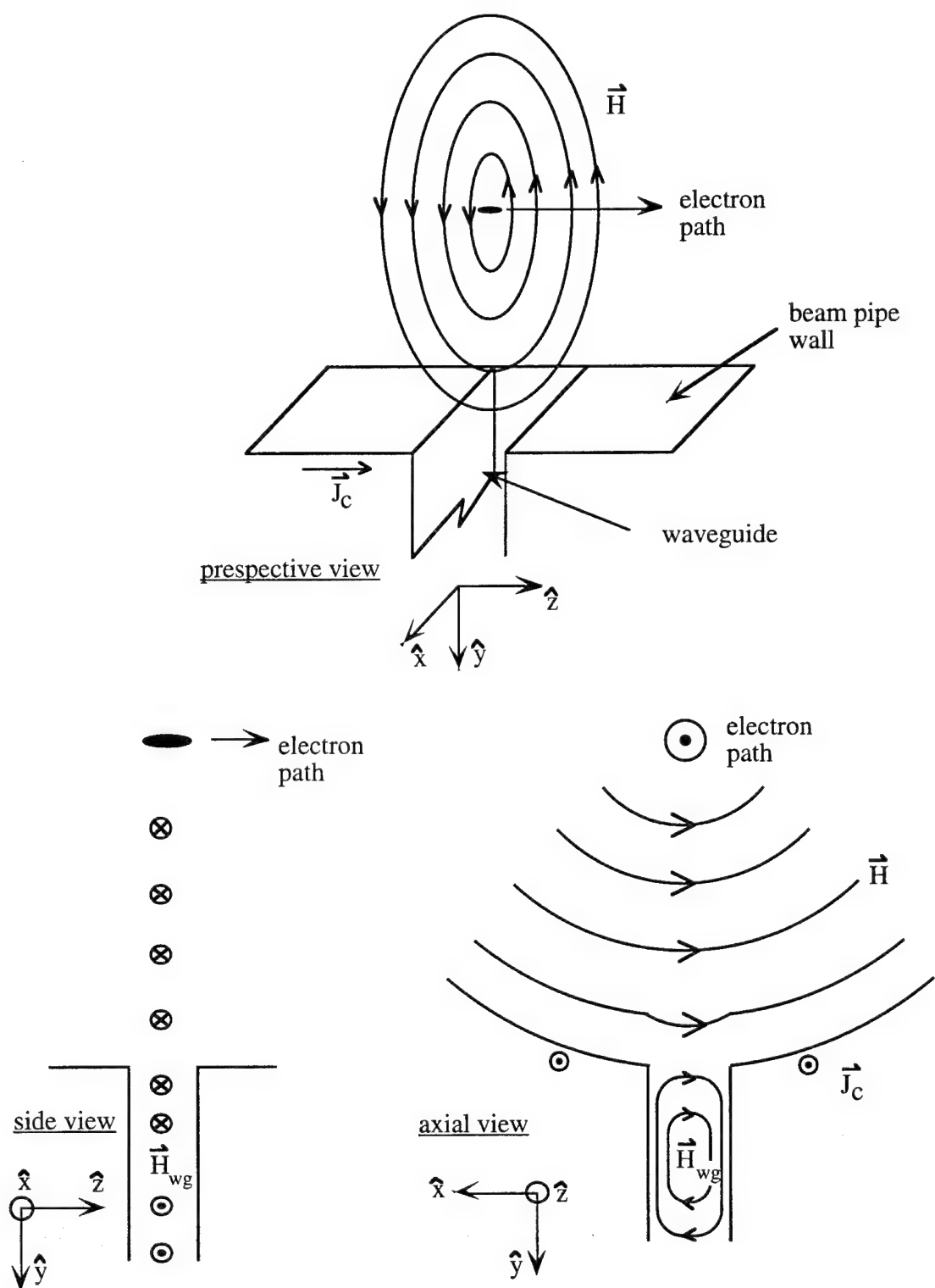
Fig. 2-7. Detail of electron beam fields coupling into waveguide.

across the aperture formed by the waveguide entrance ($\hat{n}$ is the unit vector normal to the aperture surface). For this project it is sufficient to understand the temporal nature of the field coupled into the rectangular pickup; from (2.27) it is clear that the field initially launched into the pickup waveguide will have the same temporal evolution as the relativistic electron bunch.

Although (2.27) describes the field launched into the waveguide pickup, the low frequency cutoff, f_c, of the sampling waveguide is determined by the waveguide cutoff condition,

$$f_c = \frac{1}{2\sqrt{\mu\varepsilon}}\sqrt{\left(\frac{m}{w}\right)^2 + \left(\frac{n}{h}\right)^2}$$

(2.28)

where m and n are the mode indices for the TE_{mn} and TM_{mn} modes. Applying (2.28) to the dimensions of the pickup waveguide used in this work ($w = 3.81$ mm and $h = 1.27$ mm), the lowest order mode (TE_{10}) has a cutoff of 39.4 GHz. Table 2-1 gives cutoff frequencies for other modes. Because other modes have yet higher cutoffs, the predominant mode coupled into the waveguide will be TE_{10}. As discussed in the next section the electron beam may excite higher modes in the pickup waveguide. For a given mode, the power propogating through the guide will be the product of the waveguide impedance and the coupling efficency.

Table 2-1. TE_{m0} cutoff frequencies for 1.27 mm x 3.81 mm waveguide.

m	Cutoff Freq. (GHz)
1	39.4
3	118
5	196
7	275
9	354
11	433

In summary, (2.27) predicts the pickup waveguide will couple a field whose time evolution (and frequency content) is initially that of the bunched electron beam. However, waveguide cutoff imposes a low frequency cutoff on the transmitted signal.

2.2.2 An Alternative Pickup - Electron Beam crossing a Waveguide.

Figure 2-8 shows an alternative method for coupling energy out of an electron beam and into a waveguide mode (this structure is reminiscent of the catcher structure in a klystron [Collin, 1966, see §9.7]). In this design, as the electron bunch passes through the center of the waveguide, a supported waveguide mode will extract energy from the electron bunch when the field decelerates the bunch. Alternatively, acceleration of the electron will extract energy from the field. During the electron's transit across the guide, energy will be alternately extracted and returned to the electron bunch from the waveguide field. Consideration of the time average E-field coupled from the electron beam and into the waveguide modes yields the high frequency coupling response.

During the electron beam transit, the electron beam energy couples into the waveguide mode over the entire period of waveguide mode oscillation. Averaging the coupling over the time required for the bunch to cross the entire gap , the time average of the coupling into a waveguide mode, with frequency ω, is

$$
\frac{1}{\tau_t} \int_{-\tau_t/2}^{\tau_t/2} \cos(\omega t + \phi)dt
$$
$$
= \frac{\sin(\omega \tau_t / 2 - \phi) + \sin(\omega \tau_t / 2 + \phi)}{\omega \tau_t}
$$

(2.29)

where the transit time, τ_t, is the time required for the electron to transit the guide. The result is that for some frequency components, energy coupled from the electron beam during part of the beam transit is returned during a later part of transit. For some frequencies no energy will be coupled from the electron beam to the waveguide; for

other frequencies a reduced amount of energy will be coupled into the beam. This

rolloff of energy coupling versus frequency is shown as the solid line in figure 2-9.
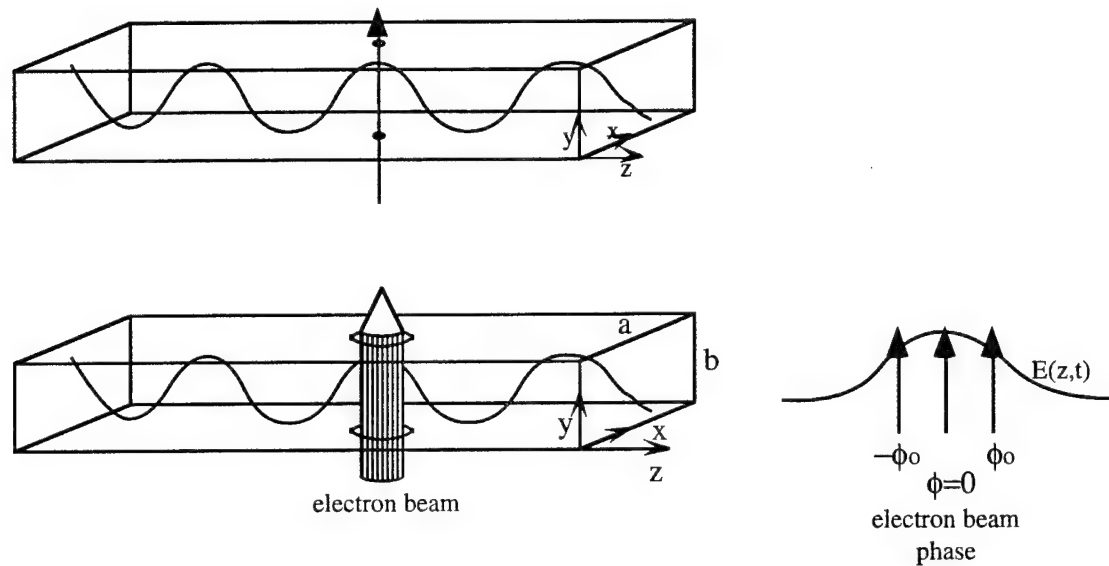
Fig. 2-8. Geometry for coupling electron beam energy into a waveguide
mode. The top geometry is for the ideal case in which the electron beam
size is much smaller than the mode wavelength. The bottom geometry
shows a real electron beam with non-negligible diameter; the detail to
the right shows the relative coupling different portions of the electron
beam to different phases of the driven wave.

The traditional waveguide coupling response model stops here. However, the

traditional analysis assumes that the electron beam crosses the waveguide over an

infinitesimally narrow (compared to wavelength) section of the longitudinal waveguide

dimension. However, for small waveguide dimensions, and comparably large electron

beams, the electron beam couples energy into the waveguide mode over a range of

phase angles (bottom right of figure 2-8). Equation (2.29) gives the power coupled at

phase ϕ for a TE_{10} mode. The phase angle ϕ varies from $\pm\omega z_b/2c$ over the electron

beam width, z_b. Rewriting this phase angle in terms of an effective phase delay time,

$t_p = z_b/c$, yields $\phi = \omega\, t_p$. Averaging over this range of phases is now equivalent to averaging over the effective phase delay time,

$$\frac{1}{\tau_p} \int_{-\tau_p/2}^{\tau_p/2} \frac{\sin\left(\omega\tau_t/2 + \omega\tau_p\right) + \sin\left(\omega\tau_t/2 - \omega\tau_p\right)}{\omega\tau_t}\, d\tau_p$$

$$= \quad 2\,\frac{\cos\left(\omega\tau_t/2 - \omega\tau_p/2\right) - \cos\left(\omega\tau_t/2 + \omega\tau_p/2\right)}{\omega\tau_p * \omega\tau_t} \qquad (2.30)$$

$$= \quad \frac{\cos\left(\omega(\tau_t - \tau_p)/2\right) - \cos\left(\omega(\tau_t + \tau_p)/2\right)}{\omega\tau_p * \omega\tau_t/2}$$

Note that in the above equation in the limit $\omega\,\tau_p \Rightarrow 0$, the numerator becomes $\sin(\omega\,\tau_t/2)$ which is the traditional result.

Figure 2-9 graphs this effect for a 1 mm and 2 mm electron beam diameter crossing a guide with a 6 pS transit time (waveguide cutoff is ignored for this example). Note that the effect of the electron beam width becomes important when the transit time and the electron phase time are of the same order. Also note that the electron beam width substantially reduces the coupling into higher frequency modes.
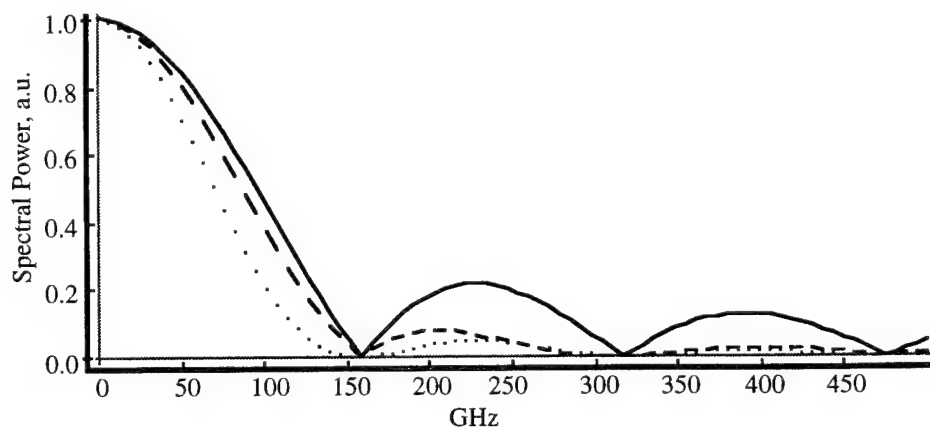
Fig. 2-9. Frequency response for wide electron beams crossing a waveguide. All plots for electron beam with 6 pS transit time. Solid curve, ideal beam, $\tau_p=0$; dashed curve, 1 mm beam diameter, $\tau_p=3.3$ pS; dotted curve, 2 mm beam, $\tau_p=6.6$ pS.

Finally, the traditional waveguide coupling analysis only considers TE_{10} coupling; because of the broadband nature of the electron signal, this simplification is not valid. From waveguide theory, the TE_{mn} electric field across a waveguide is proportional to,

$$E_x \propto \cos(m\pi x/a) \cos(n\pi y/b)$$

Adding a higher order mode term to (2.29) yields the coupling equation for any TE_{1n} mode,

$$\frac{1}{\tau_t} \int_{-\tau_t/2}^{\tau_t/2} \cos\left(\frac{n\pi y}{b}\right) \cos(\omega t + \phi)dt =$$

$$\frac{1}{\tau_t} \int_{-\tau_t/2}^{\tau_t/2} \cos\left(\frac{n\pi t}{\tau_t}\right) \cos(\omega t + \phi)dt = \tag{2.31}$$

$$\left\{ \frac{\sin\left((n\pi/2) - \omega\tau_t/2\right)}{n\pi - \omega\tau_t} + \frac{\sin\left((n\pi/2) + \omega\tau_t/2\right)}{n\pi + \omega\tau_t} \right\}$$

where the change of variables, $y = tcb/\tau_t$ has been used (b is the waveguide height). This equation predicts the frequency dependence of the waveguide coupling for the nth TE_{1n} mode. Figure 2-10 shows the magnitude of the coupling for TE_{10}, TE_{11}, and TE_{12} modes. Also shown is the magnitude of the sum of the three fields coupled, corrected for mode cutoff, for both negligible beam width and 1 mm beam diameter. This figure is significant because it shows that higher order waveguide modes, in addition to non-negligible electron beam diameter, have a considerable effect on the response spectrum of the waveguide. By including increasingly higher order modes, this model could predict the coupling in the waveguide pickup of §2.2.1.
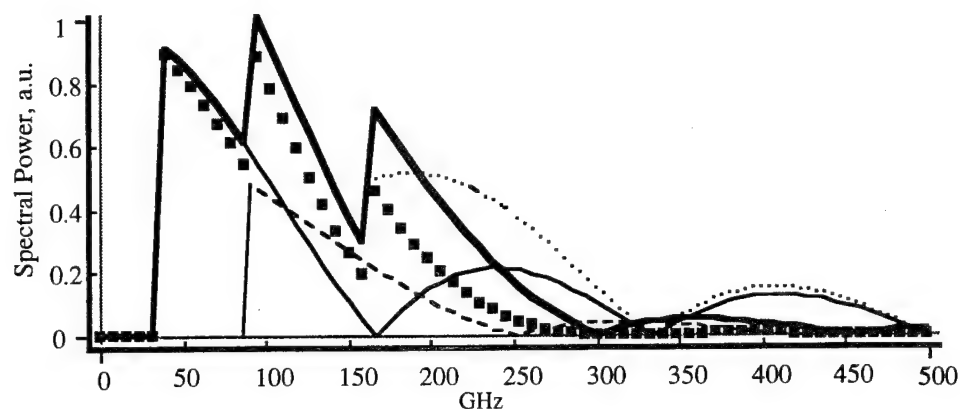
Fig. 2-10. Waveguide coupling of TE_{1n} modes. Solid thin curve is TE_{10} coupling; dashed curve is TE_{11} coupling; dotted curve is TE_{12} coupling; solid bold curve is magnitude of the sum of the three mode; squares are sum of three modes corrected for 1 mm diameter electron beam. Breaks in curves indicate mode cutoff frequency. (Model waveguide dimensions, 2 mm x 4 mm.)

Like the previous coupling geometry, the electron bunch passing through a waveguide will couple a field whose time evolution (and frequency content) is initially that of the bunched electron beam. However, due to cutoff for the various modes supported in the waveguide, the frequency response of this geometry is complicated. In addition, the high frequency operation is limited by the non-negligible width of the electron beam. Nonetheless, the simplicity of this coupling structure makes it an attractive device.

2.2.3 Waveguide attenuation and dispersion characteristics

The EM pulse generated by the pickup waveguide must be transmitted from the pickup to the measurement equipment with little distortion. Already, it has been shown how the pickup waveguide produces both a low frequency cutoff and a transit time dependent high frequency rolloff. In addition to these effects, the pickup waveguide and the transmission waveguide produce non-negligible attenuation and dispersion.

Ramo [Ramo, et al., 1984] and Wadell[Wadell, 1991] produce concise analyses of waveguide attenuation. The attenuation constants for TE_{mn} and TM_{mn} modes in

rectangular waveguide (geometry shown in figure 2-11), are [Wadell, 1991, eq. 3.10.1.4 & 3.10.1.6],

$$\alpha_{RTE_{m,n}} = \frac{2R_s}{h\eta\sqrt{1-(f_c/f)^2}}\left\{\left(1+\frac{h}{w}\right)\left(\frac{f_c}{f}\right)^2 + \left(1-\left(\frac{f_c}{f}\right)^2\right)\left[\frac{h}{w}\frac{\left[\left(\frac{h}{w}\right)m^2+n^2\right]}{\left(\frac{hm}{w}\right)^2+n^2}\right]\right\} \quad (2.32)$$

$$\alpha_{RTM_{m,n}} = \frac{2R_s}{h\eta\sqrt{1-(f_c/f)^2}}\frac{(h/w)^3 m^2+n^2}{(hm/w)^2+n^2} \quad (2.33)$$

where f_c is the cutoff frequency for the mode given by (2.28) and R_s is the waveguide surface resistivity, defined by [Ramo, et al., 1984, p. 153],

$$R_s(f) = k\sqrt{f} \quad (2.34)$$

where k is a material specific constant (for copper, $k = 2.61\times10^{-7}\ \Omega\ Hz^{-1/2}$; for aluminum, $k = 3.26\times10^{-7}\ \Omega.Hz^{-1/2}$). Figure 2-12 shows the attenuation for aluminum waveguide with the dimensions used in the Mark III pickup. Although the attenuation more than doubles from cutoff to 1 THz, for a 5 cm aluminum waveguide section (used in the Mark III pickup) the attenuation is negligible.
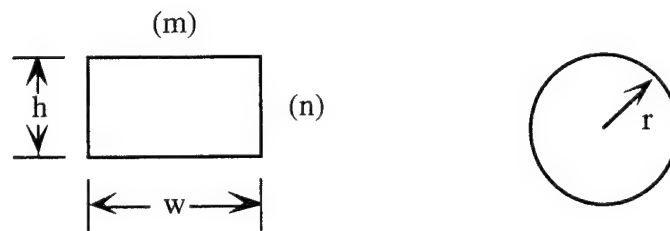
Fig. 2-11. Schematic indicating geometry of rectangular and round waveguides.
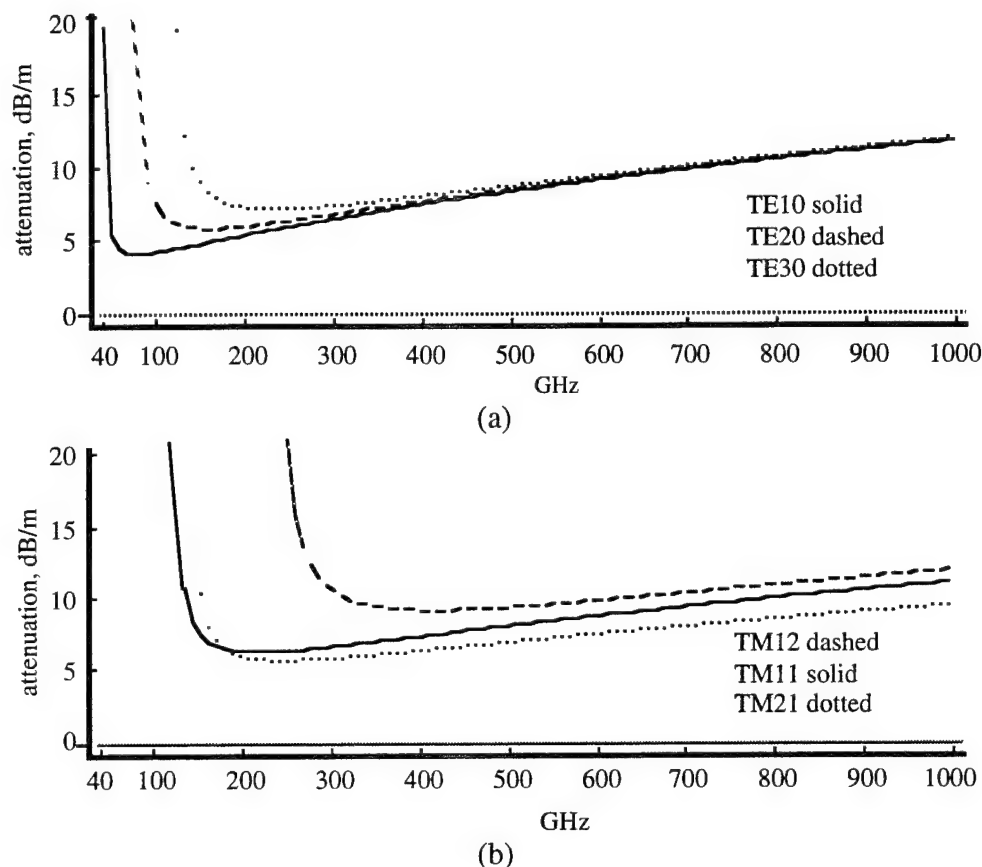
Fig. 2-12. Attenuation due to wall loss in rectangular waveguide. Results are plotted for waveguide dimensions found in the Mark III RF pickup. (a) gives the attenuation for various TE modes, (b) gives the attenuation for various TM modes.

Because the transmission waveguide from the pickup to the FTS is cylindrical copper pipe, it is also useful to have expressions for the attenuation constants for circular waveguide. For waveguide of diameter r, [Wadell, 1991, eq. 3.10.2.3 & 3.10.2.4] gives the attenuation constants as,

$$\alpha_{CTM} = \frac{R_s}{\eta r} \frac{1}{\sqrt{1 - (f_c/f)^2}} \tag{2.35}$$

$$\alpha_{CTE_{mn}} = \frac{R_s}{\eta r} \frac{1}{\sqrt{1 - (f_c/f)^2}} \left[\frac{m^2}{p_{m,n}'^2 - m^2} \right] \tag{2.36}$$

where $R_s(f)$ is found using (2.34), and $p'_{m,n}$ is the nth zero of the derivative of the mth order Bessel function (values listed in Table 2-2).

Table 2-2. Values of the nth zero of the derivative of the mth order Bessel functions [Collin, 1960, p. 196]

p'_{mn}	$m=0$	$m=1$	$m=2$
$n=1$	3.832	1.841	3.054
$n=2$	7.016	5.331	6.706
$n=3$	10.173	8.536	9.969

The computed attenuation for copper waveguide used in the signal transmission system used in this research is shown in figure 2-13. Although the TE_{01} mode has the most advantageous attenuation characteristic, the mode most excited by the rectangular pickup waveguide will be the TE_{11} mode. In this case there is a substantial frequency dependent attenuation which will effect the pulse shape.
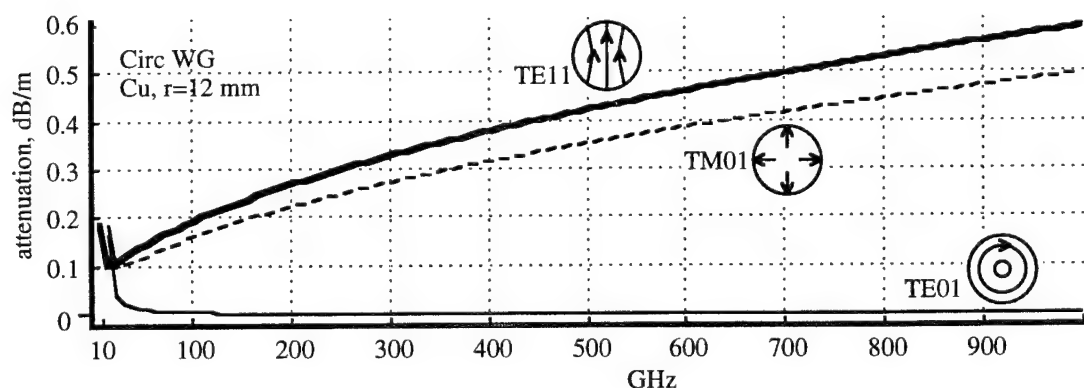
Fig. 2-13. Attenuation constant vs. frequency in circular waveguide. Plotted values for 12 mm radius copper waveguide.

Because the pulses studied in this project have broad spectral content, frequency dependent phase velocity, or dispersion, in the waveguides must also be analyzed. A frequency domain model of dispersion was used [Ramo, et al., 1984, p. 446]. If a pulse has a shape $f(t-z/v_p)$ in the time domain then in the frequency domain the signal is,

$$f\left(t - \frac{z}{v_p}\right) \Leftrightarrow F(\omega)\exp\left(-\omega \frac{z}{v_p}\right)$$

where, $f(t)$ and $F(\omega)$ are Fourier transform pairs. Dispersion during transmission results in frequency dependent phase velocity, $v_p(\omega)$. For the case of waveguide (as opposed to material) dispersion, above cutoff, ω_{cutoff}, the phase velocity of a component of angular frequency ω, is,

$$v_p(\omega) = \frac{c}{\sqrt{1 - \left(\omega_{cutoff}/\omega\right)^2}} \tag{2.37}$$

If we know the pulse shape $f(t)$ at $z=0$, then we know $F(\omega)$ at $z=0$ (numerically this is computed using an FFT), and we can find the pulse shape at any arbitrary position, z, along the waveguide by taking the inverse Fourier transform of $F(\omega)$ multiplied by the frequency dependent propagation factor, $\exp(-j\omega z / v_p(\omega))$,

$$f(t,z) = FT^{-1}\left\{F(\omega)\exp\left(-j\omega \frac{z}{v_p(\omega)}\right)\right\} \tag{2.38}$$

The Fourier transforms can be performed by FFT algorithms; however, because the FFT assumes the signal is cyclical, for long delays (long propagation distances), the pulse will appear to cycle around the sampled window. One way to avoid this apparent cycling is to use a data set that is as long as the longest delay interval; this however increases computation time and memory requirements (a 3 pS pulse propagated 10 meters would require ≈ 50000 points). An alternative, used here, is to recognize that the center of the pulse will continue to propagate with a constant velocity c, that will determine the time delay of the pulse center at position z. By subtracting a constant

phase factor z/c from the argument of the exponential in (2.38), then numerically the pulse will appear to stay centered at $t=0$, although the frequency dependent phase velocity will produce a pulse broadening. The exact form of the computation used in the figure 2-14 is,

$$f_{dly}\left(t - \frac{z}{c}, z\right) = FT^{-1}\left\{F(\omega)\exp\left(-j\omega z\left(\frac{1}{v_p(\omega)} - \frac{1}{c}\right)\right)\right\} \tag{2.39}$$

Finally, note that below cutoff, the propagated wave is severely attenuated over even short distances [Bronwell and Beam, 1947, pg. 325] (the attenuation constant is $\approx 4/\lambda$ for frequencies just 20% below cutoff). Because all the simulations had signals propagating at least several wavelengths through the guide, in the models below, any frequency component below cutoff would be small and, hence, in the simulation was set to zero.

2.2.4 Waveguide characteristics summary

This section has shown that a simple rectangular waveguide provides adequate sampling of the RF field produced by the relativistic electron bunch. Although the initial signal coupled into the waveguide is temporally the same as that produced by the bunch, transit time effects, waveguide attenuation and cutoff, and dispersion all distort the RF signal as it propagates from the electron beam system to the analysis instruments. When examining the actual measured data these effects should be considered and may need to be compensated for in a final pulse analysis.
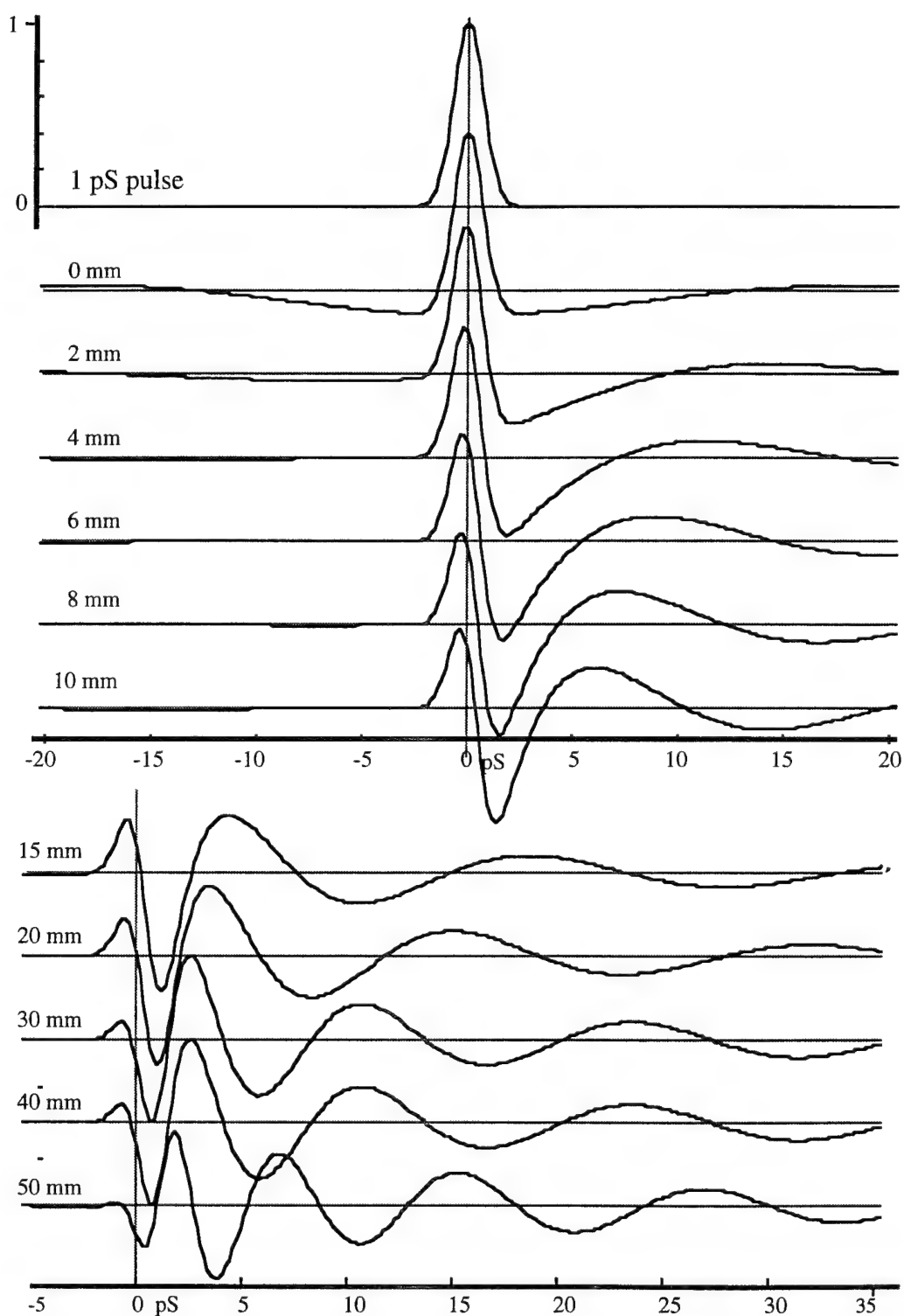
Fig. 2-14. Models of pulse dispersion through various length waveguide. Initial pulse is 1 pS gaussian. Waveguide cutoff frequency of 39.4 GHz, pulse period, 350 pS. Ordinate axis for each simulation is relative electric field.

2.3 Fourier Transform Spectroscopy Theory

As mentioned earlier, a Fourier transform spectrometer (FTS) made the majority of the electron beam signal measurements for this project (measurements made with a microwave spectrum analyzer are discussed later). Although typically used to produce frequency domain power spectra measurements, an FTS is equally useful for producing time domain, autocorrelation measurements. This is not surprising because the functions of autocorrelation and power spectra are Fourier transform pairs,

$$f(t) \oplus f(t) \quad \Leftrightarrow \quad |F(\omega)|^2 \tag{2.40}$$

Depending on the information required, one domain will often give more insight into the nature of the signal. Both time and frequency domain characteristics are used in this project. Although others have developed the theory of FTS measurements in great detail for non-transient sources [Bell, 1972; Connes, 1961; Connes and Connes, 1966; Guenther, 1990; Martin, 1982], only one reference [Greene, et al., 1991] was found addressing FTS systems for sub-picosecond transient measurements. This section will review briefly FTS theory, in both the time and frequency domain, emphasizing aspects that are important for analyzing pulsed sources.

The fundamental FTS is build around a Michelson interferometer, shown schematically in figure 2-15. To develop the basic FTS relationships in this section, assume the beam splitter is an ideal 50-50 splitter, and the mirrors are identical and are ideal reflectors (R=1) independent of frequency (later these restrictions will be dropped).
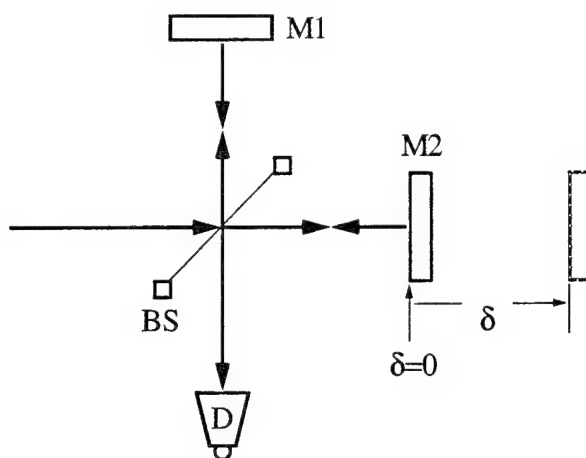
Fig. 2-15. Schematic of a Michelson interferometer used in a FTS. The beam path is shown by the thick arrows; the collimated beam from the source enters from the left, is split (by beam splitter BS) along two paths. Mirror M1 is fixed, while mirror M2 may be translated a displacement δ (dotted rectangle); M2 is at zero path displacement at δ=0. The beams from the fixed and variable path are recombined by the beam splitter, and focused into the detector, D.

2.3.1 Basic FTS Theory - Time Domain Analysis

The time domain analysis of the FTS begins by assuming that a planar collimated EM wave enters the interferometer; because this field is a solution of wave equation, then it must have a time domain form,

$$E(t,z) = E(t\text{-}z\,/c) \qquad (2.41)$$

This signal will propagate through the beam splitter, and a quarter of the wave will travel a path length z_1 from the beam splitter to the detector via the fixed mirror path. Another quarter of the wave will travel via the displaced mirror path a distance $z_1 + \delta$ to the detector. Hence the field at the detector is,

$$E_D(t,z) \propto E(t\text{-}z_1/c) \; + \; E(t\text{-}(z_1 + \delta)/c) \qquad (2.42)$$

Because the detector is sensitive to the time average intensity of the incident field, the signal produced by the detector as a function of mirror M2 displacement, δ, is,

$$D(t,\delta) \propto \langle I_D(t,\delta)\rangle$$

$$\propto \left\langle \left| E(t-z_1/c) + E\left(t-(z_1+\delta)/c\right)\right|^2 \right\rangle \qquad (2.43)$$

where the brackets indicate convolution of the impulse response , $h(t)$, of the detector, with the incident signal,

$$\langle f(t)\rangle \Rightarrow \int_{x=-\infty}^{\infty} h(t-x)f(x)dx \qquad (2.44)$$

Expanding (2.43) yields,

$$D(t,\delta) = \left\langle \left| E(t-z_1/c)\right|^2 \right\rangle + \left\langle \left| E\left(t-(z_1+\delta)/c\right)\right|^2 \right\rangle$$

$$+ 2\left\langle \mathrm{Re}\left[E^*(t-z_1/c) E\left(t-(z_1+\delta)/c\right)\right]\right\rangle \qquad (2.45)$$

In the limit $\delta/c \ll T_D$, the equivalent field displacement time is much less than the detector response time, therefore, the detector will not be able to resolve the two seperate pulses. In this slow detector regime, the first two terms of (2.45) are equal and proportional to I_E, the intensity of the incident field E; by evaluating $D(t,0)$, the first two terms sum to $D(t,0)/2$. Also, because z_1/c is yields a constant phase shift that is the same for the signals from both arms, (2.45) remains unchanged if we let $t-z_1/c \rightarrow t$. Expanding the integral of the third term of (2.45), using a change of variables, $u=t-x$, and rearranging terms, yields the desired result,

$$D(t,\delta) - \tfrac{1}{2}D(t,0) = 2\,\mathrm{Re}\left\{ \int_{x=-\infty}^{\infty} h(t-x)E^*(x)E(x-\delta/c)dx \right\} \qquad (2.46)$$

On a time scale of a micropulse, the detector response, $h(t)$, is constant, hence the integral in (2.46) is clearly the autocorrelation of the incident wave, where δ/c is the delay parameter. However, on the time scale of the macro pulse, the integration effectively produces the detector response convolved (in time) with the autocorrelation intensity. The signal from the detector will reflect the autocorrelation over a window of

time defined by the detector response. If the macro pulse duration is greater than this response time, then the signal from the detector will show the time evolution of the micro pulse autocorrelations from macro pulse beginning to end. In summary, by varying δ and sampling at the same time in subsequent macro pulses, (2.46) can be used to compute the micro pulse autocorrelation. In addition, by keeping δ fixed, the time evolution of (2.46) will be proportional to the pulse autocorrelation and hence, the micro pulse width variation during the macro pulse. As the experimental results will demonstrate, both techniques are valuable diagnostics.

2.3.2 Basic FTS Theory - Frequency Domain Analysis

Now it is possible, using the same assumptions as in the time domain analysis, to develop the frequency domain principles of Fourier transform spectroscopy, i.e., calculate the power spectrum of the incident EM wave from measurements of the detector signal at various mirror displacements, δ. Begin by considering the frequency domain form of the wave incident on the FTS; it is simply the Fourier transform of (2.41),

$$\tilde{E}(\omega,z) = \tilde{E}(\omega)e^{-j\omega z/c} \tag{2.47}$$

The frequency domain representation of the field reaching the detector is $\tilde{E}_D(\omega,\delta)$,

$$\begin{aligned} \tilde{E}_D(\omega,z) &\propto \tilde{E}(\omega)e^{-j\omega z_1/c} + \tilde{E}(\omega)e^{-j\omega(z_1+\delta)/c} \\ &\propto \tilde{E}(\omega)e^{-j\omega z_1/c}\left(1 + e^{-j\omega\delta/c}\right) \end{aligned} \tag{2.48}$$

A detector that produces a time domain time-average square law response, produces in the frequency domain a bandwidth limited autocorrelation response. Therefore, we can write the frequency domain equivalent of (2.43) as

$$\tilde{D}(\omega,\delta) \propto \tilde{H}(\omega) \int_{-\infty}^{\infty} \tilde{E}(\xi)e^{-j\xi z_1/c}\left(1 + e^{-j\xi\delta/c}\right)\tilde{E}^*(\xi-\omega)e^{j(\xi-\omega)z_1/c}\left(1 + e^{j(\xi-\omega)\delta/c}\right)d\xi \tag{2.49}$$

The leading $\tilde{H}(\omega)$ term is the detector frequency response function, whereas the integral is the autocorrelation of (2.48). Collecting terms, and rearranging yields,

$$\tilde{D}(\omega,\delta) \propto 2e^{-j\omega(z_1+\delta/2)/c}\tilde{H}(\omega)\left\{ \cos\left(\frac{\omega\delta}{2c}\right)\int_{-\infty}^{\infty}\tilde{E}(\xi)\tilde{E}^*(\xi-\omega)d\xi \right.$$
$$\left. +\int_{-\infty}^{\infty}\tilde{E}(\xi)\tilde{E}^*(\xi-\omega)\cos\left((\xi-\omega/2)\delta/c\right)d\xi\right\}$$

(2.50)

Equation (2.50) is a complicated mess, however, it is simplified as follows. Recall that a periodic pulsed source will have a periodic spectrum. By assuming that the periodic spacing of $\tilde{E}(\omega)$ is much greater than the detector bandwidth limiting function, then $\tilde{H}(\omega)$ will be zero for $\omega >> 2\pi/T_D$. Hence, (2.50) will have non-zero value for $\omega << 2\pi/T_D$. In this regime, the quantity, $\omega\delta/2c \approx 0$. In this limit, (2.50) simplifies to

$$\tilde{D}(\omega,\delta) \propto 2e^{-j\omega z_1/c}\tilde{H}(\omega)\left\{ \int_{-\infty}^{\infty}\tilde{E}(\xi)\tilde{E}^*(\xi-\omega)d\xi + \int_{-\infty}^{\infty}\tilde{E}(\xi)\tilde{E}^*(\xi-\omega)\cos\left(\xi\delta/c\right)d\xi\right\} (2.51)$$

Recognizing that the first integrand evaluates to $\tilde{D}(\omega,0)/2$ and taking up the leading phase delay in the detector response yields,

$$\tilde{D}(\omega,\delta) - \tfrac{1}{2}\tilde{D}(\omega,0) \propto 2\tilde{H}(\omega)\int_{-\infty}^{\infty}\tilde{E}(\xi)\tilde{E}^*(\xi-\omega)\cos\left(\xi\delta/c\right)d\xi$$

(2.52)

Equation (2.52) is a general result applicable for either pulsed or CW systems and for all detector responses. For the traditional FTS applications involving essentially CW sources with slow detectors, $\omega = 0$, and $\tilde{H}(\omega) = \delta(\omega) \cdot \tilde{H}(0)$, a constant. Equation (2.52) then becomes,

$$\tilde{D}(0,\delta) - \tfrac{1}{2}\tilde{D}(0,0) \propto \int_{-\infty}^{\infty}\left|\tilde{E}(\xi)\right|^2 \cos\left(\xi\delta/c\right)d\xi$$

(2.53)

It is important to note that the integrand in (2.53) is independent of any frequency dependent phase variation in $\tilde{E}$. Hence, an FTS using a square law detector is

insensitive to any dispersion present in the source signal. It is for this reason that the FTS is able to characterize signals with large dispersion.

Taking the Fourier transform of (2.53), and recognizing $\tilde{D}(0,\delta) = \langle D(t,\delta) \rangle$, yields the classical CW FTS relationship,

$$\left| \tilde{E}(c\sigma) \right|^2 \propto \mathsf{FT}\left\{ \langle D(t,\delta) \rangle - \tfrac{1}{2} \langle D(t,0) \rangle \right\} \tag{2.54}$$

The left hand side of (2.54) is the power spectra of the incident signal as a function wavenumber, σ. The argument to the Fourier transform on the right hand side of (2.54) is the DC signal measured by the detector as a function of mirror displacement (note that if δ is in units of cm then σ is in units of cm^{-1}). Note that assuming the initial pulse has phase equal to a constant for all frequencies, and dispersion is ignored, then taking the inverse transform of the square root of the left hand side of (2.54) will yield the original pulse shape.

2.3.3 Practical Corrections to Basic FTS Theory

Up to this point, the FTS system has been considered in its ideal operation. However, in actual operation the individual components of the FTS will alter the ideal response. In this section the practical effects of pulsed operation, beam splitter response, and micropulse echo effects, are briefly discussed.

We have seen that equations (2.54) and (2.46) are Fourier transform pairs; therefore, in general practice the FTS is used to measure the autocorrelation of a incident signal, and then the (phase independent) power spectra of the signal is computed using the Fourier transform. For measurements on signals which are modulated on and off (as are studied in this work), instead of taking the time average signal from the detector, the detector signal is sampled only during the period the signal is "on". This sampling has the effect of improving the autocorrelation signal to noise by

the ratio of the chopping period divided by the pulse sample width [Stremler, 1982, pg. 163],

$$\frac{(S/N)_{sampled}}{(S/N)_{averaged}} \approx \frac{T_M}{T_D} \qquad (2.55)$$

For the experiments run in this project, $T_M \approx 0.1$ s, $T_D \approx 1$ μS, giving a signal to noise improvement of $\sim 10^5$ when sampling instead of averaging.

In the actual interferometer, the dielectric beam splitter has a finite thickness so that it behaves like an etalon producing a periodic bandstop filter in the interferometer. The frequency dependence of the filtering is obtained by considering the transmission characteristics of the beam splitter which has been derived by [Chamberlain, et al., 1966]. For a beam splitter (figure 2-16) of thickness h, index n, and at and angle θ to the incident beam, the interferometer transmission coefficients for parallel and normal incidence are,

$$T_p = \frac{2R_p t_p^2 E}{\left(t_p^2 + R_p E\right)^2} \qquad T_n = \frac{2R_n t_n^2 E}{\left(t_n^2 + R_n E\right)^2}$$

where R_p, R_n, and E are defined as,

$$R_p = \frac{\sin^2(\theta - \theta')}{\sin^2(\theta + \theta')} \qquad R_n = \frac{\tan^2(\theta - \theta')}{\tan^2(\theta + \theta')} \qquad E = 4\sin^2\left(\frac{\omega}{c} hn\cos\theta'\right)$$

and $t_x = 1 - R_x$, and θ and θ' are related by Snell's law. For an unpolarized beam, the transmission will be an equal mix of both polarizations,

$$T_{unpolar} = \frac{1}{2}(T_p + T_n) \qquad (2.56)$$

Figure 2-17 shows the results of (2.56) for two thicknesses of mylar beam splitters oriented at 45°. Note that an ideal 50-50 beam splitter would yield 50% transmission. Figure 2-18 shows the effect on interferometer transmission versus the beam splitter incident angle.
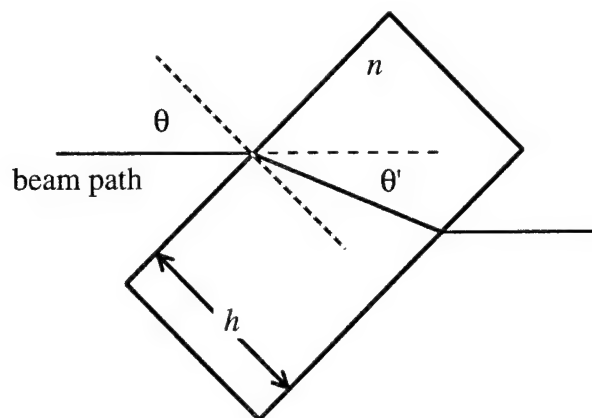
Fig. 2-16. Interferometer beam splitter geometry. Incident angle is θ, beam splitter index is n, and thickness is h.
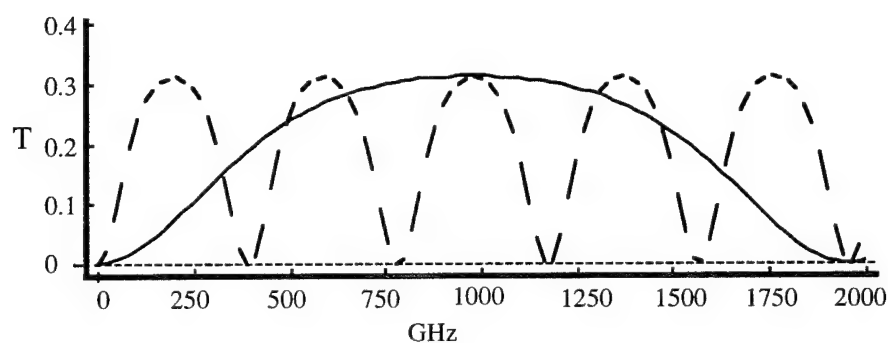
Fig. 2-17. Interferometer transmission for two thickness of mylar beam splitter. Incident angle is θ=45°, beam splitter index is 1.69. Beam splitter thickness: 50 μm (solid); 250 μm (dashed).
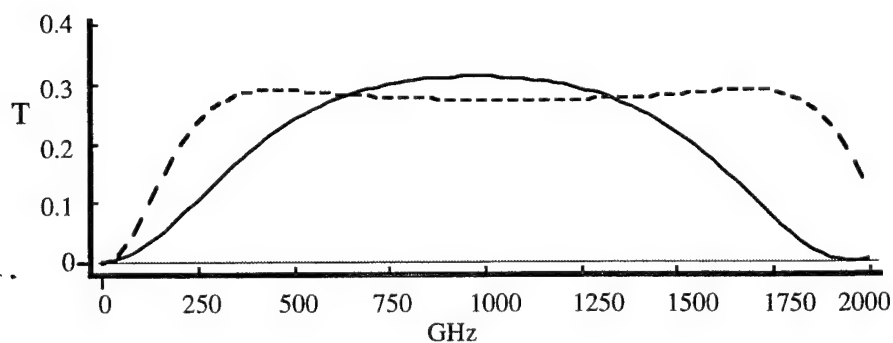
Fig. 2-18. Interferometer transmission for mylar beam splitter ($h=50 \mu m$) at two angles of incidence. Angle of incidence: 45° (solid), 70° (dashed).

Another potential problem in making measurements on picosecond EM transients is false signals due to echoes[††]. From (2.46), the signal from the detector (ignoring DC level and detector response function) is,

$$\int E(x)E(x\text{-}\delta)\,dx \tag{2.57}$$

If the signal is somehow split and a fraction delayed a time d and attenuated by A, then the signal from the square law detector is

$$\int \left(E(x)+AE(x\text{-}d)\right)\left(E(x\text{-}\delta)+AE(x\text{-}d\text{-}\delta)\right)dx \tag{2.58}$$

Expanding (2.58) yields,

$$\int \left(E(x)E(x\text{-}\delta) + AE(x)E(x\text{-}d\text{-}\delta) + AE(x\text{-}d)E(x\text{-}\delta) + A^2E(x\text{-}d)E(x\text{-}d\text{-}\delta)\right)dx \tag{2.59}$$

As the interferometer arm is scanned, the first and last term in (2.59) yield the original autocorrelation signal (within a multiplicative constant) from (2.46). The second and third term are images of the autocorrelation signal attenuated by A, and delayed $\pm d$ to either side of the original autocorrelation peak. These sidelobes are spurious signals and would confuse the interpretation of the original picosecond EM transient. Therefore it is important in the design of the optical system leading from the transient source to the detector that no spurious echoes be generated.

2.4 Measurement Theory Summary

This chapter has discussed the theory underlying the generation, transmission, and measurement of picosecond EM transient as generated by relativistic electron beams. Based on this discussion, the next chapter will describe the actual hardware used to verify these theories and characterize a relativistic bunch of electrons.

[††] Note that echo and dispersion are different phenomena; whereas the FTS is insensitive to frequency dependent phase shifts on the input signal (dispersion), echo duplicates and delays a fraction of the signal. In the time domain, echo makes one pulse look like two, or in the frequency domain, modulates the spectrum by the quantity, $1 + \exp(j\omega\tau_e)$.

Chapter 3
Experimental Design

This chapter describes the overall experimental apparatus used in these investigations. The first section discusses the design of the FEL at Duke, emphasizing the design and operation of the electron beam source and the RF linear accelerator. The second section describes the electron beam sampling regions and the mm/sub-mm waveguide that carries the RF signal back to the measurement equipment. The last section describes the measurement and analysis equipment, including an estimate of measurement system performance.

3.1 FEL E-Beam Source

Although the history, design, and theory of free electron lasers is beyond the scope of this dissertation, (for excellent reviews of FELs see [Anon., 1988; Brau, 1990]) the operation of the electron beam that drives the FEL is central to this project. For this reason, the goal of this section is to describe the operation details of the FEL at Duke with particular emphasis on the electron beam system.

Two electron beam systems were evaluated in this study. The first device is the Duke Mark III FEL built by Dr. John Madey and associates over a several years [Benson, et al., 1988; Westenskow and Madey, 1984]. The Duke FEL (Mark III) produces an optical output of bunches (1-5 μs) of infrared (2-5 μm, continuously tunable) pulses (~1 pS, ~0.6-12 J peak); the electron beam system produces a 40 MeV beam of picosecond duration electron bunches. The FEL electron beam source and beam line are shown schematically in figures 3-1 and 3-2. The second electron beam source used in this work is the experimental 1 MeV picosecond electron bunch source (PEBS) developed under a joint research project between North Carolina Central

University and Duke University [Jones, et al., 1992]. In both systems, bunches arrive every 350 pS; in addition, the pulse train is chopped at 10 Hz, yielding pulse train lengths of 1-4 μS. Although this dissertation is most concerned with the electron beam before it reaches the wiggler and optics section, later, in the discussion, we will consider the electron beam after the wiggler. For now, let us concentrate on the electron beam source system.

3.1.1 RF Electronics and Electron Gun

The electron gun on the Mark III and PEBS uses a high power RF cavity to accelerate the electrons from the cathode [Westenskow and Madey, 1984]. The RF is supplied by a 25 MW klystron driven by a stable microwave synthesizer system. The klystron is pulsed with pulse lengths from 1 to 5 μS, at repetition rates of 1-10 Hz. The use of pulses prevents electrical breakdown and arcing in the FEL waveguides and LINAC. The cathode (heated to 1800 K) produces electrons via field assisted thermionic emission. The microwave fields in the cavity accelerate electrons from the cathode during the first half of the RF cycle; the same fields, during the second half RF cycle, drive emitted electrons still in the cavity back to the cathode, causing back heating of the cathode. During the full RF cycle, electrons leave the gun with a wide range of momenta (peak forward energy of ~1 MeV), with the highest energy electrons emitted early in the RF cycle, and lower energy electrons emitted later in the cycle. Electron bunches leave the gun with a period equal to the RF drive period (e.g., T=350 pS). Overall, the gun produces an average current of ~180 mA and a peak current ~20 A.

2.8565 GHz
Klystron

-7.9 dB

Variable
Phase Shifter

-56.6 dB

Alpha Magnet

Q Q D

Electron
Gun

Q

Q

Q

Key

Variable Attenuator

Q   Quadrapole Magnet

D   Dipole Magnet

Load

Waveguide Directional
     Coupler

Hybrid Coupler

Waveguide to Coax
(RG-8/U) Transition

Circulator

FEL RF Linac Schem

LINAC

Waveguide
Load

40 MeV E-Beam
To FEL
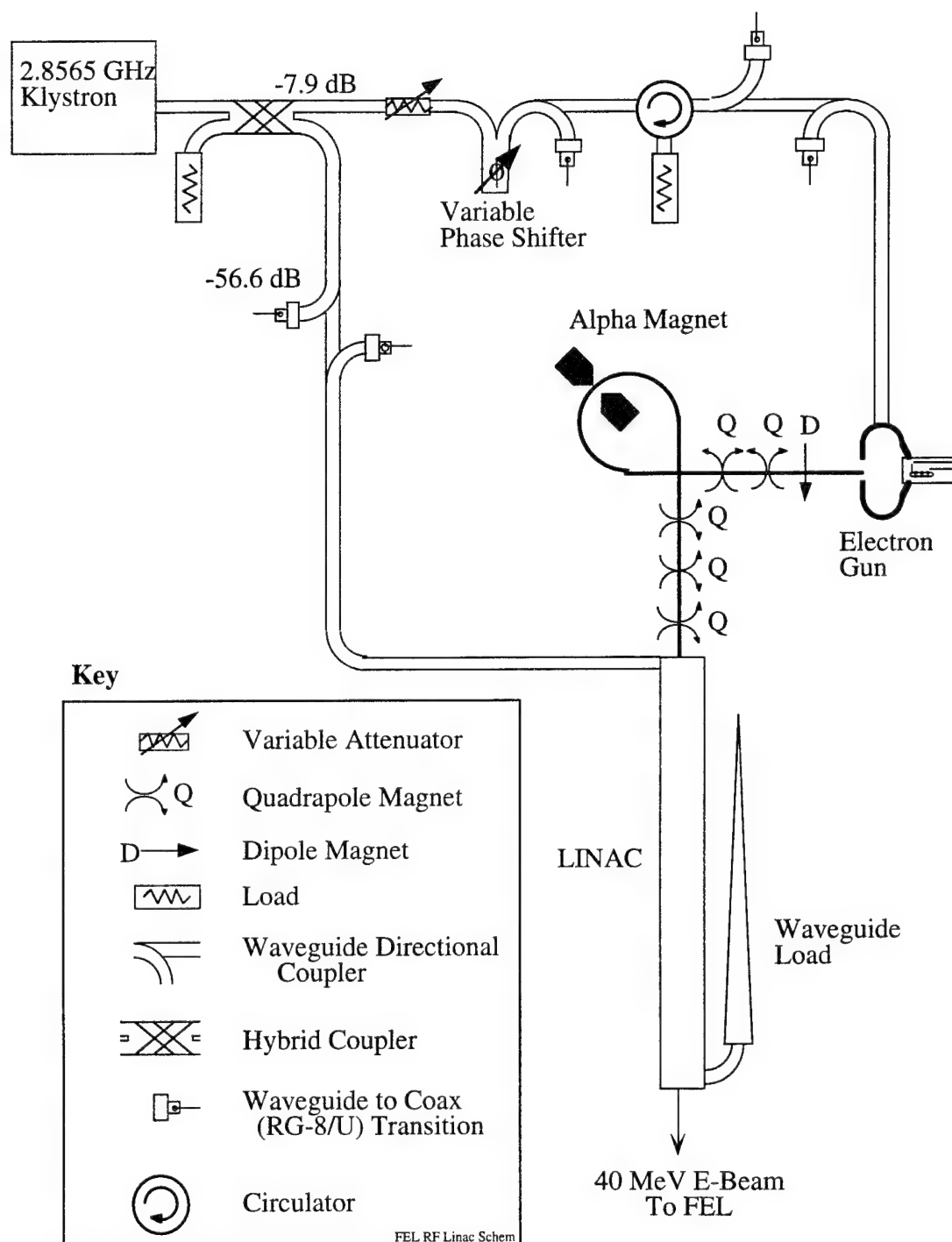
Fig. 3-1. Electron Gun and LINAC in the Duke FEL
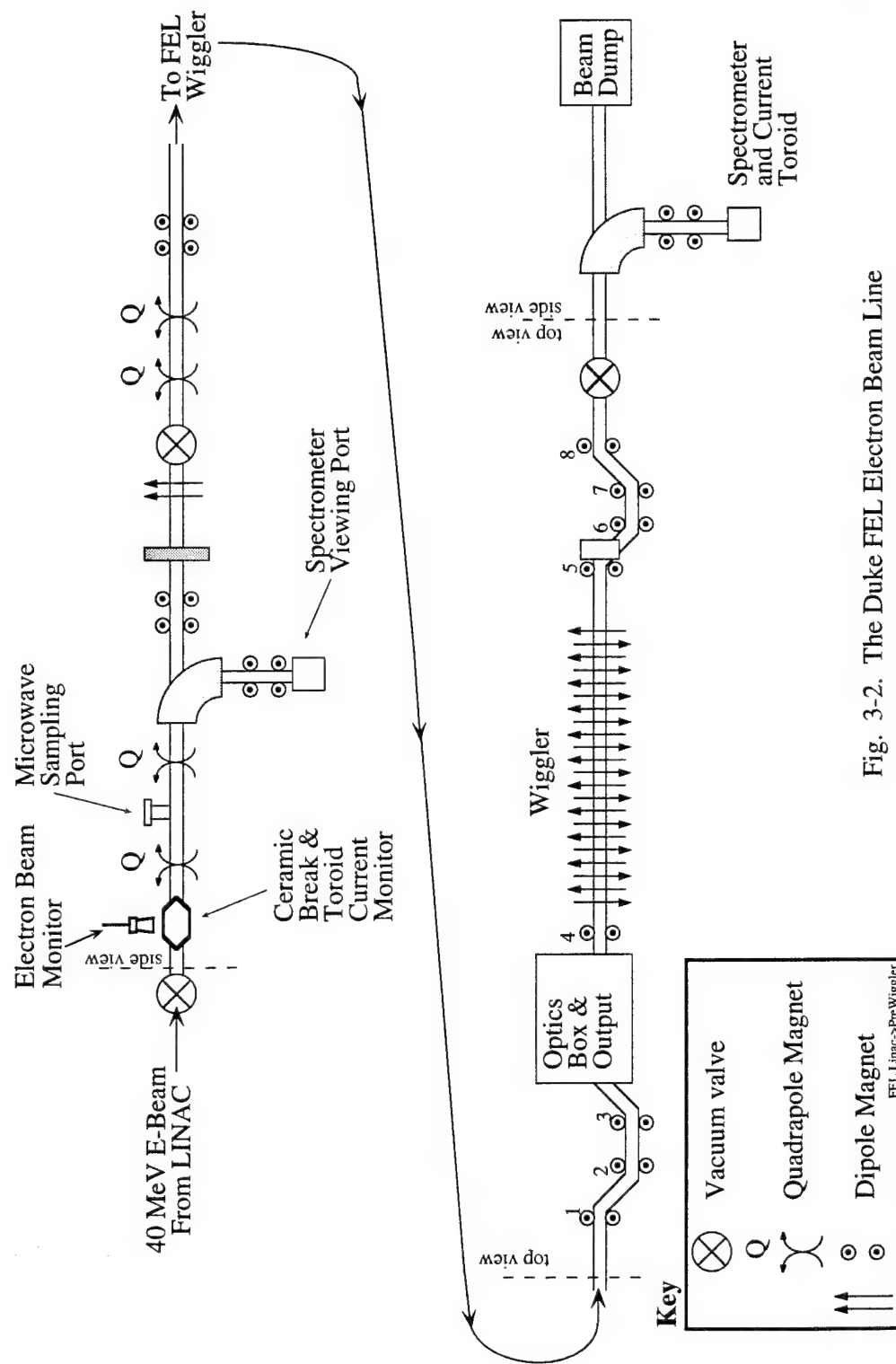
Fig. 3-2. The Duke FEL Electron Beam Line

For proper operation the FEL wiggler requires electron bunches of short time duration and small momentum spread. Because the gun produces electron bunches with wide energy spread, it is necessary to select a narrow portion of the electron beam momenta spectrum. This filtering is achieved by the alpha magnet [Enge, 1963]. Shown in figure 3-1, the electron beam enters the alpha magnet, where a linearly increasing magnetic field (directed into the page) bends the electron beam ~280° (hence the name "alpha magnet"). In this configuration, Enge [Enge, 1963] has shown that electrons with higher energy will travel larger arcs. As a result, slower, later electrons will leave the alpha magnet coincident with faster, earlier emitted electrons; the alpha magnet effectively shortens the electron beam bunches. In addition, an adjustable slit in the alpha magnet beam path allows one to select a stream of electrons with a given average momentum and energy spread. Because the RF phase during acceleration of the electrons determines the electrons' energy, the alpha magnet, by selecting electrons with a narrow range of energies, acts as a electron phase filter selecting only those electrons that have a given phase relative to the LINAC drive RF.

During the transit of an electron bunch from the gun, through the alpha magnet and to the LINAC, electrons with higher energy (emitted early in the RF cycle) will travel farther than electrons with lower energy (emitted late in the RF cycle), hence the bunch may spread. When properly adjusted, the alpha magnet will compensate for this spreading and produce a net bunch compression. The electron bunches produced by this configuration are only a few picoseconds wide.

Figure 3-3 summarizes the temporal structure of the electron beam produced by the gun and alpha magnet. At a nominal 10 Hz rate, electron bunches, called micro pulses, are emitted in groups or bunch trains, called "macro" pulses. The micro pulses are approximately 5 pS in duration and separated by 350 pS (≈1/2.8565 GHz). Macro

pulse groups are from 1 to 5 µS in duration (containing 3000 - 15000 micro pulses).
Ideally, the macro pulse is a rect() function in time.
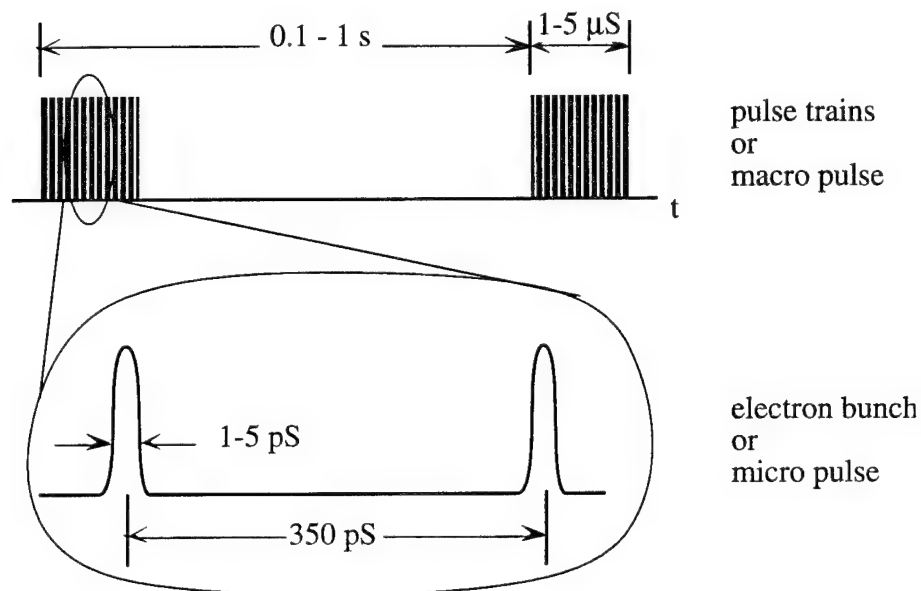
Fig. 3-3. Electron bunch and bunch train timing

3.1.2 Linear Accelerator (LINAC)

To be useful as a gain media in the wiggler section of the FEL, the electron
bunches must be accelerated to near the speed of light. The reason for this is that the
wavelength of the optical output from the FEL is approximated by [Brau, 1990, eq. 1.4,
pp. 7-14],

$$\lambda_L = \lambda_W / 2\gamma^2 \qquad (3.1)$$

where λ_L is the wavelength of the FEL optical output, λ_W is the distance between like
wiggler magnet poles (figure 3-2), and γ is the relativistic energy parameter,

$$\gamma = (1 - \beta^2)^{-1/2} \qquad (3.2)$$

$$\beta = v/c \qquad (3.3)$$

where v is the electron velocity and c is the speed of light. Therefore higher electron energies yield shorter optical wavelengths.

The LINAC used in the Duke FEL is based on the disk loaded waveguide [Brau, 1990, chapter 8]. Traveling waves are coupled into the entrance and propagate, along with the electron bunches, down the waveguide. When properly designed the disk loaded waveguide supports near TM_{010} modes. In each waveguide section, the phase velocity of the injected RF couples energy into the electron beam; beam energy increases with each section, hence increasing the number of disk loaded sections, linearly increases the beam energy. The LINAC on the Duke FEL produces electron beam energies of up to 45 MeV.

TM_{010} $\qquad$ TM_{110}

(a)

(b) $\qquad\qquad\qquad\qquad\qquad\qquad$ (c)
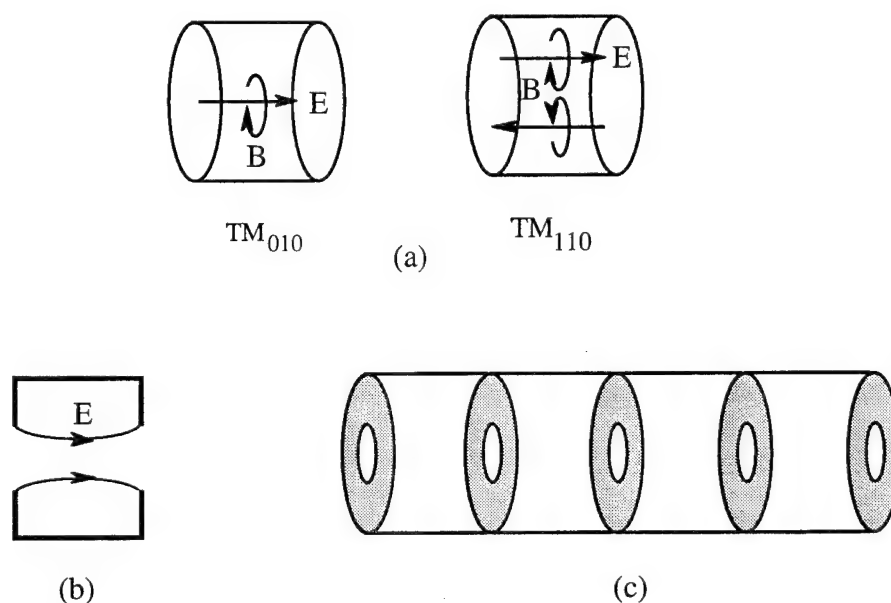
Fig. 3-4. LINAC Cavity Design. a) TM_{nmo} modes supported by cylindrical cavity. b) Section of disk loaded cavity showing axial E-field. c) Disk loaded waveguide segment.

3.1.3 Electron Beam Controls and Monitors

Various quadrapole and dipole electro-magnets bend and focus the electron beam, much like prisms and lenses steer and focus optical beams. To monitor the beam

position and transverse profile, the FEL operators can move fluorescent viewing screens into the beam path and watch the impact image of the electron beam via TV cameras. In addition to the viewing screens, the operators monitor the beam energy with two spectrometers (before and after the wiggler), and the beam current is monitored by a toroid coil immediately after the LINAC. The PEBS system currently has no energy spectrometer, and uses only a toroid and Faraday cup to measure electron beam characteristics. Finally, pyro-electric detectors monitor the optical output from the FEL (many experiments simply need maximum optical power without concern of electron beam efficiency or operation).

In the current FEL configuration there is no means of monitoring either directly or indirectly the electron pulse structure. As discussed in the Introduction, other researchers [Bergere, et al., 1962; Neal, 1968, pp. 264-6] have developed simple devices for monitoring electron bunch length, however none of these have been adopted in the current Mark III or PEBS design.

Note that it is possible to get the electron beam positioned correctly, yet have the direction and divergence incorrectly adjusted.[‡‡] Also it is possible to have large electron beam currents, yet have the electron beam incorrectly aligned (direction, focus, and energy), yielding poor FEL operation (i.e., toroid and pyro do not indicate electron beam micro pulse structure).[‡] In other words, both the electron beam geometry and temporal characteristics must be properly adjusted for optimum FEL operation.

Finally, the high energy electron beam can become a source of x-ray radiation and high energy particles if it hits the metal beam tube or any other metal object. This can occur when the beam is being steered (during FEL alignment) or when the beam is

---

[‡‡] The optical system analogy is when an laser beam passes through the center of a lens, but because of lens tilt, exits at an angle off axis; if the beam must travel through a series of lenses, tilts and focal length misadjustment will yield grossly distorted output beam.

[‡] A similar situation occurs in the alignment of femtosecond optical lasers: maximum average optical power often is not commensurate with minimum pulse width.

routed into either energy spectrometer. In addition, x-rays are emitted when the electron beam hits the beam dump at the end of the FEL. Components hit by the electron beam become neutron activated, and remain radioactive for as long as several hours. For these reasons, the entire electron beam system (gun to beam dump) is housed in a shielded room with no access permitted during operation (and for a few hours after operation). Radiation levels in the FEL room during operation go as high as 100 rem/hour; fatal to biological organisms and destructive to some electronics and optics.

3.1.4 Electron Beam RF Source Points

Although most of the Mark III electron beam path is enclosed in metal pipe (effectively containing any RF produced by the electron beam), there are currently two locations along the beam line at which the beam is exposed. The first location is an electrical "break" in the electron beam pipe formed by a short ceramic tube, just beyond the LINAC. Originally designed as a location for a toroid beam current monitor, this "ceramic break" (figure 3-5) makes a usable window for observing the RF emitted by the electron beam. The second location is a special Tee placed in the beam line. Located just beyond the ceramic break and between two quadrapole magnets, this tee couples electron beam RF through a reduced height waveguide and a glass (quartz) window. To prevent charge build up (a problem in high energy electron beam systems) the window is coated with 40 Å of chromium. The metalization was found to have negligible effect in the mm/sub-mm range.
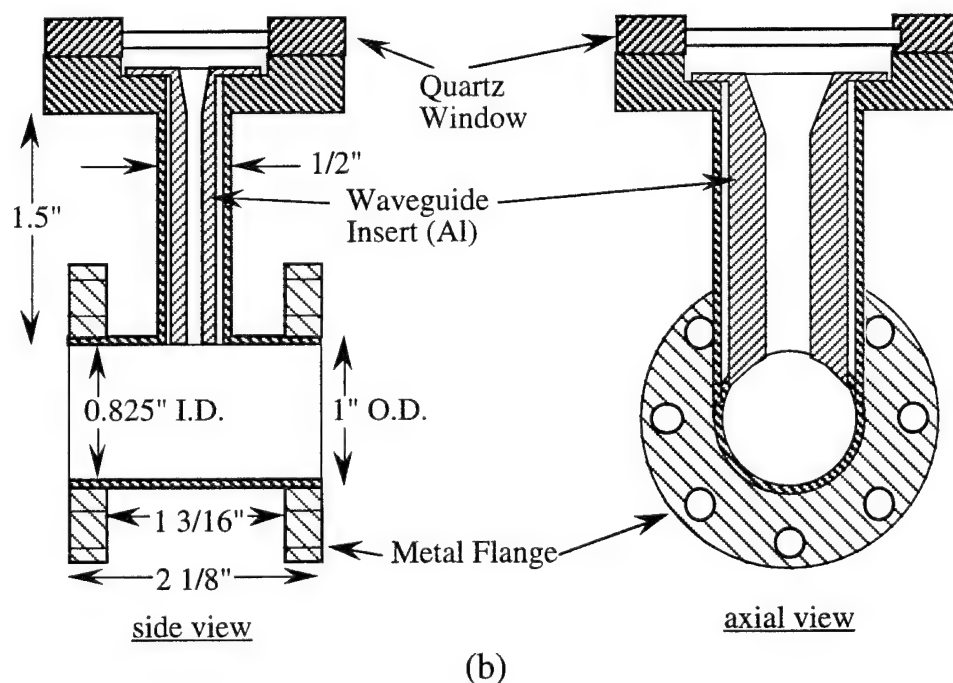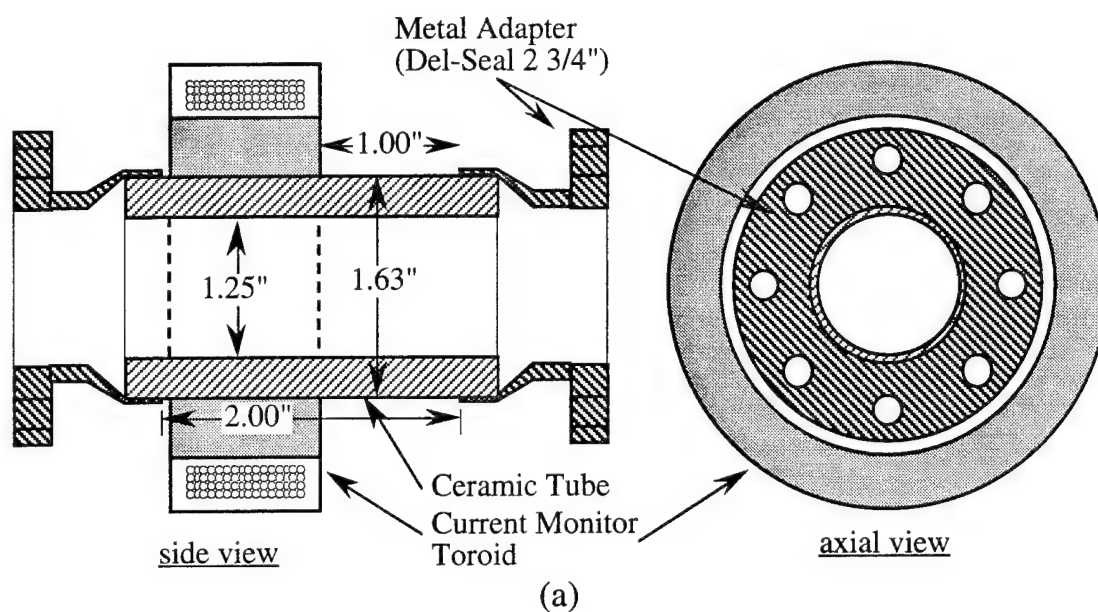
Fig. 3-5. Ceramic Break and Beam Line Tee details. (a) Ceramic (alumina) break showing relative position of current monitor toroid, and open space for RF pickup. (b) Tee placed in beam line with waveguide RF coupling structure (waveguide insert detail shown in figure 3-6).

In the PEBS the electron beam was passed through a rectangular waveguide. Initially, two sizes of waveguide were used. The large waveguide was 1.9 mm x 3.8 mm, with a 1 mm diameter hole in the center of the wide wall for the electron beam passage. The small waveguide was 0.95 mm x 1.9 mm, with a 0.5 mm diameter hole in the center of the wide wall. Both guides were about 15 cm long, from the electron beam hole to the end of the guide. The signal from the guide diffracted out of the end of the guide, passed through a quartz vacuum window, and aimed into overmoded transport guide.

3.2 RF Sampling and Transport

Due to the high radiation environment of the operating FEL, it is not possible to have measurement equipment near the RF ports at the ceramic break or the beam line tee. Therefore the RF generated by the electron beam must be coupled out of the beam line and transported to the measurement system in an adjacent lab.

3.2.1 Electron Beam RF Coupling Structures

As described in §3.1.4, there are two areas at which the electron beam RF can be sampled. When monitoring emission from the ceramic break, the open end of the circular transport waveguide sampled the RF of the electron beam. A variety of distances between the open waveguide end and the ceramic break have been tried. In all cases the waveguide axis was perpendicular to the electron beam transit. In some cases, an Eccosorb[†] barrel was extended beyond the end of the waveguide to reduce higher order transverse mode coupling.

The beam monitor at the tee is somewhat more complex, using a reduced height waveguide section to couple RF from the beam line to the transport waveguide.

[†] Eccosorb is a layered dielectric microwave absorbing material originally manufactured by Emerson-Cummings, however it is now available from a variety of sources. The material used in these experiments was AN-72, a quarter inch thick, yielding 20 dB attenuation at 10 GHz; attenuation increases at higher frequencies making this an ideal mm/sub-mm attenuating material.

Because the entire tee is under vacuum, it has not been practical to experiment with different coupling geometries. Currently a rectangular waveguide section acts as a simple field probe (figure 3-6). The TE_{0n} cutoff frequency for dimensions given is 39.4•n GHz. To improve the coupling between the sampling section and the transport waveguide, the sampling waveguide output is flared to form an 18° full angle pyramidal horn.
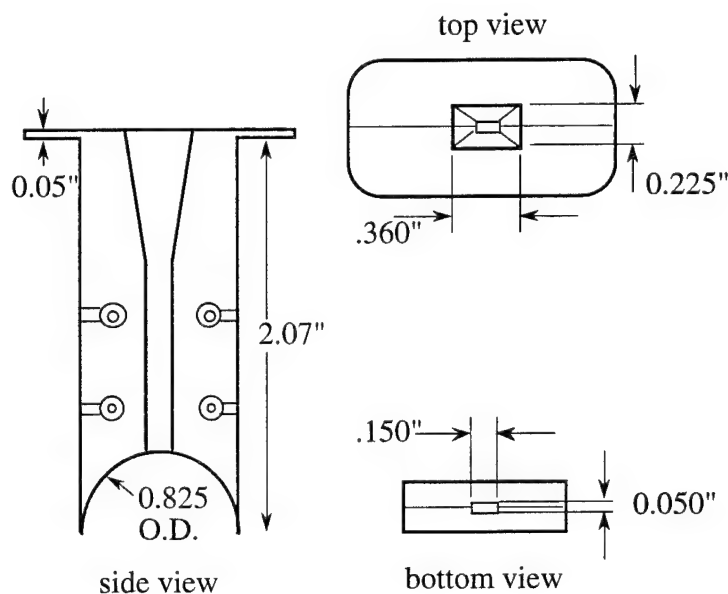
Fig. 3-6. Electron beam sampling waveguide insert. The waveguide end that samples the electron beam is simple reduced height rectangular waveguide. The output end is flared in both axes to form an 18° full angle horn.

3.2.2 Waveguide System

Circular waveguide was used to transport the electron beam RF from the coupling devices to the measurement electronics. Circular waveguide was chosen for two reasons. First, circular waveguide is widely used in the mm/sub-mm spectroscopy community; in particular, the Microwave Groups at Duke and The Ohio State University (OSU) have used this form of guide for over 40 years in studies involving gas phase spectroscopy in long (>10 m) cells. In the mm/sub-mm regions, circular

waveguide has extremely low attenuation per unit length. Circular waveguide is also easily constructed from commercially available copper water pipe. Simple brass coupling rings are soldered to the ends of the pipe, allowing "Tinkertoy"-like construction of large waveguide systems. Bends in the waveguide are accomplished using right angle guides specially constructed by the Microwave Group at OSU.

The waveguide system constructed as shown in figure 3-7. Currently no mode filters are used in the waveguide, however, for some experiments Eccosorb tubes were extended from the waveguide to the coupling structure (either the Tee window or the ceramic break). When monitoring the ceramic break, the waveguide was brought within 3 cm of the outside of the ceramic and later 25.4 cm from the ceramic. When monitoring the Tee output, the waveguide was brought to 2.5 cm from the window.
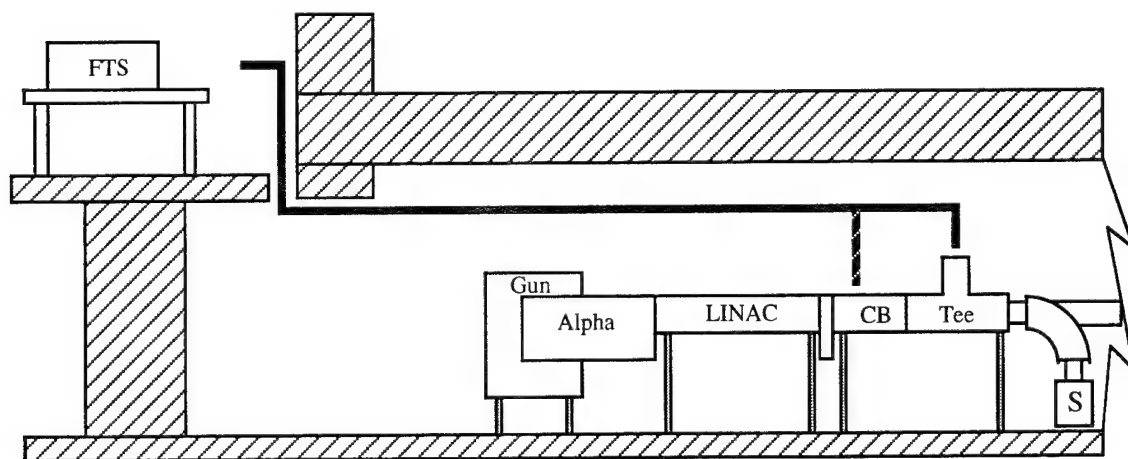
Fig. 3-7. Schematic of waveguide layout from measurement instrumentation to electron beam couplers. CB is ceramic break, S is electron spectrometer. Figure is not drawn to scale, however the LINAC is ≈ 2 m long, and the length of the transport waveguide from the Tee to the FTS is ≈ 17 m.

3.3 Detection and Measurement Systems

The various instruments used to monitor the electron beam RF form the core of the experimental system. Initially, horn mounted diode detectors were used to verify the

predicted RF. Later, both microwave spectrum analyzers (heterodyne detection) and Fourier transform spectrometers were used. The experimental implementation of these instruments is described in this section.

3.3.1 Fourier Transform Spectrometer

The Fourier transform spectrometer (FTS) used in these experiments was constructed entirely from scratch. There were three reasons for the do-it-yourself approach: cost, time, and flexibility. First, it was most economical; most of the parts for the FTS were available in the Duke Microwave lab or could be borrowed from other groups. Overall equipment costs were under US$1000. Second, this approach was most expeditious; the entire spectrometer was build, tested, re-engineered, re-tested and running in four months. An additional month was required for design and construction of the helium cooled InSb detector. Third, by constructing all the apparatus ourselves we were able to tailor the measurement system to the source characteristics.

The spectrometer is of conventional design [Bell, 1972]. The layout of the FTS system is shown in figure 3-8. Table 3-1 itemizes the various FTS components.

The translation stage had 30 cm total travel, however for most of the scans shorter displacements were used. Over the entire range of mirror displacement the stage produced less than 0.5 mrad angular error; the largest error occurred at the ends of the stage, so most scans were restricted to the center portion of the stage where angular error was less than 0.1 mrad. The mechanical operation of the drive screw was calibrated against a precision machinists dial (accuracy ~0.1% of full scale displacement of 1") and found to have negligible backlash, linear monotonic motion, and a position accuracy of < 0.4% total displacement .

The stepper motor was connected directly to the displacement drive screw. The average displacement for a single step was measured to be 4.99 μm. Although the motor had a rated maximum speed of 500 steps/second, due to control (computer

software) limitations, maximum step rate was limited to 100 steps/second. Due to other bottlenecks in the data collection system (DSO limits described below), this reduced rate was not a limiting factor. The entire stepper motor system was constructed for ~US$120.

Mylar was chosen as the beamsplitter material for two reasons. First, the optical properties of mylar are almost ideal for mm/sub-mm applications; mylar has an index of 1.69 and very low loss (negligible for the thicknesses used here). The second advantage of using mylar is that it available in a variety of thicknesses at reasonable cost. Finally, because mylar is transparent in the visible (unlike teflon or polyethylene), optical alignment can be done using a HeNe laser.

The mirrors used in the FTS are front surface aluminum coated, and although their surface flatness is marginal ($3\lambda/25$ mm) for visible light interferometry, the equivalent flatness at 300 GHz is $\lambda/150$ across the entire 10 cm diameter surface which is quite acceptable for interferometric measurements. Because the mirrors were relatively thin, large area (10 cm sq.) mirror mounts are used. These mounts provide excellent adjustment, support, and stiffness. Although the mirror mounts were custom ordered from ThorLabs, they were much less expensive than comparable stock items available from other vendors.

Table 3-1. Summary of FTS components.

Item	Description	Manufacturer
M,M1, M2	10 cm dia., 3 mm thick, 3λ @ 633 nm / 25 mm, front surface aluminum mirror (BK7)	Melles Griot 01 MFG 030
M1,M2	Adjustable Mirror Mount, 10 cm optic	ThorLabs, MM4
T	Linear translator stage and rail, mm/rotation drive screw	Velmex
S	Stepper Motor, 200 step/rotation	C&H Sales
BS	Beam splitter holder, aluminum, 10 cm clear aperture	OSU
BS	Beam splitter, mylar, 250 μm or 50 μm	
H	Microwave horn, Conical	
D	Detector, helium cooled InSb bolometer (see §3.3.2 for design details)	
SMC	Stepper motor interface	Forthright Electronics, or, C&H Sales
LIA	Lockin amplifier	Stanford Research Systems, 510
DSO	Digitizing oscilloscope	Hewlett Packard 54504
L	microwave lenses, TPX or teflon	
AL	alignment laser, HeNe	
m	alignment mirrors, front surface, $\lambda/4$	

Table 3-2. Component Manufacturer Information.

Manufacturer	Address	Phone
Velmex	P.O. Box 38, 7550 Routes 5&20, E. Bloomfield, NY 14443	800-642-6446
C&H Sales	2176 East Colorado Blvd., Pasadena, CA 91107	800-325-9465
Forthright Electronics	2851 Mendicino Drive, Unit A, Prescott Valley, AZ 86314	602-772-0288

(top view)

(Front Elevation)
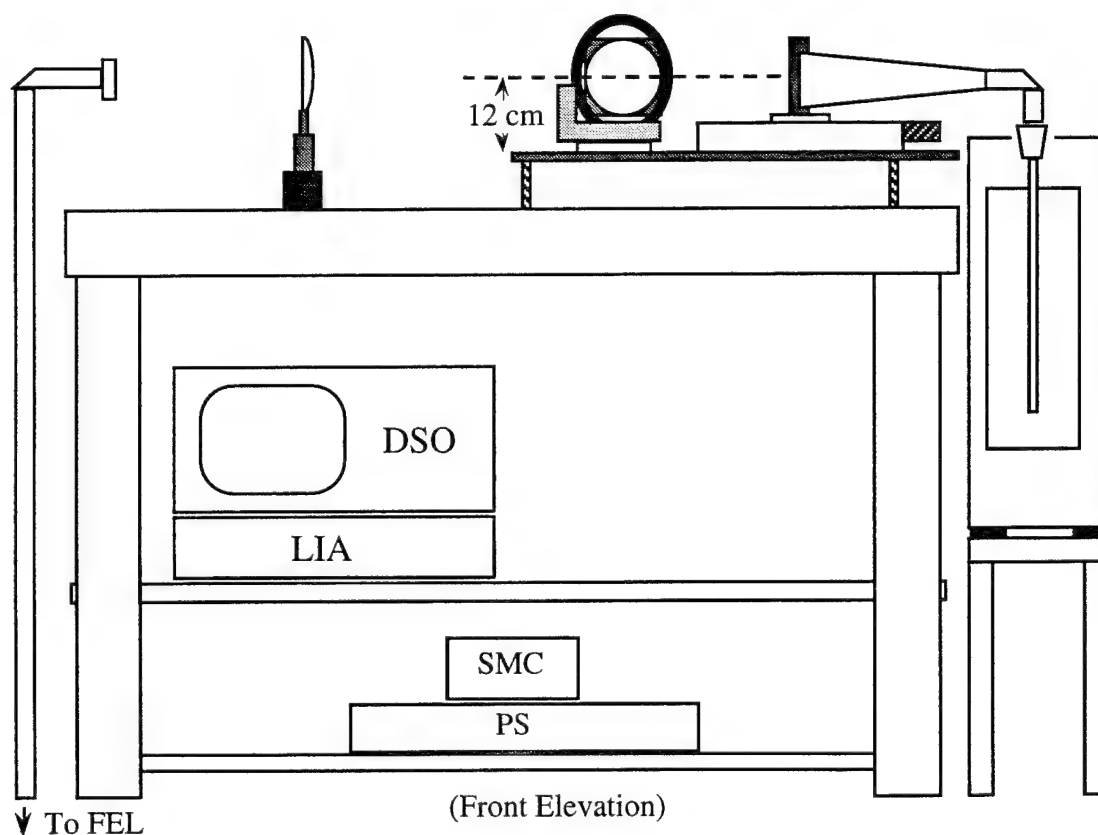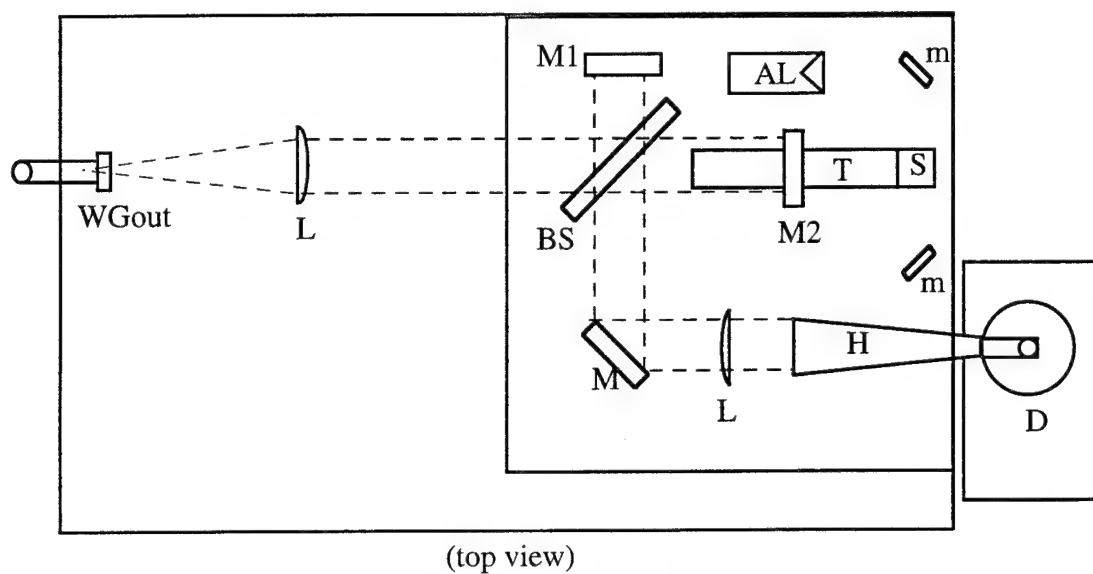
Fig. 3-8. FTS layout and instrumentation setup. Top view shows layout of FTS components: WGout, FEL waveguide output; L, microwave lens; BS, beamsplitter; M,M1 fixed 10 cm dia. mirrors; M2, moving 10 cm dia mirror; AL, alignment laser; m, alignment mirrors; H, horn; D, detector and dewar. Front elevation shows location of electronics: DSO, digitizing oscilloscope; LIA, lockin amplifier; PS, stepper motor power supply; SMC, stepper motor controller.

3.3.2 Helium Cooled InSb Hot Electron Bolometer

The InSb detector and helium dewar were specially constructed for this project. A helium cooled InSb hot electron bolometer was used because of its excellent sensitivity (typically NEP $\sim 10^{-12}$ W/Hz$^{-1/2}$), broad spectral range (typically flat from dc-300 GHz, $1/f^2$ rolloff beyond 300 GHz), and fast response time (<1 μS). No other mm/sub-mm detector has these characteristics.

Figure 3-9 shows the design of the detector and light pipe system. The dewar was a stainless steel double jacket cryostat originally manufactured by Raytheon for airborne far-IR studies. The dewar is compact (16" tall, ~5" dia.) and portable (a necessary requirement because the liquid helium supply was located in the Physics building, while the actual experiment apparatus was located on the roof of the FEL entrance labyrinth).

The dewar vacuum was typically rough pumped to below 30 mTorr. The dewar could be chilled in under two hours and required approximately two liters of liquid nitrogen and one liter of liquid helium. On a single nitrogen fill, the dewar liquid helium hold time was nominally 18 hours with the detector inserted. If the detector assembly was removed and the nitrogen topped off, the liquid helium hold time was over 24 hours.
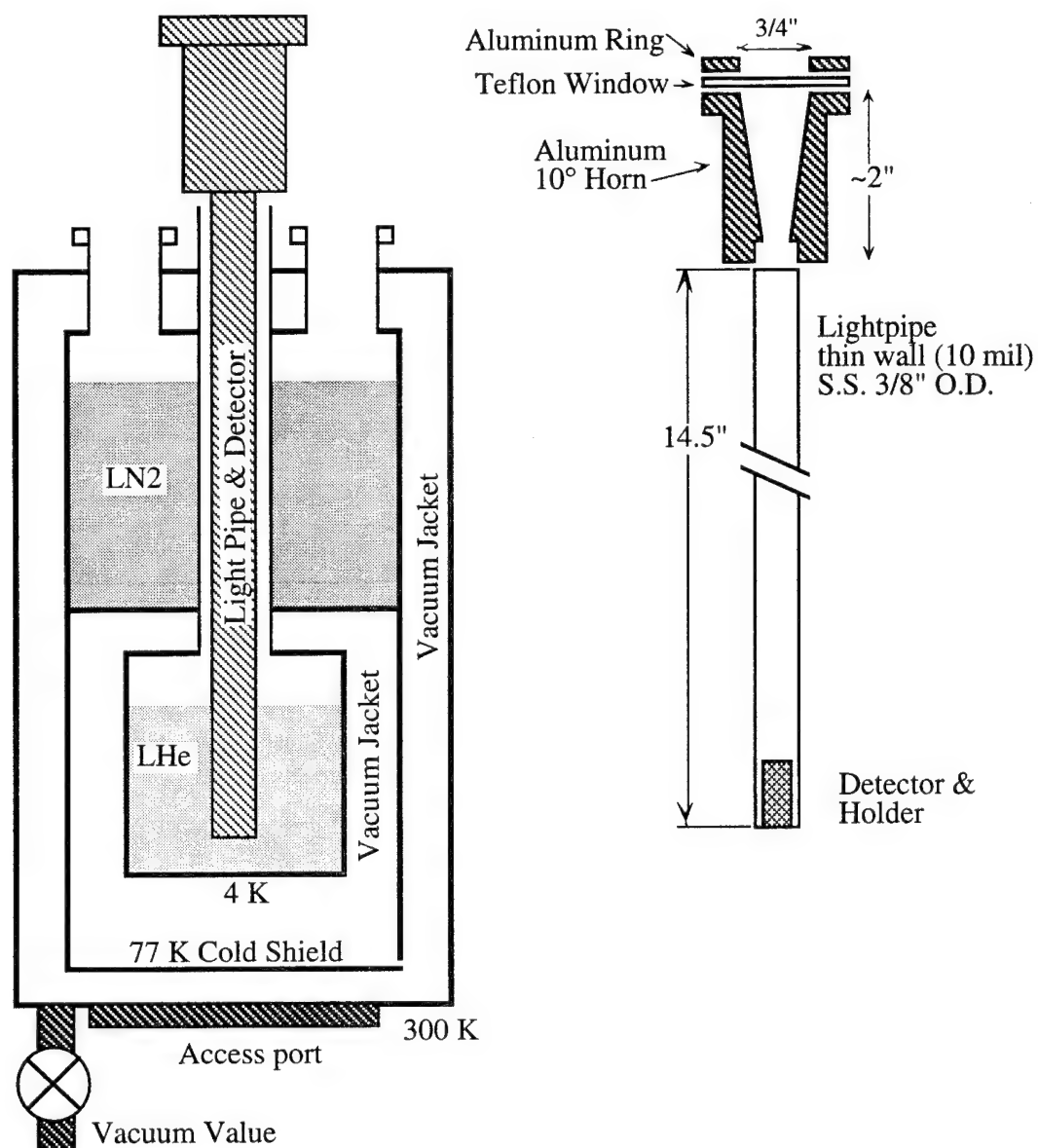
Fig. 3-9. Detector and cryogenic dewar. See figure 3-10 for a detailed view of the detector and holder.

Several different detector designs were tried, however the most functional used a simple stainless steel light pipe to carry RF to the InSb detector submersed in the liquid helium bath. In this design, a 10° conical condensing horn [Williamson, 1952] collects the signal from the interferometer into the top of the light pipe. The signal then bounces down the light pipe, finally hitting the detector section. The detector section (shown in figure 3-10) is submerged in liquid helium. The signal is again concentrated by a smaller 10° horn, then filtered by a 4 mil black polyethylene (low pass) filter at 4 K. The passed radiation hits the InSb chip where it is partially absorbed (yielding a detectable change in conductivity). Finally, an eccosorb plug absorbs any radiation transmitted beyond the detector. The electrical signal from the InSb chip is carried on a pair of #38 enameled wires; the wires are varnished into a groove over the top and side of the detector holder, come onto the outer surface of the light pipe and spiral up the light pipe to a coaxial connection at the top of the detector assembly. Micro-coax and twisted pair transmission line geometries were also tried, however they gave no better electrical results and were more complicated to construct. The detector horn fit tightly (at room temperature) in the light pipe, the polyethylene filter was pressed between the horn and holder, and the entire mount was held in the lightpipe by masking tape*.

---

* Dr. J. Holton conducted numerous studies on the mechanical properties of various bonding agents, and found that masking tape is the only one to remain adhesive over repeated thermal (4 K) cycling.[Holton, 1993]
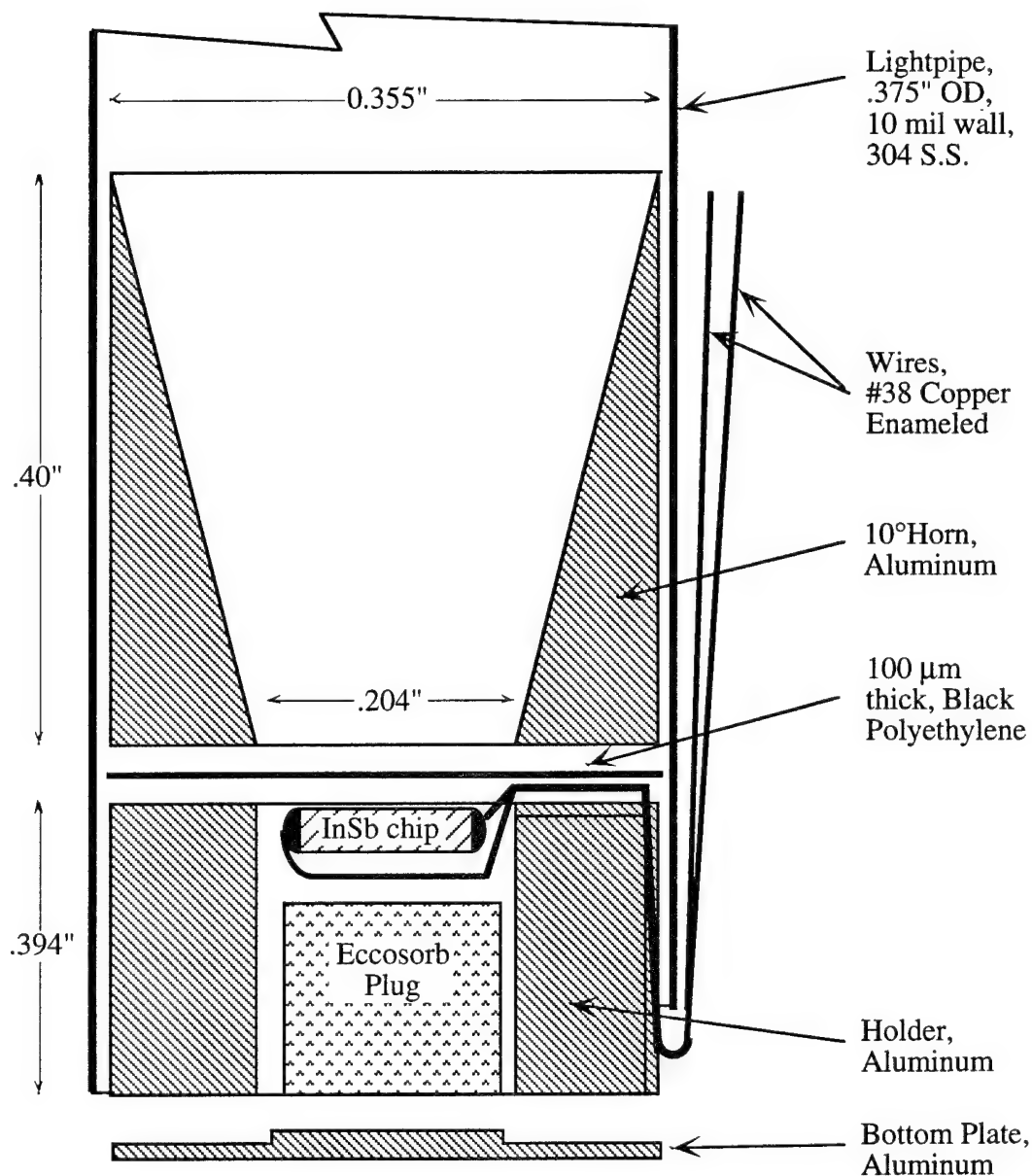
Fig. 3-10. Detail of InSb detector mount.

The InSb chip used in these experiments was obtained from the OSU Microwave Group[††]. The sample characteristics are shown in Table 3-3. The #38 enameled wires were soldered to either end of the chip using Indalloy solder #1E[**] and Harris "Stay

---

[††] The samples were graciously provided and initially processed by D. Flatin and Dr. F. De Lucia.
[**] Indium Corporation of America, 1676 Lincoln Ave, Utica, New York

Clean" flux. When biased by 100 μA at 4°K, the chip initially yielded a 15.9 mV drop; over the period of 2 months this value drooped to 14.6 mV.

Table 3-3. InSb Chip Characteristics.

InSb chip	#1
Manufacturer	Johnson-Matthey (Cominco America Inc., Electronic Mat. Div.), E. 15128 Euclid, Spokane WA 99216, ph. 509-924-2200 PO: HX-380736-A, Contr. EMS 27320 Date: 26 June 1980 Lot: W-4176-I, grade 56
Doping	n-type, N=3-4.8 x 10^{13} cm^{-3} @ 77 K
Mobility	5.8x10^5 cm^2 V^{-1} s^{-1} @ 77 K
Resistivity	≈0.3 Ω cm @ 77 K
Dimensions	≈ 1.5 mm x 0.8 mm x 2.5 mm

3.3.3 FTS and Detector Performance Estimates

Based on the description of the FTS and detector in the last section, it is possible to estimate the spectral and temporal response of the spectrometer. Although the spectrometer is calibrated before use, it is useful to determine a likely range of measurement system operation as an operational guide.

First consider the spectral range of the FTS. The FTS used in this work measures very broadband spectra. Ideally, the components used in the spectrometer should all have very low loss, or at least constant loss independent of frequency. Unfortunately, real components and materials have non-negligible loss that is frequency dependent. The product of all components' transmission yields the total loss at any frequency. Table 3-4 gives an estimate of the frequency dependent transmission both for individual components and for the complete system.

Table 3-4. Transmission estimates of FTS components.

Transmission	10 cm⁻¹ (300 GHz)	20 cm⁻¹ (600 GHz)	30 cm⁻¹ (900 GHz)	40 cm⁻¹ (1.2 THz)	50 cm⁻¹ (1.5 THz)	100 cm⁻¹ (3 THz)
TPX Optics, 2 cm	.87-.76	.67-.45	.54-.30	.44-.20	.40-.14	.004
Teflon, 2 mm	.98	.95	.92-.90	.86-.76	.81-.72	.86-.67
Blk. Poly., 100 μm	.97	.95	.92	.88	.84	.13
Light Pipe, 35 cm, 72 μΩ	.81	.76	.72	.69	.67	.60
System Total	.67-.59	.46-.31	.34-.17	.23-.09	.18-.06	$\approx 3 \times 10^{-4}$

Because different researchers have used different grades of TPX [Chantry, et al., 1969; Chantry, et al., 1971], there is a wide range in the expected transmission spectra of the TPX optics. For Teflon, the expected transmission is effected by both structural variations, formulae variations, and temperature variations [Alvarez, et al., 1975; Chantry, et al., 1972; Johnson and Rabolt, 1973]; in particular, teflon undergoes a phase transition at 19°C, resulting in strong temperature dependent absorption in the 40 to 50 cm⁻¹ region. Like TPX, black polyethylene has a range of transmission spectra, depending on manufacturer [Bell, 1972; Blea, et al., 1970] . Finally, the light pipe in the detector dewar has a frequency dependent transmission due to wall losses [Ohlmann, et al., 1958].

The total transmission results of Table 3-4 are illustrated in figure 3-11. Also shown are a variety of rolloff functions, that may reasonably approximate the measured system response. In operation, the frequency dependent response of the FTS will be calibrated against a blackbody source.
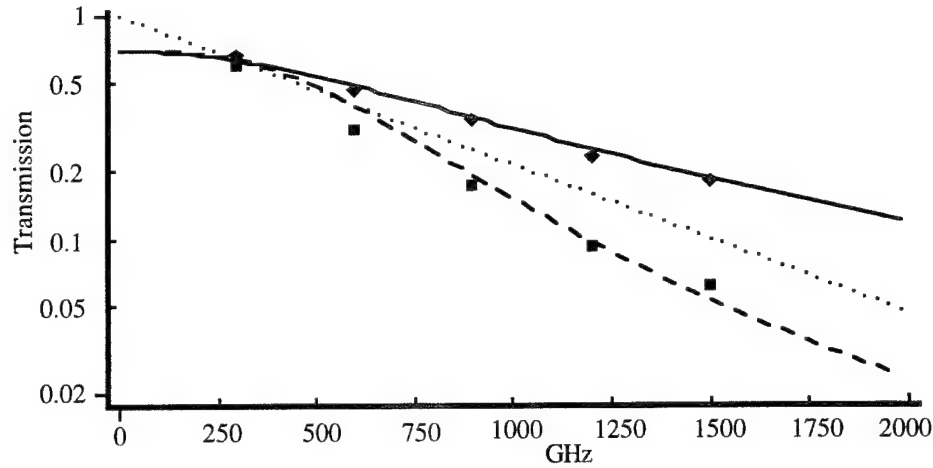
Fig. 3-11. Graph of estimated transmission of FTS system. Diamonds and squares are maximum and minimum transmission estimated in Table 3-4. Lines are different rolloff functions: solid, $0.7 (1 + (f/900)^2)^{-1}$; dotted, $\exp(-f/650)$; dashed, $0.7 (1 + (f/650)^3)^{-1}$.

Like the FTS components, the InSb detector also has a frequency dependent spectral response. Although the theory of helium cooled hot electron bolometers is beyond the scope of this research, it is useful to estimate the spectral response of the InSb detector. The response of an InSb detector has been shown to be proportional to the frequency dependent material conductivity [Kogan, 1963; Putley, 1964; Putley, 1977],

$$R_{InSb} \propto \sigma(\omega) = \sigma_0 (1 + \omega^2 \tau_{es}^2)^{-1} \tag{3.4}$$

where τ_{es} is the electron scattering time, and the dc conductivity, σ_0, is expressed in terms of carrier concentration, N, and the effective mass, m^* ($= 0.014\, m_e$ for InSb),

$$\sigma_0 = Nq^2 \tau_{es}/m^* \tag{3.5}$$

Measuring the resistivity, ρ, of the InSb sample at 4 K, (3.5) yields the electron scattering time,

$$\tau_{es} = m^*/ Nq^2 \rho \tag{3.6}$$

Defining a linear frequency rolloff parameter, $f_o = 1/(2\pi \tau_{es})$ and rewriting (3.4) in terms of linear frequency, yields the detector spectral rolloff versus linear frequency of incident microwave radiation,

$$R_{InSb} \propto \sigma(f) = \sigma_o(\ 1 + (f/f_o)^2\ )^{-1} \tag{3.7}$$

Hence, for microwave radiation with $f \ll f_o$, the InSb detector response is relatively flat; for radiation with $f \gg f_o$, the detector response falls off as f^{-2}. For the sample used in this work (see Table 3-3), $\tau_{es} \approx 200$ fS, and $f_o \approx 800$ GHz.

Finally, others [Putley, 1964; Rollin, 1961] have shown the electrical bandwidth of the InSb detector is inversely related to the carrier lifetime. For InSb detectors similar to the one used in this work the carrier lifetime is on the order of 200 nS, yielding an estimated electrical (video) bandwidth ≈ 2 MHz.

3.3.4 Electron Beam Monitor

As discussed in the next section, a trigger signal is needed to synchronize the sampling hardware to the beginning of the electron pulse train. The synchronizing signal comes from an X-band waveguide to coax detector mount which, located at the ceramic break (figure 3-12), acts like a receiver and detects the RF field associated with the passing electron pulse train. The detector mount holds a 1N23 crystal detector and drives 75 feet (22.9 m) of 50 ohm (RG-58/U) coax without amplification. Because the detector mount has a video bandwidth of >10 MHz, the signal sent down the coax has the same time structure as the signal generated by the FEL toroid beam monitor.

ceramic break

waveguide
detector mount

RG-58/U Coax
to Instrumentation

(transverse plane)   (parallel plane)
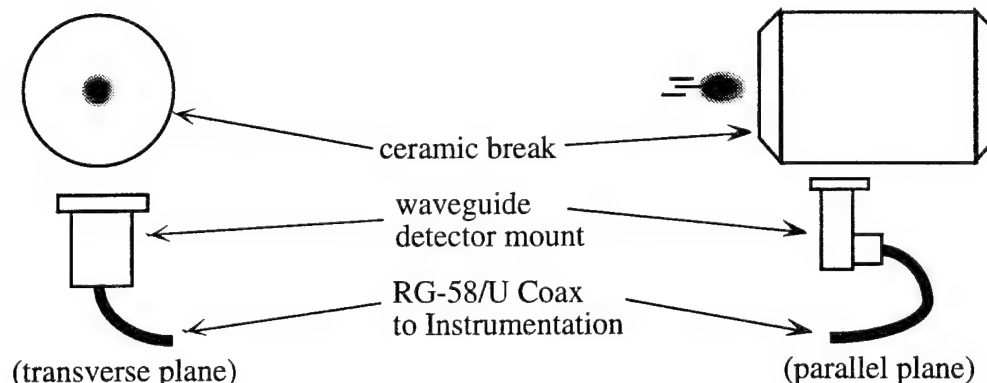
Fig. 3-12. Beam monitor layout.

The waveguide beam monitor does have some directionality, and as a result, also acts as a coarse beam position monitor. Therefore the signal produced by the waveguide mount is a function of both the average electron beam current and the beam position.

3.3.5 Sampling, Control, and Analysis Electronics

Figure 3-13 shows a schematic of the FTS control and analysis system. The overall control is provided by an Apple Macintosh IIci computer, utilizing both a National Instruments GPIB controller and a multi-function interface board. National Instruments' Labview software controlled all aspects of runtime operation and data collection. Because the FEL macro pulses are 1-5 μS in duration, much faster than available sampling boards, an HP 54504 digitizing oscilloscope (DSO) samples the FTS signal and also the signal from the FEL electron beam monitor (see next section).

Special care has been exercised in shielding the signal from the InSb detector to the sampling electronics. The reason for this care is that the millivolt level signal from the InSb detector could easily be lost in the noise produced by the 25 MW FEL pulsed klystron, located within two meters of the experiment. The detector signal was amplified immediately outside the dewar, and entire dewar, detector and preamplifier assembly were placed in a copper Faraday can, with a single opening in the top for the

FTS microwave signal. The amplifier typically used was an Ortec 5004 with 60 dB

(x1000 voltage) gain and 1 MHz bandwidth. Occasionally, a homemade x100 voltage

amplifier (based on the Analog Devices AD844) with 8 MHz bandwidth, was used.

Both amplifier were powered by battery packs, also placed inside the Faraday cage.

Single shielded coaxial cable (RG-58) brought the signal from the detector system to

the DSO.
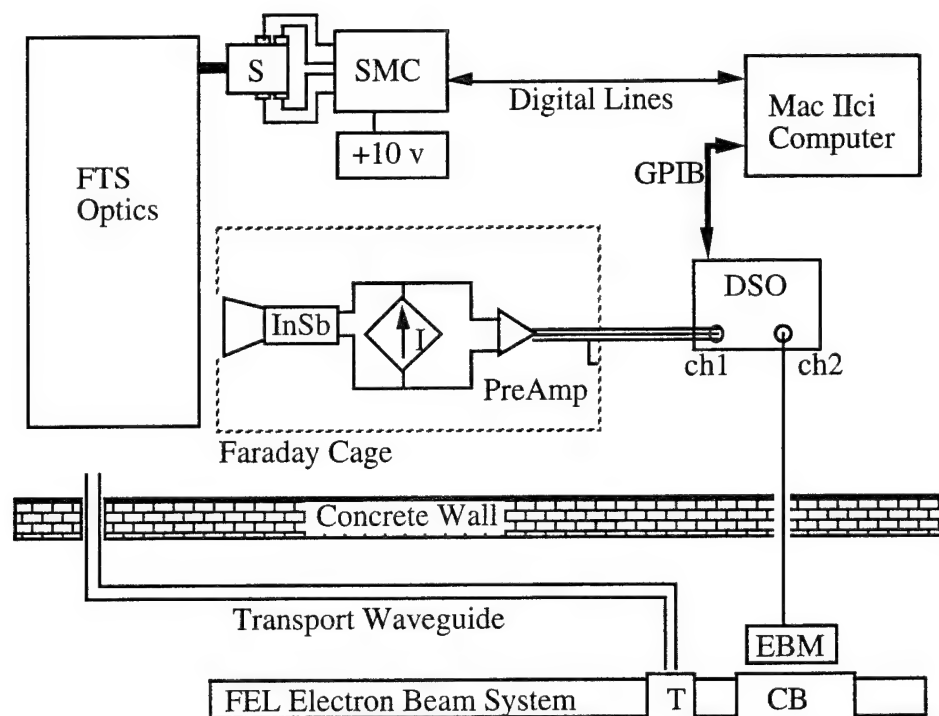
Fig. 3-13. Measurement system instrumentation schematic. InSb, InSb
detector; I, detector bias supply; EBM, electron beam monitor; S, stepper
motor; SMC, motor controller and power interface; DSO, digital
sampling oscilloscope; CB, ceramic break; T, pickup tee.

The amplified signal from the InSb detector has the same time duration as the FEL

macro pulse, approximately 1-5 μS. An HP 54504 digital oscilloscope is used to

accurately sample the InSb signal at the same delay time in each macro pulse. As

shown in figure 3-14b, the DSO uses the signal from the beam monitor (EBM) to derive

a sweep trigger. At a time t_s, after the trigger at t_o, the DSO averages the detector signal

and the EBM signal over a period t_{avg} (typically 50-100 nS). The DSO then reports both average values to the control program running on the Mac IIci.
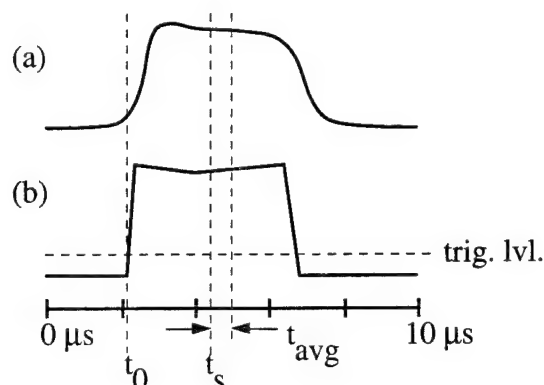
Fig. 3-14. Timing for sampling of InSb and beam monitor signals. Upper trace (a), from InSb preamp; lower trace (b), from beam monitor.

During a data collection run, the Mac IIci computer controls both the FTS stepper motor and the data transfer from the DSO. Program initiation starts with the operator indicating the FTS scan step size, scan direction, the number of steps, and the DSO values for t_s and t_{avg}. The program then repeatedly steps the FTS motor, waits for a FEL macro pulse, and stores the EBM and InSb signal levels corresponding to the mirror displacement. The data is stored and later processed using the Igor software package. Currently the overall system sample rate is limited by the data acquisition system to approximately one FTS sample per second even though the FEL generates 10 macro pulses per second (the limiting data collection rate).

3.3.6 Calibration System

A black body source was used to both check general FTS operation, and also, by monitoring known strong atmospheric absorption lines, verify FTS frequency calibration. Shown in figure 3-15, the black body source was build using nichrome wire wrapped on a coarsely tapped machinable ceramic rod of 0.5" diameter. The ceramic rod assembly was housed inside a small aluminum box, with a 0.5" diameter

hole in front of the nichrome wrapped portion of the ceramic rod. The source was powered by a standard adjustable Variac transformer.

To provide a measurement of the rod temperature, an Alumel-Chromel (type-K) thermocouple is mounted in a hole in the bottom of the ceramic rod. The thermocouple wires connect to an Analog Devices AD595 thermocouple amplifier [Analog Devices, 1991]; this device yields a temperature proportional voltage output of 10 mV/°C.

Because the black body source produces extremely small signals, a chopper and lockin amplifier (Stanford Research Systems Model SRS 510) were used in place of the DSO to monitor the thermal signal. When using the lockin, the control system software was modified to give an appropriate delay between stepper motor motion and lockin signal measurement.

Side View   Front View

Ceramic Rod

Nichrome Wire

Thermocouple

Aluminum Case

Thermocouple
leads to electronics

CeramicElectrical
Feedthrough

Heater Wires to Variac
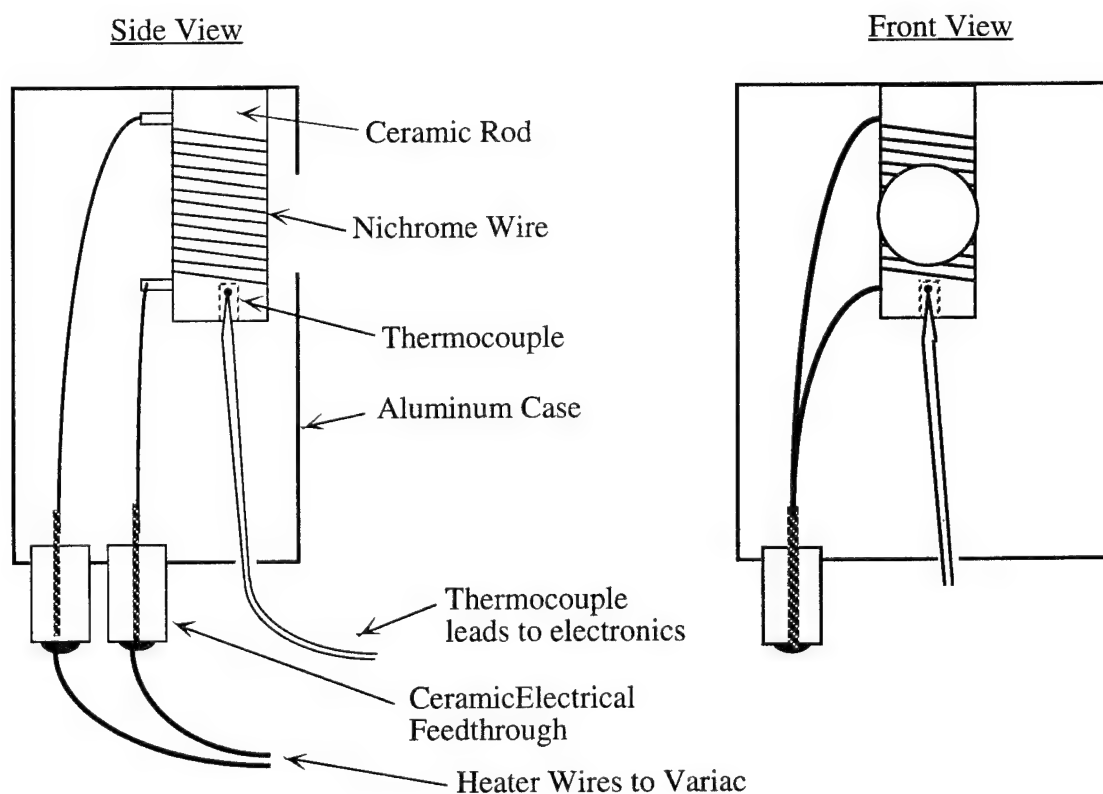
Fig. 3-15. Black body source mechanical design.

3.3.7 Heterodyne Spectrum Analyzer

Narrow band (BW <100 kHz) frequency analysis of the microwave signal emitted by the electron beam was also performed using a Tektronix 2782 spectrum analyzer[**]. The analyzer had a measurement range of dc to 40 GHz, with programmable bandwidth, scan times, etc. and a low noise floor (< -75 dBm).

3.4 Summary

This chapter has described all of the equipment used in these experiments. The next chapter presents and discusses the results from the actual experimental trials. Subsequent chapters will discuss changes and improvements to be made in the original equipment.

[**] The spectrum analyzer was made available for these experiments by Bob Rodriquez and Don Fritch of Tektronix. Their generous support is greatly appreciated.

Chapter 4
Results and Discussion

The purpose of this chapter is to display the results of the measurements made by the FTS on actual electron beams. However, literally hundreds of data scans have been taken, over a period of several months, under varying conditions, on two different electron beam systems. Although only a limited amount of data is reproduced here, it is typical and illustrative of the operational characteristics of the FTS and electron beam systems.

This chapter will layout those results functionally. First, the basic characteristics of the FTS are demonstrated, based on results from a black body source. Measurements of FEL operation will be shown and discussed, included electron beam fluctuations, and measurement of picosecond electron bunch widths. Data from the Picosecond Electron Bunch System (PEBS) is presented showing an alternative electron beam interaction device and the correlation between measured bunch width and alpha magnet slit size (and electron energy spread). Finally, as an alternative to the FTS, a spectrum analyzer is used measure the electron bunch generated RF.

4.1 System Verification

It is important to understand the response of the measurement instruments so that experimental signals can be separated form instrument characteristics. For the work discussed here, the measurement system response is made up of two parts: spectral performance of the interferometer, and transient impulse response of the detector electronics.

4.1.1 FTS Black Body Calibration of Interferometer

During design and operation, the FTS system spectral response was characterized and monitored by measuring thermal blackbody sources. The sources are simple nichrome heaters, with embedded thermocouple thermometers. These sources have a theoretical spectral radiance predicted by Planck's blackbody radiance law [Boyd, 1983, pg. 49] ,

$$L(f) = \frac{2hf^3}{c^2} \frac{1}{\exp(hf/kT) - 1} \tag{4.1}$$

and shown in figure 4-1. When the response of the beamsplitter (predicted by (2.56)) and the detector (equation (3.7)) are included, the theoretical response of the FTS to a blackbody source is shown in figure 4-2.
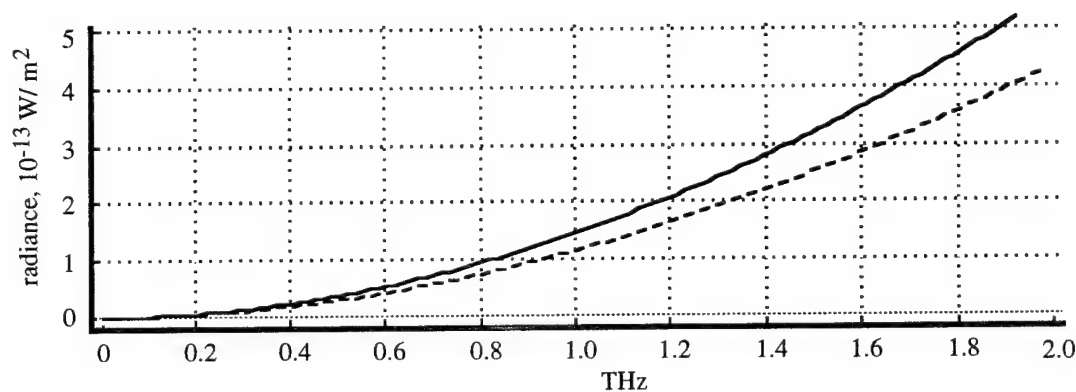

Fig. 4-1. Theoretical black body spectral emission from source at various temperatures. Solid line, 500 K; dashed line, 400 K.
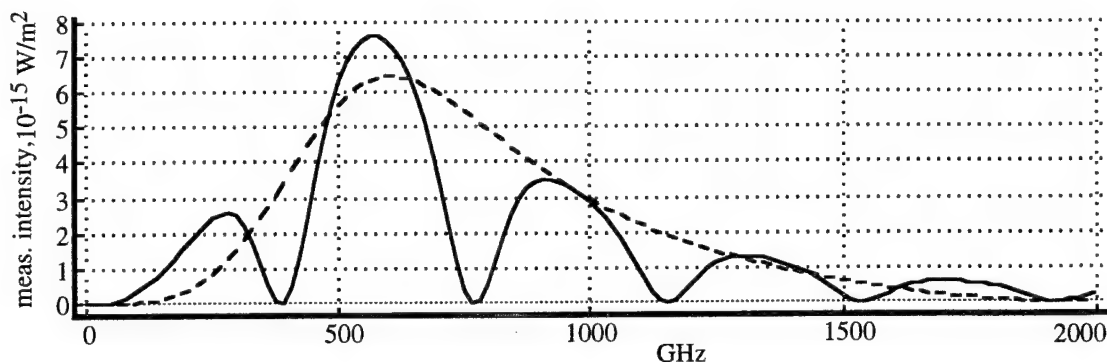
Fig. 4-2. Theoretical FTS response to black body source including predicted beamsplitter and detector spectral response. Black body temperature set at 450 K. Solid curve for 270 μm beamsplitter, dashed curve for 50 μm beamsplitter.

Figures 4-3 and 4-4 shows typical experimental measurements of the FTS response to the black body source. Superimposed on the experimental data are the theoretical curves based on figure 4-2 adjusted for the measured black body temperature (450 K) and fit for InSb bolometer response, component losses, and beamsplitter filtering. In both figures, the best fit for the InSb detector spectral response, including component losses, is,

$$\eta_{InSb} = (\ 1 + (f/600)^5\ )^{-1} \tag{4.2}$$

where f is frequency in gigahertz. This is more pessimistic than commercial detector specifications [QMC Instruments Ltd., 1992] , and hot-electron bolometer theory which predict the rolloff to depend on the square of the frequency (§3.3.3). Note, however, that figure (4.2) reflects not only the detector spectral response, but also the spectral response of interferometer components not modeled by the beamsplitter rolloff or detector spectral response. Equation (4.2) is, however consistent with the spectral loss estimates from §3.3.3; assuming a component spectral attenuation proportional to f^{-3}, the combined response of both the FTS components and the InSb bolometer would yield a f^{-5} dependent FTS spectral rolloff.

Figure 4-3. FTS black body response and fit to theoretical system model for 55 μm beamsplitter. Bold curve is model, single width curve is experimental data. Blackbody temperature, 456 K. *filename: Igor FTS BB Fits [datafile:931216.1705]*

94

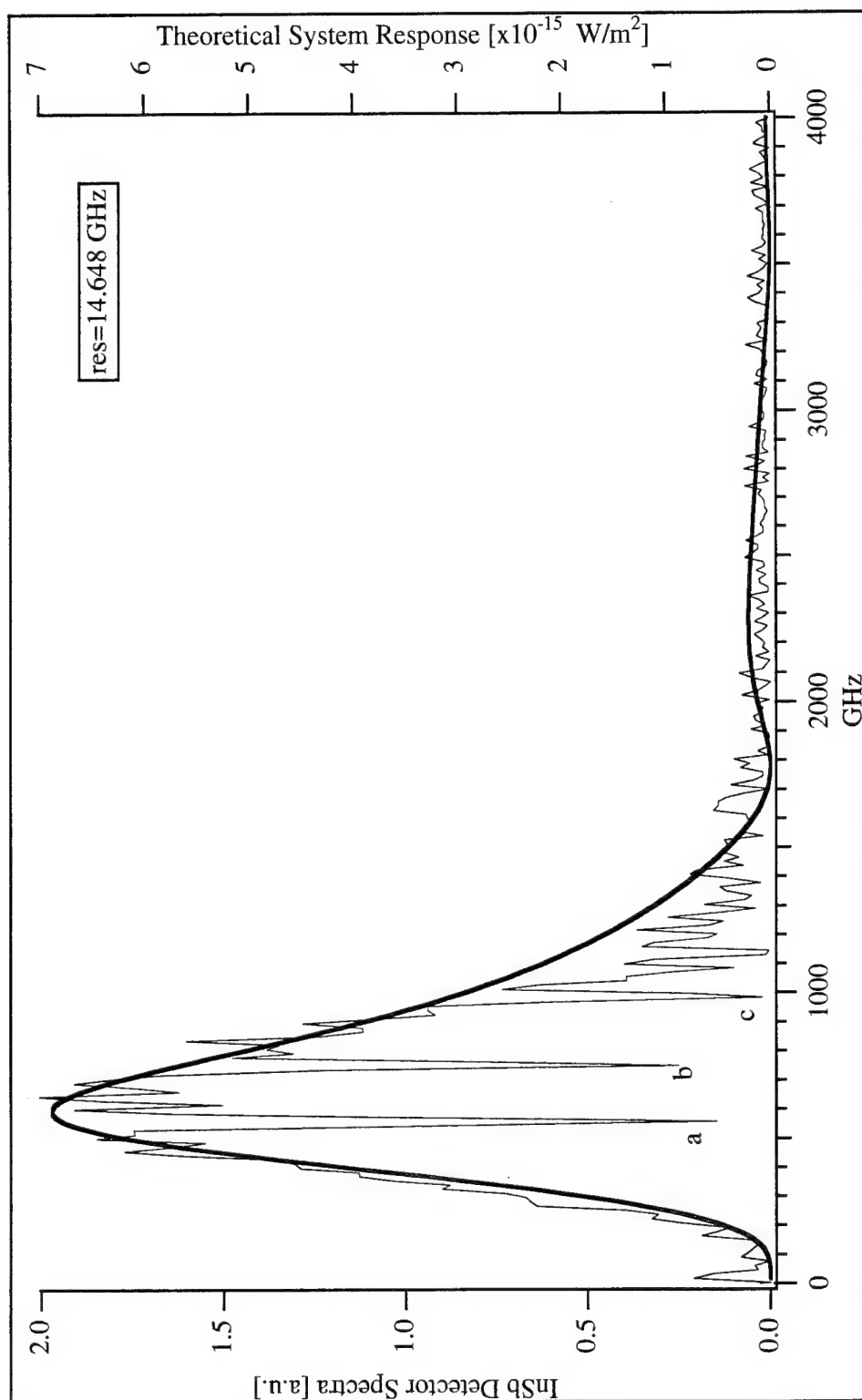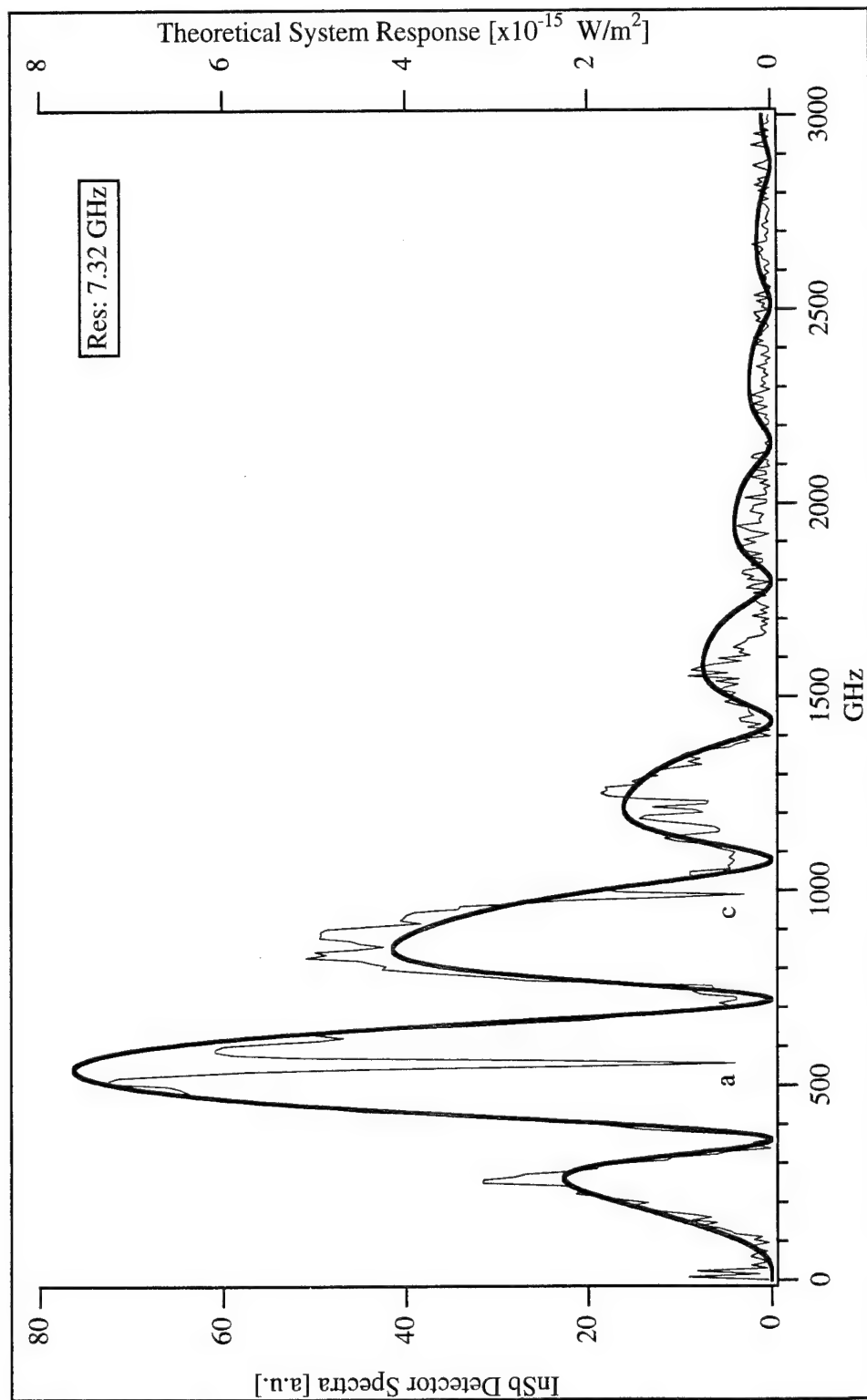Figure 4-4. FTS black body response and fit to theoretical system model for 270 μm beamsplitter. Bold curve is model, single width curve is experimental data. Blackbody temperature, 450 K.
filename: Igor FTS BB Fits {datafile:930910.1807}

Using equation (2.56), the zeros of the beamsplitter response are related to the beamsplitter thickness. By fitting the beamsplitter model to the data, the actual beamsplitter thicknesses are found to be slightly thicker than the manufacturer specification. The 250 μm beamsplitter is actually approximately 270 μm thick, whereas the 50 μm beamsplitter is 55 μm thick. These discrepancies are only minor and have no impact on the electron beam pulse measurement.

Both figures reveal several strong absorption peaks. As shown in Table 4-1, these lines correspond to atmospheric water absorption. Although it is possible to purge the entire interferometer and beam line with dry nitrogen, because these lines are narrow compared to the electron beam spectra, no effort was made to remove the water vapor from the system. Figures 4-3 and 4-4 both clearly show the lines at 557 GHz (a) and 988 GHz (c). The 752 GHz (b) line is obvious in 4-3, however, in figure 4-4 this line is obscured by the beamsplitter minimum at ≈760 GHz.

Table 4-1. Water vapor absorption lines at S.T.P. from [Everitt and Hensley, 1989; Sheppard, et al., 1970]. The lines at (a),(b), and (c) are highlighted in figures 4-3 and 4-4.

frequency (GHz)	atten. coeff. [cm^{-1}]	% trans., 100 cm	% trans., 1000 cm
380	$0.1299 * 10^{-2}$	87 %	27 %
448	$0.1375 * 10^{-2}$	87 %	25 %
557 (a)	$0.7305 * 10^{-1}$	0.067 %	0 %
752 (b)	$0.5072 * 10^{-1}$	0.063 %	0 %
916	$0.2250 * 10^{-2}$	80 %	10 %
970	$0.2725 * 10^{-2}$	76 %	6.6 %
988 (c)	$0.3702 * 10^{-1}$	2.5 %	0 %

The experimental data shows a good fit to theory below 1500 GHz. However, above 1500 GHz the theoretical model falls into the noise floor of the experimental data. Although increased signal averaging or reduced component attenuation would improve the response above 1500 GHz, the theoretical models accurately predict the FTS response over the spectral range at which most of the electron beam characterization is studied. Because the FTS worked predictably in the spectral range of interest, further improvement of the system response was not pursued.

The autocorrelation impulse response of the FTS is obtained by taking the inverse transform of the spectral response of the FTS system with unity spectral input. Taking the inverse transform of the estimated FTS response including system losses and the beam splitter function, yields time domain autocorrelations shown in figure 4-5. The thinner beamsplitter yields better response, however, neither beamsplitter yields ideal impulse response. This is due to the spectral rolloff in the system components; by using optics with less high frequency loss (so that the optical spectral rolloff is not as severe as f^{-3}) shorter pulses could be measured. Using the 50 μm beam splitter, the current FTS can measure pulses with 1 pS autocorrelation width. Figure 4-6 shows the response when ideal optics are used and only the detector has a f^{-2} rolloff at 600 GHz; this system would be limited to measuring pulses with 800 fS autocorrelation width.
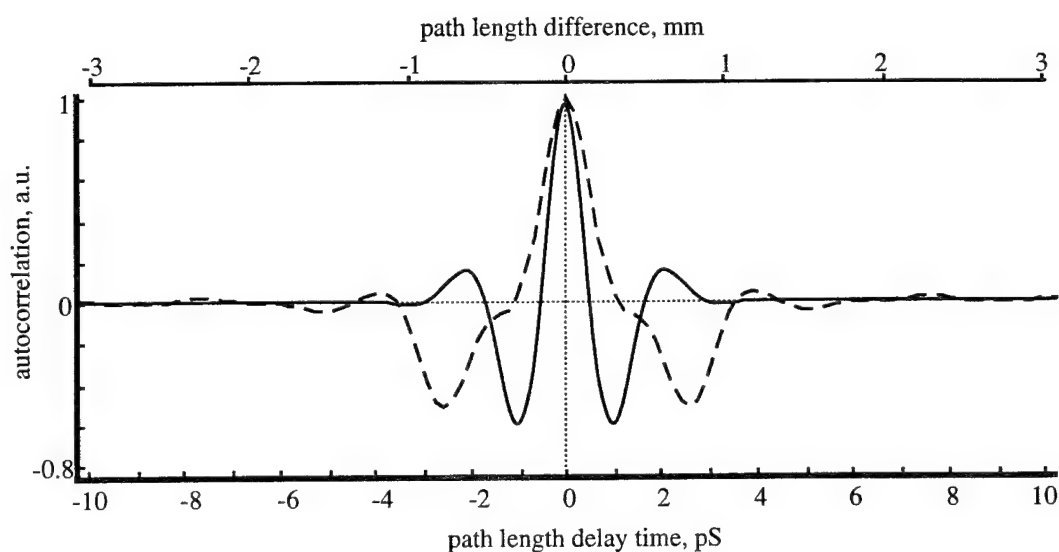
Fig. 4-5. Estimated total FTS impulse response. Solid curve, 50 μm beam splitter, dashed curve, 250 μm beam splitter.
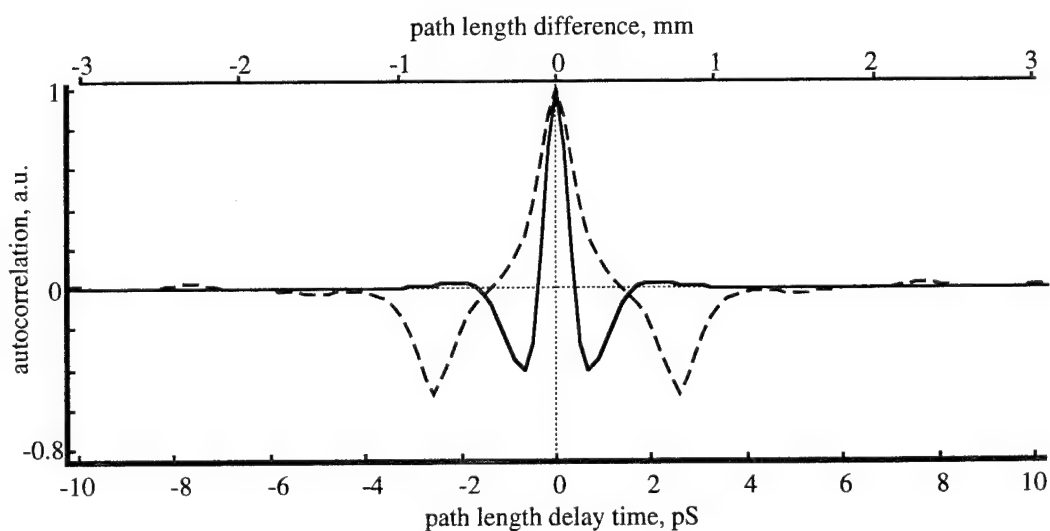
Fig. 4-6. Estimated FTS impulse response due to detector spectral sensitivity. This estimate is based on only the detector having a f^{-2} spectral rolloff. Solid curve, 50 μm beam splitter, dashed curve, 250 μm beam splitter.

Using the measured spectral impulse response of the FTS system, we may estimate the FTS response to electron bunch transients of different shapes. Figures 4-7 and 4-8 show computed estimates of the FTS measurement on gaussian and rectangular shaped pulses. From these figures we may see that the low frequency rolloff of the FTS, due to the beam splitter response, produces an effect of differentiation on the measured signal. The high frequency rolloff, due to the detector, leads to a smoothing, or averaging, of the original electron beam signal. Also note that for pulses widths of less than 1 pS, the FTS response makes pulse shape identification impossible. By measuring the width of the two minima on either side of the central peak, it is possible to determine if a pulse width is less than 1 pS. Section 4.2 will use the estimates presented in these figures as a basis for calculating the electron transient pulse characteristics.

Fig. 4-7. Computed estimates of FTS response to Gaussian transient. These figures are based on the measured FTS response and gaussian pulses with 1/e half widths indicated on the left. The absciccae, above, are for interferometer arm full path change, either in displacement in mm, or delay time, in pS. The label on the left of each pulse is the propogation delay time.

Fig. 4-8. Computed estimates of FTS response to rect() transient. These figures are based on the measured FTS response and rect() pulses with half widths indicated on the left. T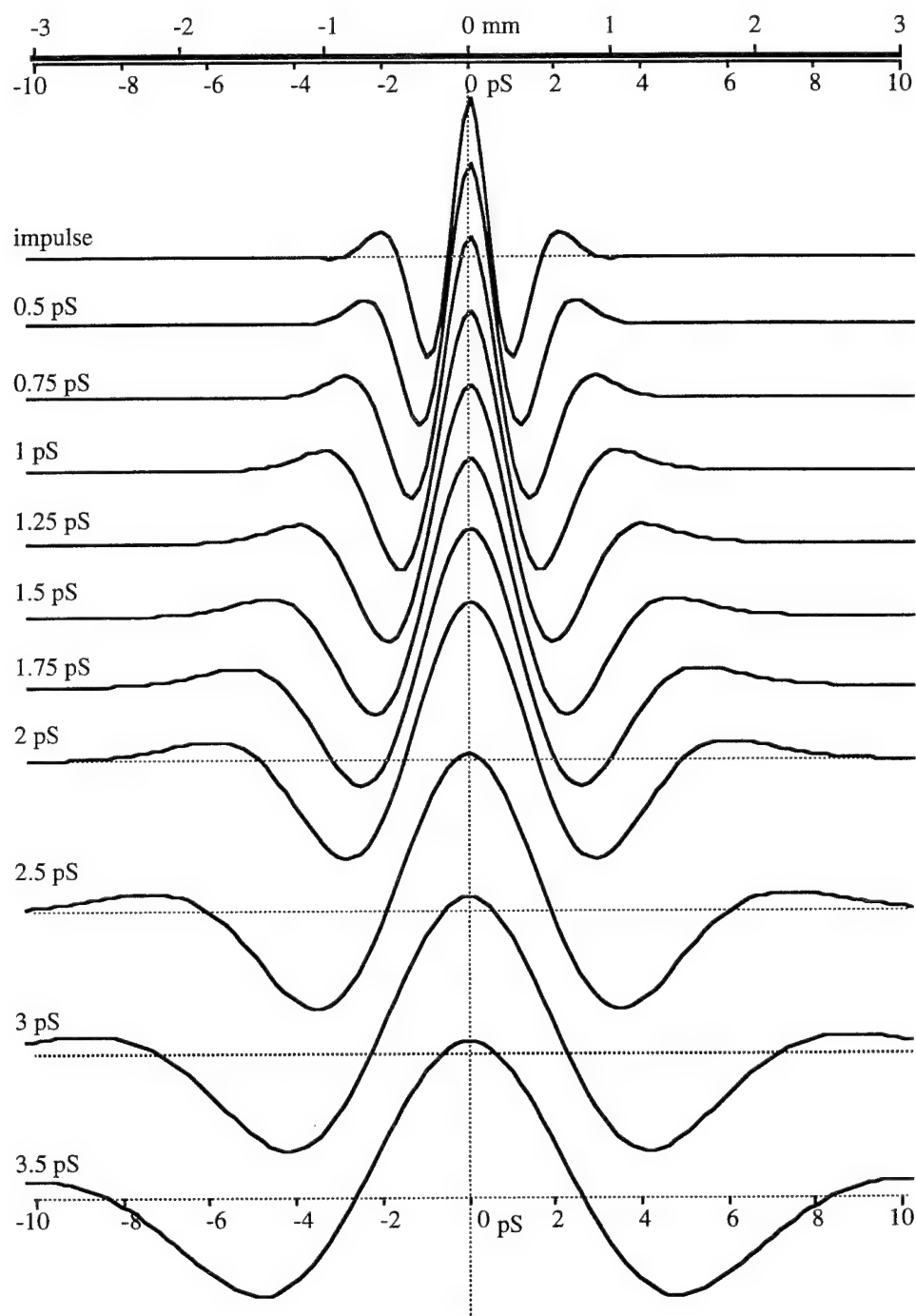he absciccae, above, are for interferometer arm full path change, either in displacement in mm, or delay time, in pS. The label on the left of each pulse is the propogation delay time. *filename:RectPredFigs.Word*
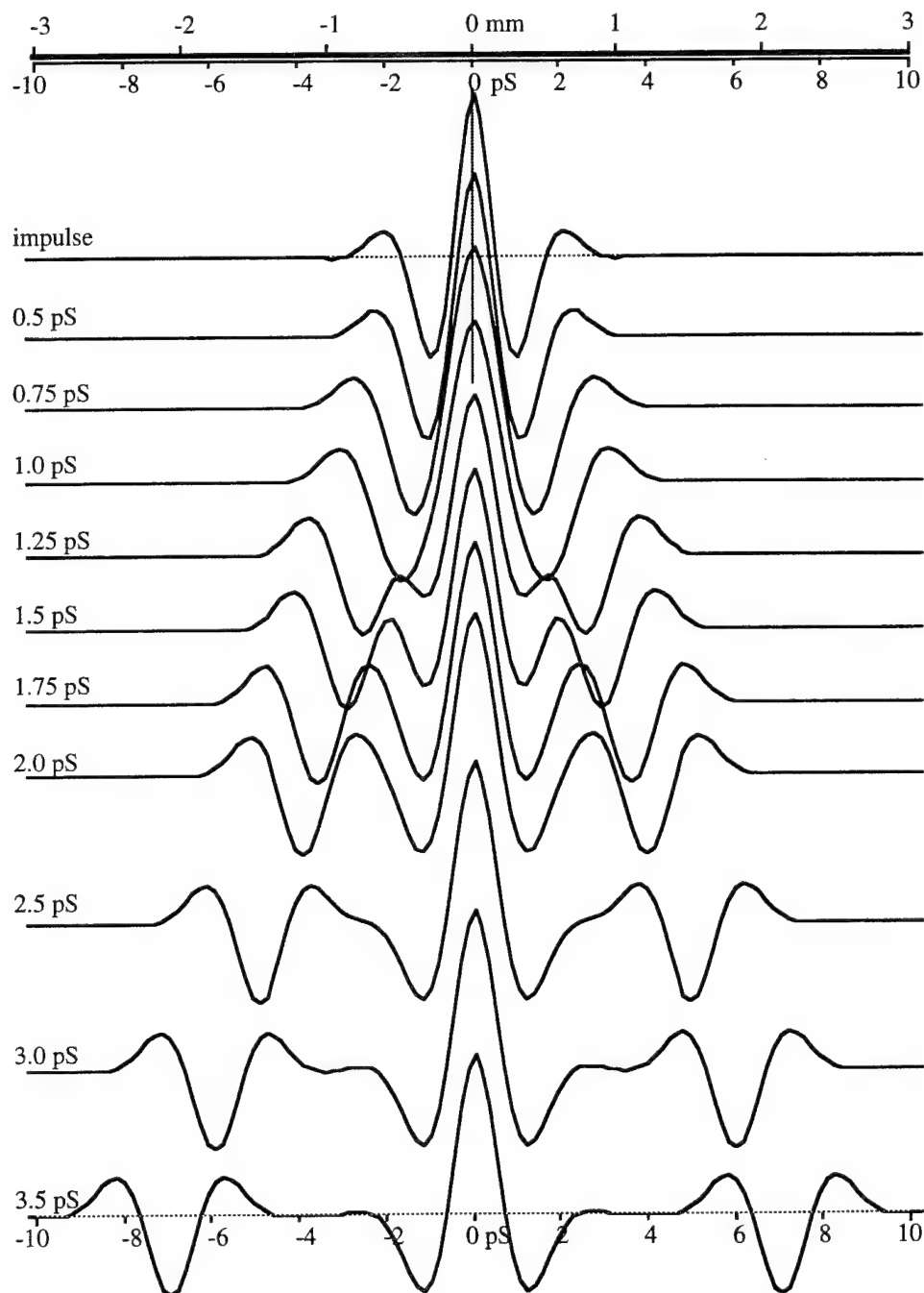
4.1.2 Beam Monitor Characteristics

In this work various devices were tried as electron beam monitors (EBM) to trigger the sampling electronics and to monitor the beam current. In the experiments performed on the FEL, an X-band waveguide-to-coax transition with a 1N23 detector served as the EBM. The X-band transition was placed next to the FEL current toroid, a few centimeters radially out from the LINAC ceramic break. As shown in figure 4-9a, this device worked well as trigger for the sampling electronics, virtually replicating the FEL low frequency current toroid signal, because the electron beam spectrum is virtually flat from DC to a few tens of gigahertz. Hence, an X-band signal is essentially the same as the low frequency pulse train envelope signal. Unfortunately the X-band signal is dependent on the electron beam position; with, only one detector, it was not possible to determine whether train-to-train signal variations were due to current or position variations. At best the X-band detector provided rough measurement of beam current status, indicating gross electron beam variations or failures. A far better monitor for this work would have been a second InSb detector, sampling a portion of the electron beam signal just before the FTS. Such a detector would have the same spectral response as the FTS detector, yielding a signal proportional to the total emitted power, and therefore also useful for broadband power normalization. With appropriate electronics this InSb monitor response could be made fast enough to serve as a sampling system trigger.

4.1.3 Video pulse response of FTS System

As discussed in the last chapter, the electron bunch trains are not continuous, rather the trains are chopped, producing groups of bunches 1-4 μS in duration, at a rate of 1-10 Hz. To accurately sample the chopped trains, the InSb detector and electronics should have a response time, often called video response to distinguish this from the spectral

response, comparable to or faster than the chopped signal. During one set of FEL data runs, the pulse trains were made 0.1 μS long. During that run, the response time of the InSb detector was tested. Figure 4-9 shows 0.1 μS pulse as measured by the X-band detector, the signal directly from the InSb detector, and the InSb signal amplified (using an Analog Devices AD844 configured as a x100 DC preamp). Note that the InSb signal was DC coupled to allow chip resistance calculations. The direct InSb signal (figure 4-9b) has an approximately exponential rolloff with a response time of ≈400 nS, corresponding to 3 dB bandwidth of 2.5 MHz. The InSb signal amplified by the AD844 preamp shows a slightly slower response of ≈600 nS, or a 1.67 MHz bandwidth (figure 4-9c) . These results compare favorably to the estimated carrier lifetime of ≈0.2 μS for InSb.
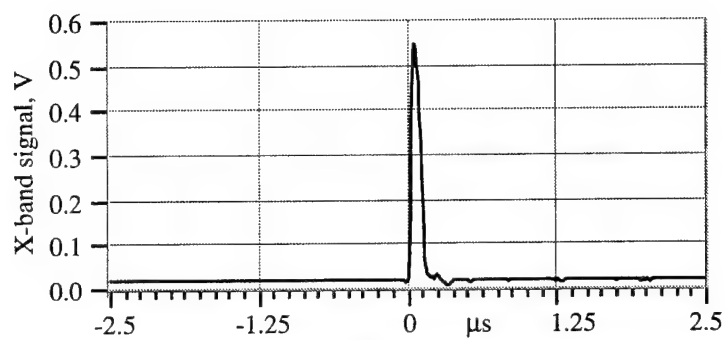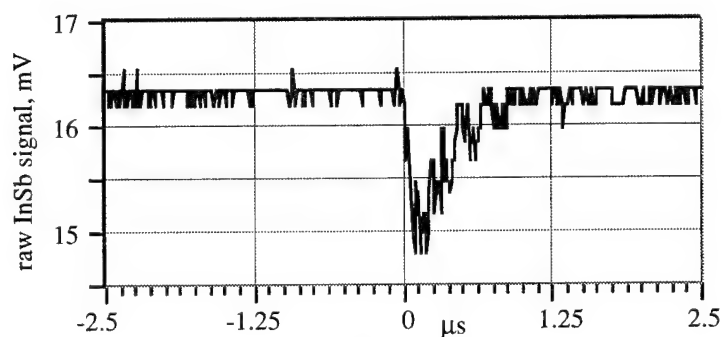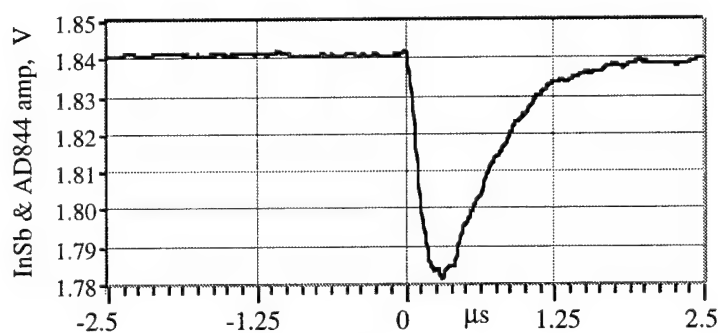
Fig. 4-9. Impulse response of InSb bolometer. a) Signal from X-band current monitor showing 100 nS electron bunch train. b) Signal directly from InSb bolometer (no amplifier). c) Signal from InSb bolometer amplified by AD844 x100 preamp.

4.1.4 Noise Characteristics

Because the detector and FTS instrumentation was located within a few meters of the FEL electron beam pulse forming electronics and klystron, both sources of strong EM noise, care was taken in shielding the InSb signal. As shown in figure 4-9b, the raw InSb signal level has a magnitude of only a few millivolts. Figure 4-10 shows the signal from the detector with no input FTS signal. The noise on this signal is due to both oscilloscope digitization errors and external pickup. The HP 54504A oscilloscope has a vertical accuracy of 0.4% full scale [Hewlett-Packard, 1993]; for figure 4-10, full scale was 56 mV, yielding a digitization accuracy of 0.22 mV. This level corresponds to the noise over a majority of the sampled period. However, within 1 μS of the electron beam generation, at 0 μS, the noise exceeds the oscilloscope sampling noise, and is from the FEL firing electronics. The noise appears to be a high frequency ringing; because the preamps used have high frequency rolloffs of approximately 1 MHz, this noise is removed by the preamp.
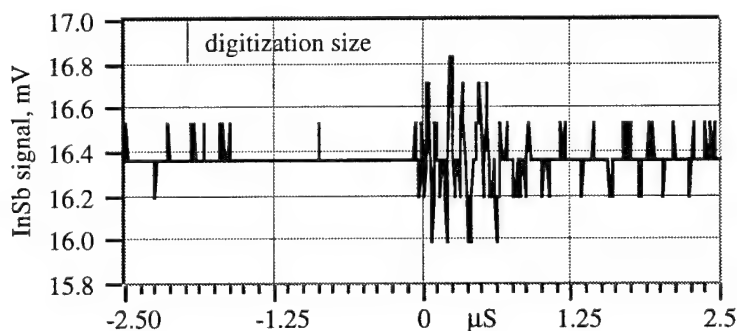
Fig. 4-10. Noise on un-amplified InSb detector signal. Signal directly from InSb detector electronics measured on HP 54504A oscilloscope. The digitization accuracy of the oscilloscope is 0.22 mV.

4.2 FEL Measurements

A variety of experimental configurations were tried in analyzing the FTS system response and the electron bunch characteristics. This section highlights typical measurements taken on the Mark III FEL and the Duke PEBS.

4.2.1 Electron Beam Transient Measured through Ceramic Break

The first electron beam measurements were made with no proper interaction region; instead, the signal transmission waveguide was simply brought to the ceramic break, as shown in figure 4-11. Figure 4-12 shows data from a typical FTS scan using this simple pickup scheme.
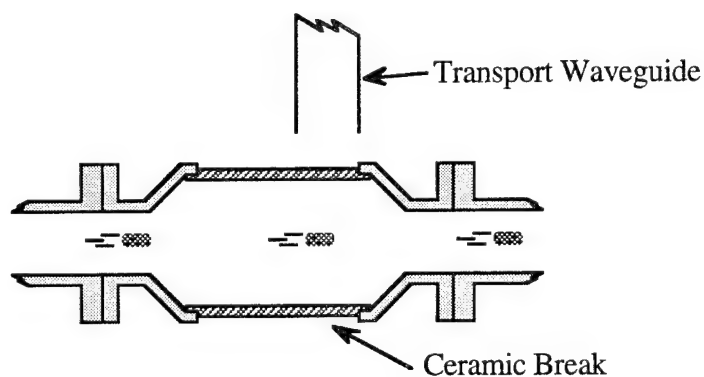
Fig. 4-11. Simple electron beam sampling through ceramic break by transport waveguide.

Several comments are required about the data presented in figure 4-12. The interferogram from the InSb detector is quite symmetric and shows little noise from current fluctuations as monitored by the X-band detector. Immediately proceeding this data run, InSb fluctuations were measured against X-band fluctuations, and a 10 mV X-band change yielded a 100 mV InSb change; therefore the interferogram is not appreciably affected by beam current or position variations. The computed spectrum of the interferogram shows quite a bit of structure, due to the oscillations on either side of

the interferogram peak: the strong signal at 70 GHz corresponds to an interferogram period of 4.3 mm; the 105 GHz signal, corresponds to a period of 2.9 mm.

There are several possible causes for these oscillations. The electron beam must be the source of any spectral energy. Therefore the sharp spectral peaks could be due to a small periodic current superimposed on the electron bunch. The sharp peaks could also be due to filtering between the electron beam and the FTS. One possible filter source would be an etalon effect in the alumina wall making up the ceramic break. Figure 4-13 shows the transmission of an alumina window of the dimensions used in the ceramic break. Although the transmission characteristics could be made to overlap with select peaks in the interferogram spectra, the overall transmission pattern is not dominant in the electron beam signal. It has been suggested that absorption in the ceramic break due to impurities in the alumina may cause spectral filtering; however, absorption filtering should have a broad band effect, and not pass very narrow spectral lines.
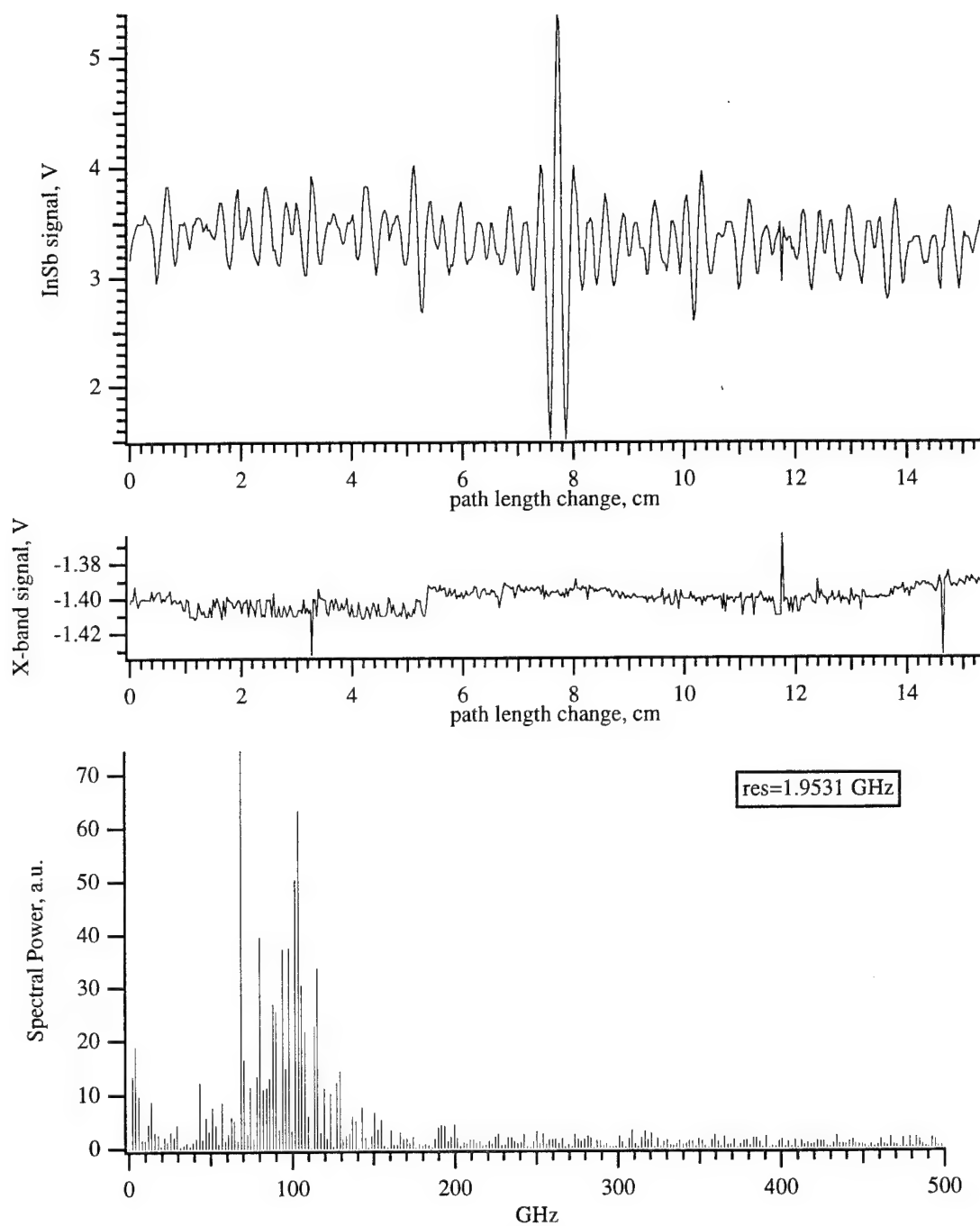
Fig. 4-12. FTS data measuring electron beam through ceramic break wall. Parameters: waveguide 10.5" from ceramic break; 9.4 " lens collimating waveguide output; 12.4" lens at detector horn; 10 mil BS; #smpls=512; steps/smpl=30;For;scope dly=2.00(us);full scr=50(ns);*datafile:931026.2138*
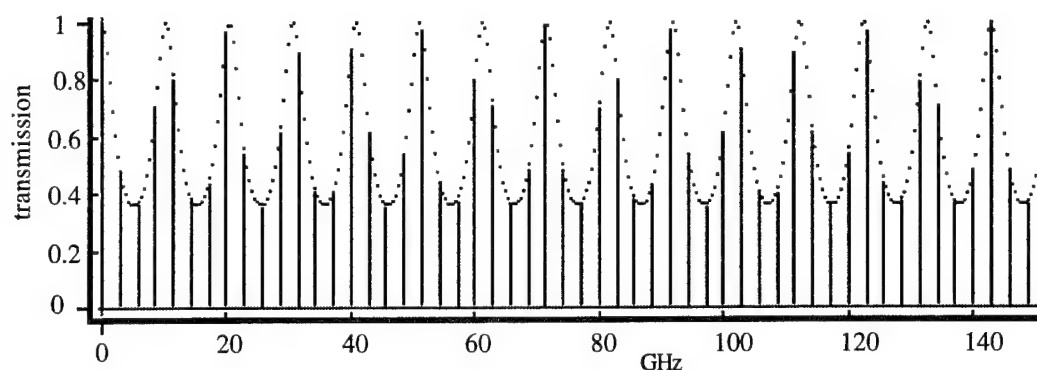
Fig. 4-13. Transmission due to etaloning in alumina (n=9). Wall thickness of 4.9 mm corresponding to the dimensions of the ceramic break. Dotted curve is the continuous transmission function of the etalon; lines from zero indicate spectral lines at the electron bunch frequency spacing of 2.8565 GHz.

4.2.2 Electron Beam Measured by Waveguide Pickup

Unlike the measurements made through the ceramic break, fewer unknowns and a more precise model exist for sampling the electron beam transient using a waveguide pickup. Typical FTS data is shown in figure 4-14. The FTS configuration is essentially the same as that used in the measurements of §4.2.1, except an attenuating aperture (a 5 mm diameter hole cut in Eccosorb sheet) was placed in front of the transport waveguide output; the aperture partially acts as a high pass filter (spectral components whose wavelength is greater than 5 mm are partially attenuated); because the low frequency components are not as significant in forming a narrow interferogram peak, the ability of the FTS to measure short pulses is not significantly hampered by this filtering.
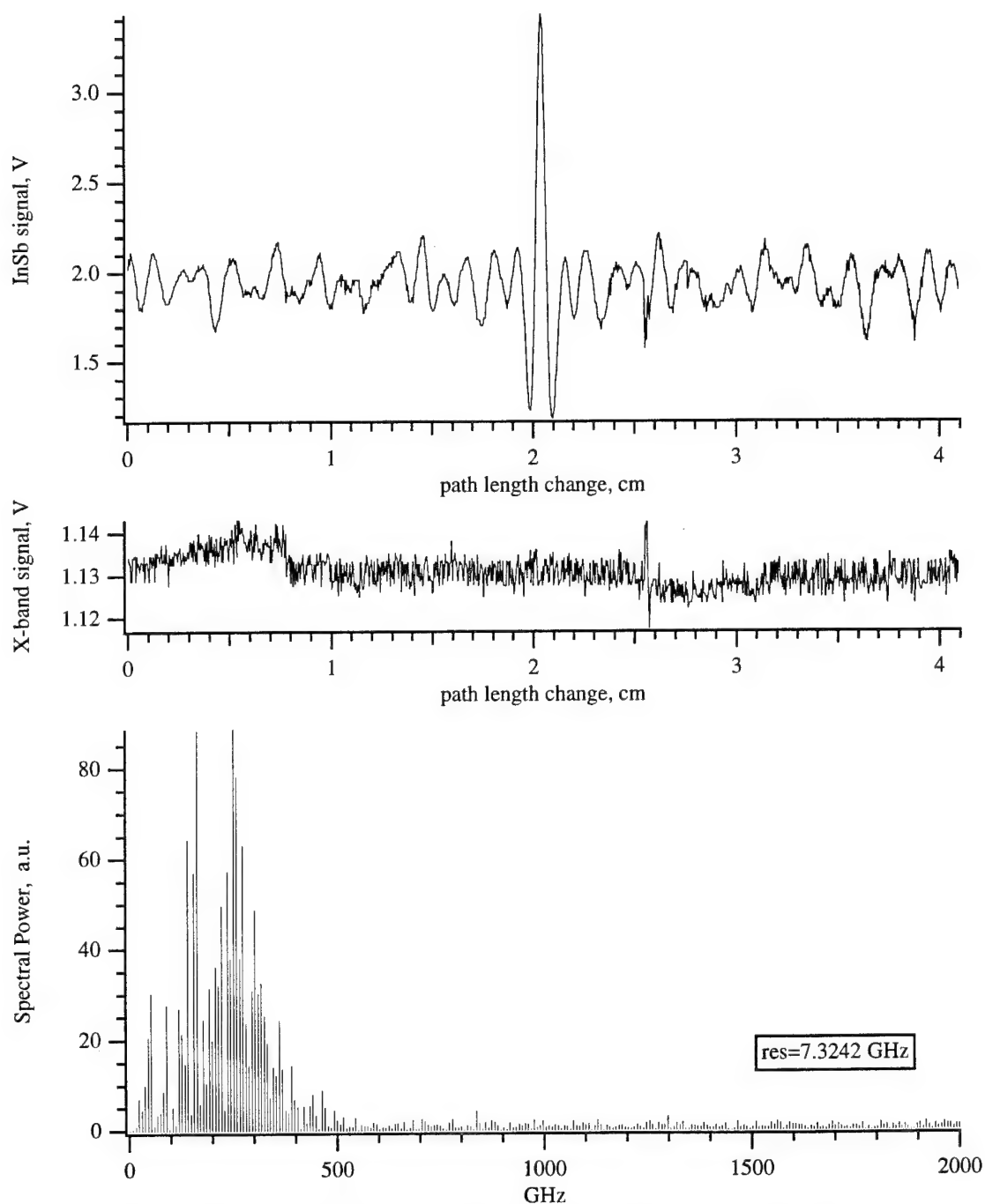
Fig. 4-14. FTS data of Mark III sampled by waveguide pickup.
Parameters: 2 mil BS; 5 mm aperture in Eccosorb at waveguide output;
9.4" lens collimating signal from aperture output;12.4" lens at detector horn;
Quartz window at waveguide pickup Tee; #smpls=1024;step/smpl=4;Rev;
scope dly=3.00 μS; scope window=50nS; StopTime:931210.1421

In November 1993, the FEL electron gun system was modified, incorporating a new, realigned cathode and a rebuilt RF pulse forming network (PFN). The result of the FEL modifications and realignment produces a significant change in the electron bunch duration and spectra. The effect of these modifications was immediately evident on the FTS interferograms, shown in figure 4-15. Before modification (12 Oct 93) the electron pulse produced an interferogram with a central peak full width of ≈ 5.0 pS; after FEL modification (10 Dec 93), the pulse produced a central peak with a ≈ 2.6 pS width. Although not shown here, the signal spectra before FEL modification did not extend past 200 GHz, whereas after FEL modification the spectrum extended to beyond 400 GHz. The 10 Dec 93 spectra has significantly more high frequency content, corresponding to a much shorter electron bunch duration. It is important to note that the FTS technique immediately identified the change in electron beam bunch characteristics.
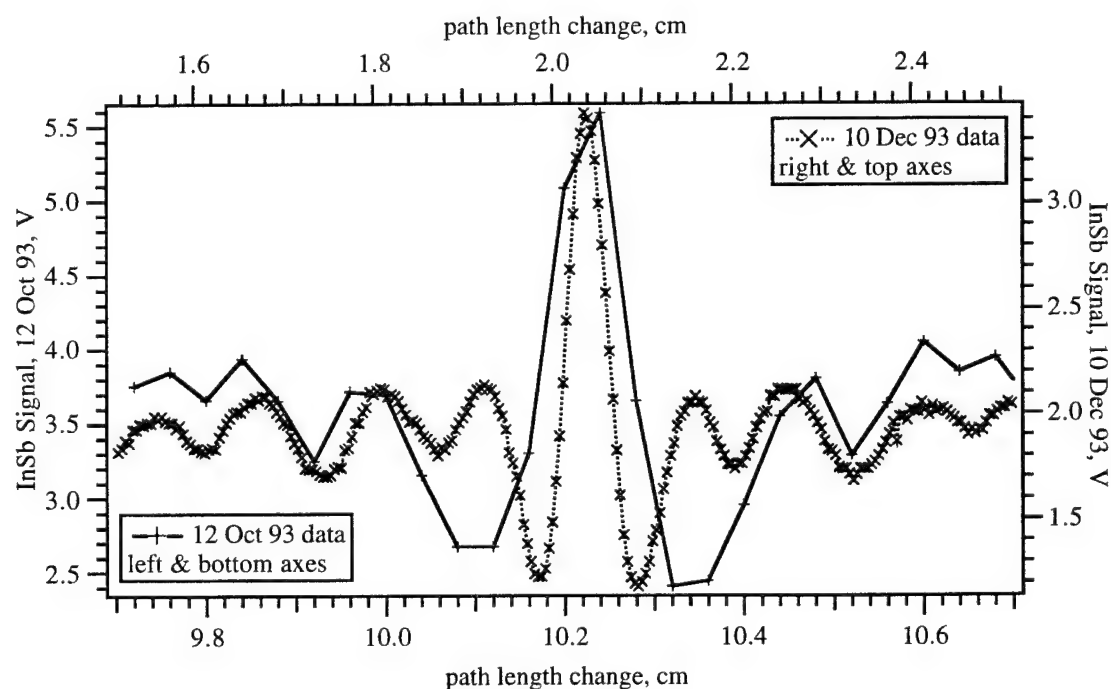
Fig. 4-15. Comparison of FTS interferograms before and after Mark III modifications. Note that although the 12 Oct 93 data had a coarser step size (400 μm/sample) than the 10 Dec 93 data (40 μm/sample), the autocorrelation peak is still evident.

Figure 4-16 show the fit of the measured interferogram (autocorrelation) to the autocorrelation of a 1.3 pS gaussian pulse filtered by the FTS system response.
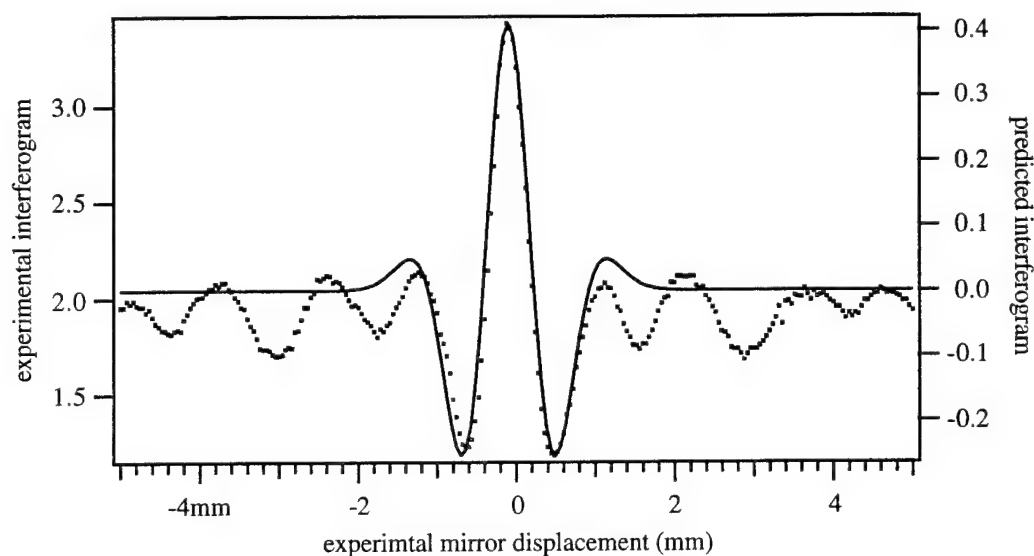
Fig. 4-16. Measured (dots) and predicted (solid) interferogram data from Duke Mark III FEL. Predicted fit is for a 1.3 pS gaussian pulse.

4.2.3 Electron Beam macro pulse diagnostics

The previous sections have considered the autocorrelation of the electron beam signal in order to measure the electron bunch width. The InSb detector output, independent of interferometer operation, however, also yields electron bunch diagnostic information. The reason for this is that the InSb detector signal reflects the high frequency (>40 GHz) power produced by the electron bunch transient. Therefore, the raw InSb video signal will give a relative indication of the whether the electron beam is producing bunches of short or long duration.

Figure 4-17 shows the InSb detector signal as the FEL RF drive level is varied. The InSb signal clearly shows a shifting of short pulse energy to the end of the pulse train as the RF drive level increases. The X-band signal changed negligibly during the RF
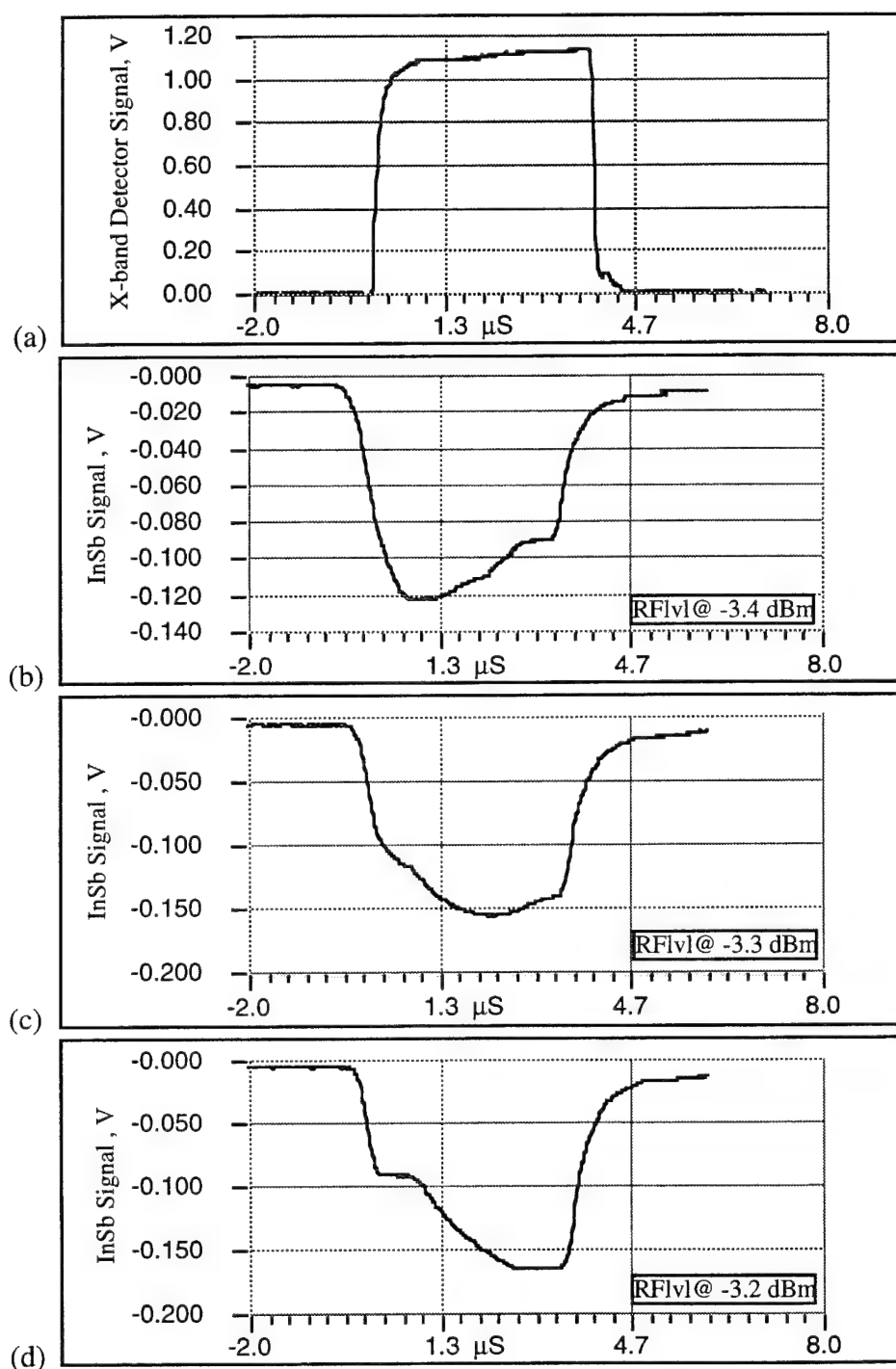
Fig. 4-17. InSb video signal evolution during electron train burst versus FEL RF drive level. The InSb detector signal was recorded at a fixed FTS path length.

drive level variation. Although these results are relatively crude, it is clear that the electron bunch duration changes from beginning to end of the pulse train, and that change is measurable by a simple millimeter detector.

Because the InSb detector electronics have sufficient response speed to track the electron pulse train (macro pulse) evolution, the FTS system was next used to measure the electron bunch duration near the beginning and end of the pulse train under varying RF drive levels. Pulse width variation from beginning to end of the pulse train is clearly evident in figure 4-18, and the pulse width variation is clearly dependent on the RF drive level. Although not shown, the optical output of the FEL was also dependent on the RF power level, and for the particular configuration at the time this data was taken, the FEL laser output correlated with the last half of the pulse train tracked by the InSb signal.

114
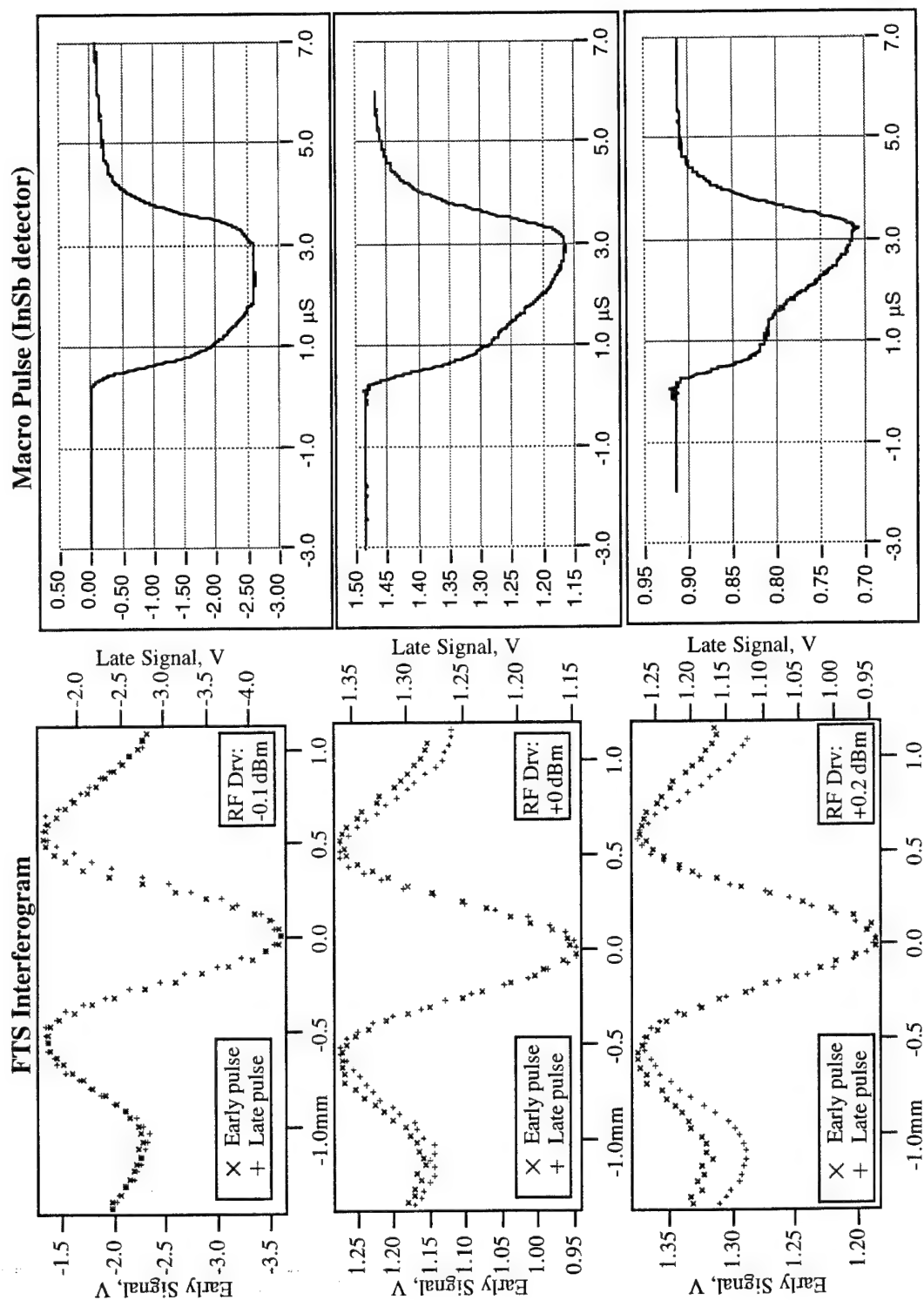
Fig. 4-18. Electron bunch width variation during electron bunch train
evolution (macro pulse) and RF drive adjustment.
filename: RFDrvVsPulseWdth Final

4.3 PEBS Measurements

4.3.1 Basic E-Beam Measured through Waveguide

The PEBS system has been used as a source of 1 MeV electron bunches for tests on different electron beam interaction devices. FTS pulse measurements have been made on the electron beam in this source driving various simple waveguide coupling structures. Recent work has measured the response of waveguides of two different sizes: "large," 1.9 mm x 3.9 mm ($\tau_t = 6.3$ pS), and "small", 0.95 mm x 1.9 mm ($\tau_t = 3.2$ pS).

The interferogram data from the "small" waveguide is shown in figure 4-19. The spectrum of the measured signal is shown in figure 4-20. Attempts to fit this data to either simple rect() or gaussian pulse shapes yielded poor results; rect() shape pulses rolled off too quickly, whereas gaussian pulses did not rolloff fast enough. Various other functions were tried, and a moderately good fit was achieved with a flattened inverted paraboloid,

$$y = 1-(x/.8 \text{ mm})^2 \tag{4.3}$$

shown in figure 4-21.

The spectra of these signals show a jump in power near the TE_{10} and TE_{11} cutoffs at 79 GHz and 177 GHz. There in not enough spectral power in the measured pulse to observe a signal increase at the next cutoff at 325 GHz for the TE_{12} mode. Although not conclusive this data supports the improved model of an electron bunch crossing a waveguide presented in §2.2.2.

Figures 4-22 and 4-23 show the interferogram and spectra for the "large" waveguide in the PEBS. Although neither the electron bunch and the FTS characteristics are changed, the measured signal is much different than that obtained

from the "small" waveguide. The reason for this is that the larger waveguide has a longer characteristic transit time and different cutoff frequencies. The characteristic increase in spectral power at the waveguide cutoffs (at 40 GHz, 88 GHz, and 162 GHz) is clearly evident in figure 4-23. The rapid rolloff in spectral response due to the large transit time is also evident. Again, these data supports the improved model of waveguide modes excited by bunched electrons. Finally, because the electron bunch length is much shorter than the transit time, the overall response of the "large" waveguide is its impulse response.

In the data from both waveguides, there is considerable spectral content below the lowest cutoff frequency. This may be due to stray RF due to transition radiation or other phenomena, coupling into or along the waveguides and being collected and measured by the FTS. Some of this may also be due to spurious interference between components in the interferometer; enclosing the interferometer in a box made of Eccosorb reduced some spurious pickup however, did not entirely remove the low frequency noise. Further investigation is required to determine the source of this signal.
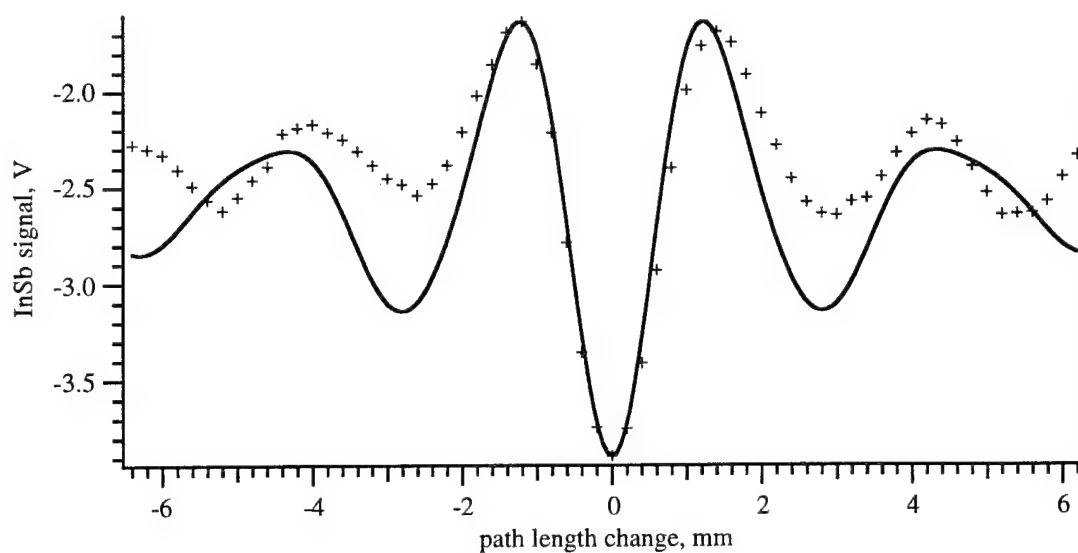
Fig. 4-19. Interferogram of PEBS signal from electron beam crossing "small" waveguide. Crosses are measured interferogram. Solid line is calculated interferogram due to truncated paraboloid shaped pulse. FTS used 250 µm beam splitter.
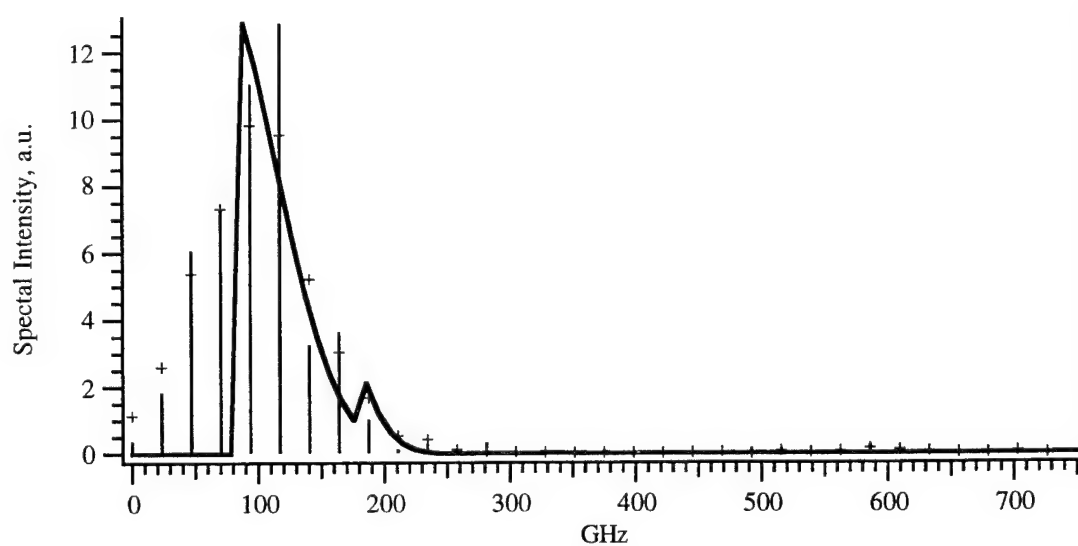
Fig. 4-20. Frequency spectrum of signal measured in figure 4-19. Lines from zero are computed spectra of measured data in figure 4-19, crosses are spectra of measured data apodized by a triangle function. Bold line is spectrum of estimated pulse.
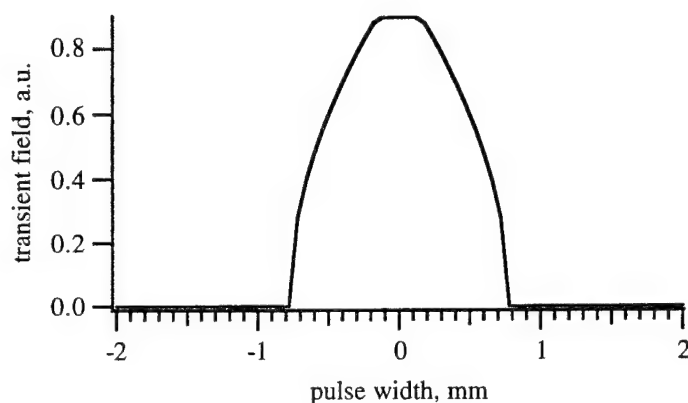
Fig. 4-21. Estimated pulse shape of transient produced by PEBS "small" waveguide. Pulse is flattened inverted parabola.
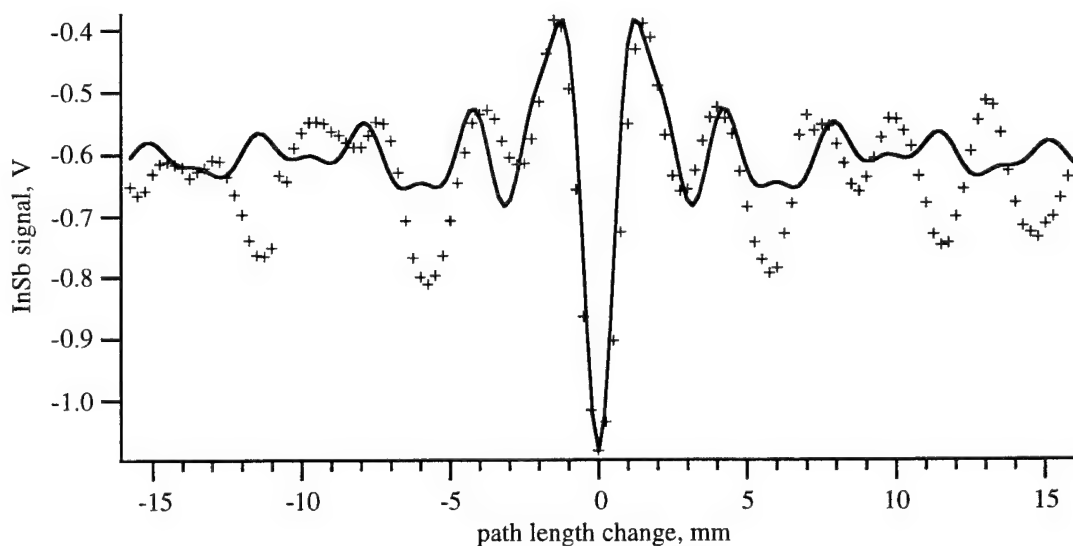
Fig. 4-22. Interferogram of PEBS signal from electron beam crossing "large" waveguide. Crosses are measured interferogram. Solid line is calculated interferogram predominantly due to waveguide and FTS spectral responses. FTS used 250 µm beam splitter.
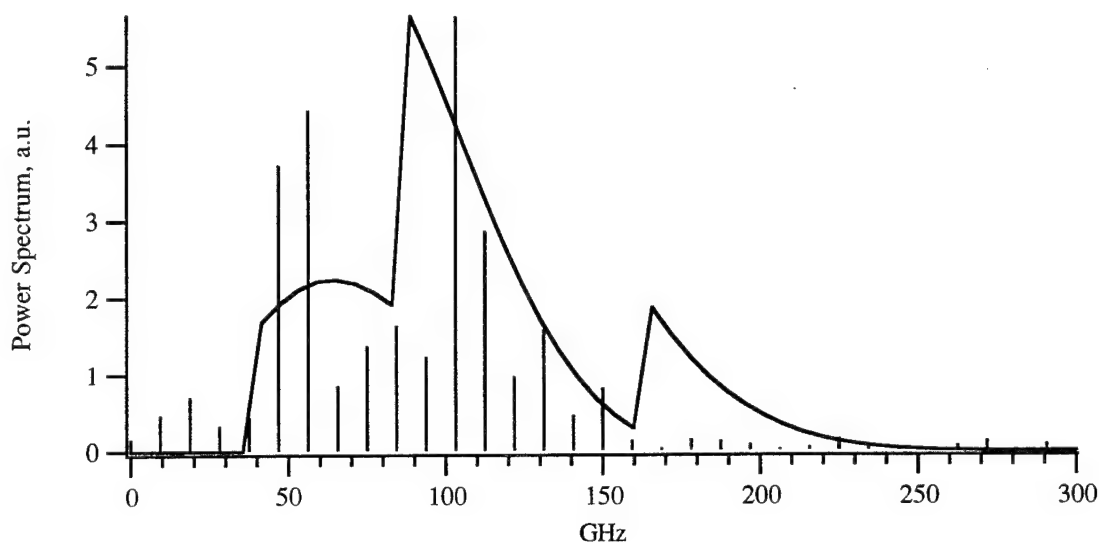
Fig. 4-23. Spectrum of PEBS signal from electron beam crossing "large" waveguide. Array of lines from zero is spectrum calculated from measured data in figure 4-22. Solid line is predicted spectrum of the system response of the large waveguide and the FTS.

4.3.2 Electron Beam Variation Measure by FTS

As another test of the ability of the FTS to measure changes in electron bunch width, the PEBS alpha magnet setting were changed while monitoring the electron bunch width. Alpha magnet adjustments changed the electron bunch momentum spread and, hence, the electron bunch duration. Figure 4-24 shows the net effect on the measured bunch length versus momentum spread. The FTS clearly resolves a reduction in pulse width as the momentum spread is decreased (small MF numbers). The pulse width changes from approximately 1.5 pS to over 5 pS due to momentum filter changes.
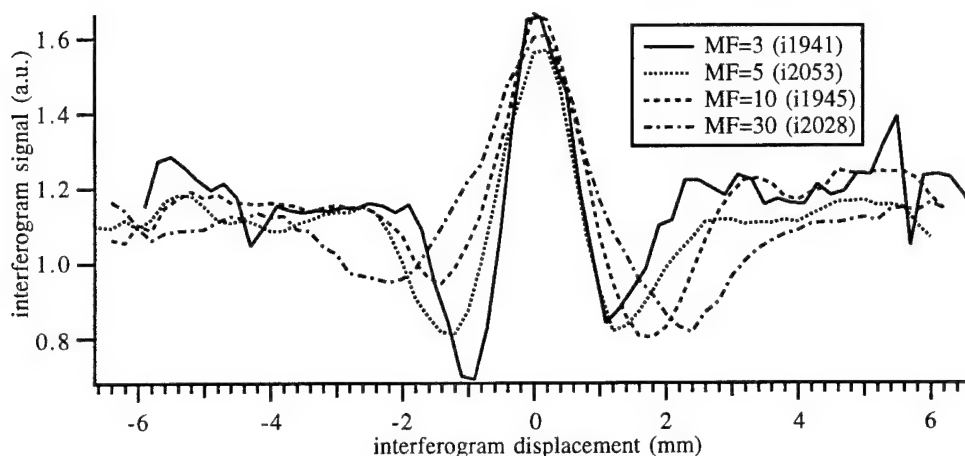
Fig. 4-24. Measurement of electron bunch duration versus momentum spread in PEBS. Smaller MF values indicate smaller momentum spread.

4.4 Heterodyne Spectrum Analyzer Measurements

Heterodyne detection is another alternative approach to measuring RF spectra. Heterodyne detection yields much higher spectral resolution. However, this technique requires a local oscillator (LO) signal at or near the frequency of interest; at millimeter and submillimeter frequencies stable oscillators of sufficient power are not common. Nonetheless, commercial spectrum analyzers now have LOs that operate to 40 GHz (and beyond with external mixers). A Tektronix model 2784 spectrum analyzer [Tektronix, 1993] †† characterized the electron beam transient. This analyzer measures signals from 10 Hz to 40 GHz in coax with programmable resolution bandwidth from 3 Hz to 10 MHz. Although external mixers can extend the range of this instrument to > 300 GHz, these were not available for this study.

The transient signal was focused into an X-band horn and waveguide to type-N transition. The signal was brought through ≈75 cm of type RG-9B/U 50 Ω coaxial cable the spectrum analyzer input. Figure 4-25 shows the results of spectral scans at various

†† We would like to thank Don Fritch and Bob Rodriguez of Tektronix for their generous loan of this equipment.

harmonics of the FEL drive klystron frequency. All measurements were taken with 30 kHz resolution bandwidth and 20 second full scan duration.

The various data clearly show the pulse train structure convolved about the pulse repetition frequency. The measurement at 8.570 GHz is below the X-band horn cutoff, and hence is of lower power. At frequencies above 25 GHz, the spectrum analyzer shows signal only slightly above the noise floor. This drop in signal is assumed to be due to poor matching into the X-band horn and coaxial transition.

Although this data does not reveal any added information about the electron bunch structure, it does show that heterodyne detection is a usable alternative to the other techniques discussed in this paper. With appropriate external mixers, heterodyne detection should provide signal characterization to beyond 300 GHz. Also, if the LO is phase locked to a known phase reference, it should be possible to down convert the transient signal and measure its relative phase. With both the phase and the amplitude information, heterodyne detection would be able to totally characterize the frequency domain transient signal. Fourier transforming this information would give a true indication of the time domain electron transient and generating bunch shape.
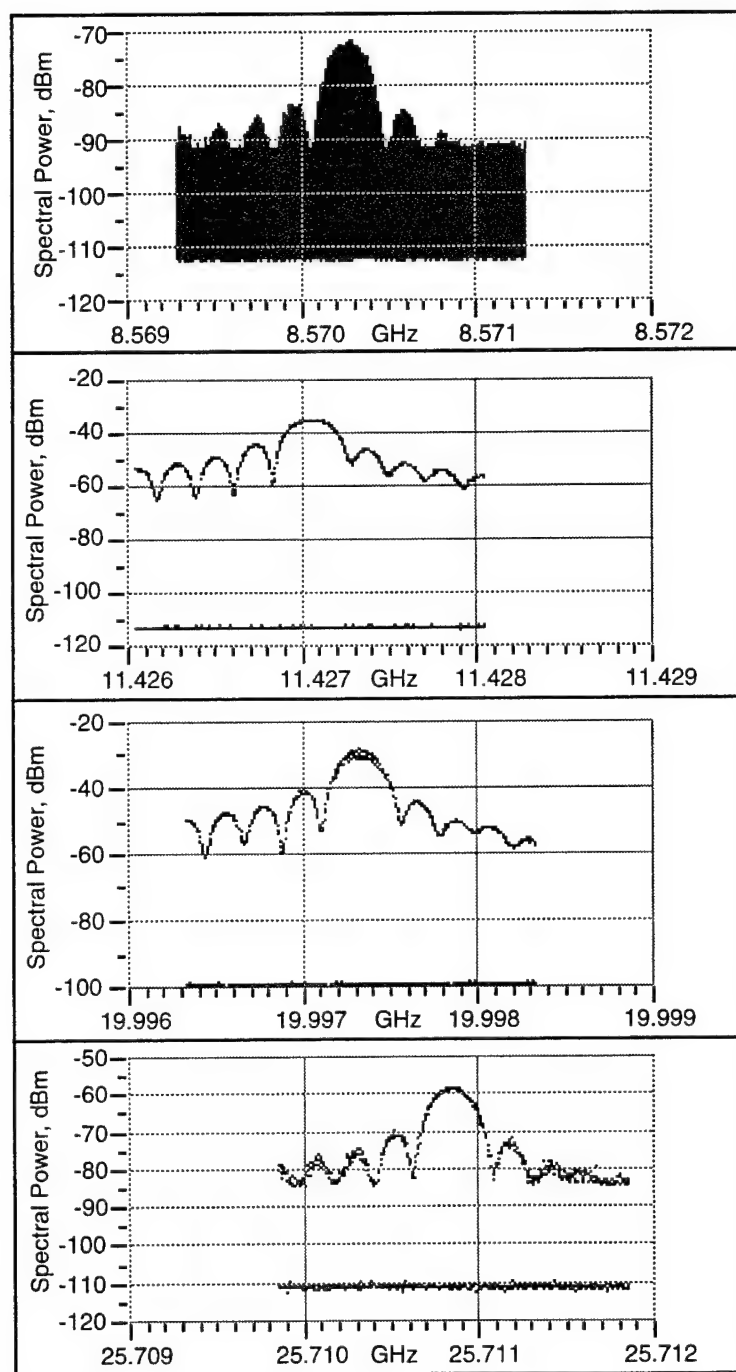
Fig. 4-25. Spectrum analyzer measurement of electron beam transient signal. Spectrum analyzer resolution bandwidth was 30 kHz for all measurements.
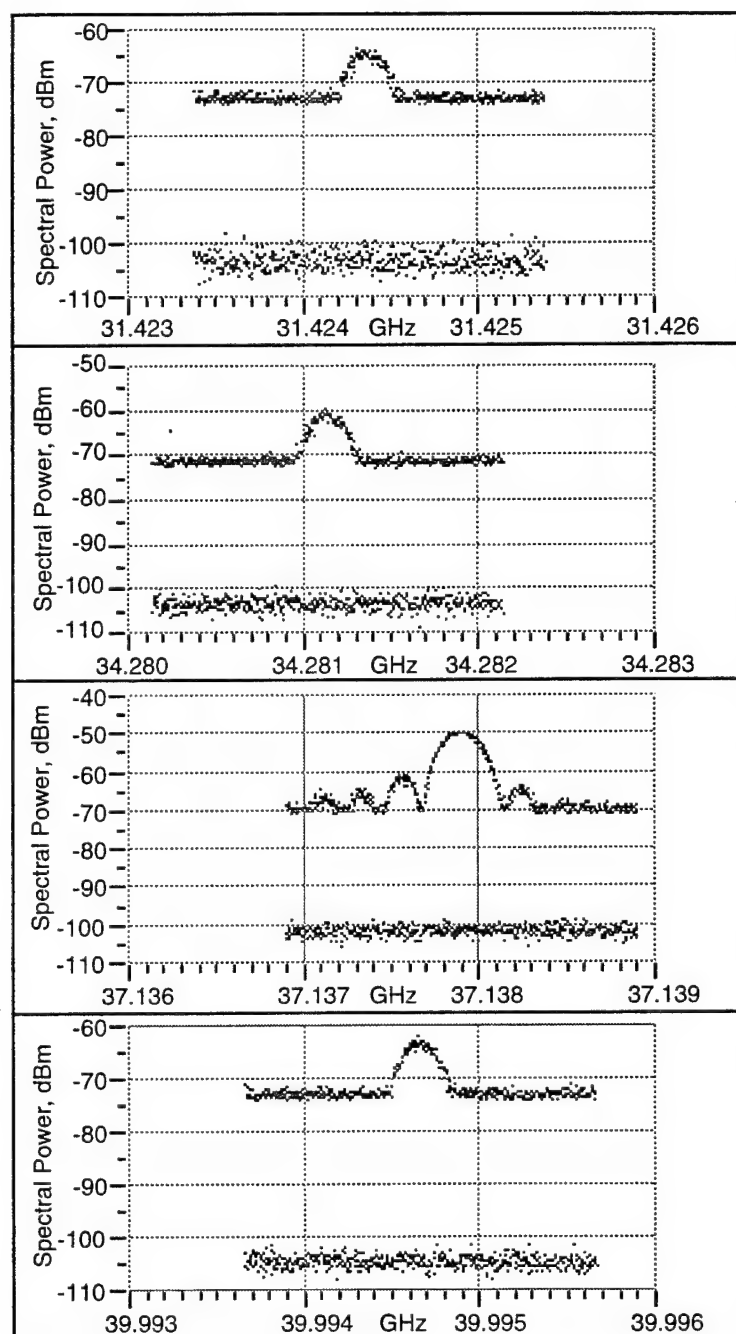
Fig. 4-25, continued.

4.5 Summary

The data presented in this chapter shows that the FTS is capable of measuring the power spectrum of the transient produced by a relativistic electron bunch. Based on that spectrum, the temporal profile of the transient and the electron bunch is estimated. FTS works as an electron bunch autocorrelator, with enough resolution to monitor bunch changes from beginning to end of macro pulse. This overall technique has been used successfully on both the Mark III FEL and the PEBS project at Duke. In addition to characterizing the electron beam, this chapter has shown the validity of a more detailed analysis of millimeter wavelength waveguide excitation by electron beams.

Chapter 5
Future Research

This dissertation has reviewed all the work done to present studying the bunched electron beams. Because the results have been very encouraging, we are planning future experiments and refinements to the current technique. This section describes these future projects.

5.1 Basic FTS improvements

Having used the current FTS for almost a year, we have discovered several system limitations that can be improved. First, the DSO configuration limits overall FTS sample rate to approximately one sample per second, although the FEL generates 10 macro pulses per second (the limiting data collection rate). There are a couple of reasons for this bottleneck. First, the DSO cannot be configured to return a sample from a single time bin. Therefore, to sample the macro pulse, the scope is configured to sample a short period (e.g., 50 nS) at the appropriate place in the macro pulse, average the samples, and return the single average value. This entire process takes about a half second, and as a result, one interferogram point is taken for every 5 to 10 FEL macro pulses. This entire process could be improved if instead of an oscilloscope a transient digitizer with independent clock input were used. Such a system could be configured to sample during a macro pulse after translation of the interferometer arm. An alternative approach to using a transient digitizer would be to use a sample and hold IC and the A/D in the Macintosh computer. A fairly simple timing circuit would allow sampling at multiple times during the macro pulse, allowing real time study of the macro pulse evolution. In either approach the time to translate the interferometer mirror would limit overall system measurement rates. Another alternative would be to use a DSO with

deep, partitioned memory. Such a device could be configured to digitize entire macro pulses, following every interferometer mirror translation. The oscilloscope would operate independent of the FTS stepper controller, and only after the entire data scan would all data be downloaded to the computer. This approach would allow simple analysis of the electron bunch evolution during a full macro pulse.

The current translation system in the FTS is slower than necessary due to the use of a fine threaded lead screw in the translation stage. The current lead screw has 10 threads per millimeter. This screw is driven by a stepper motor with 200 steps per revolution. Because the current software implementation of the stepper driver can only generate ≈ 50 steps per second, the overall translation rate is limited to ≈ 250 μm/s. This rate can be improved by redesigning the stepper motor interface, and using a hardware implementation of the software driver. This is a relatively simple project which would require a few counter ICs and a simple state controller. Ideally, the timing of the stepper controller would be synchronized with the data sampling hardware so that once begun, mirror translation and data sampling could be done without software intervention.

Improving the FTS spectral response, would improve the temporal resolution of the system. Because the teflon and TPX optics are fairly lossy at higher frequencies, they should be replaced. Off axis paraboloid mirrors would be ideal replacements for the TPX lenses. Polyethylene or quartz windows would be excellent materials to replace the teflon windows used in the system. Implementation of both these solutions should reduce frequency dependent system losses, flatten the FTS response below 1 THz, and extend response beyond 2 THz.

Another problem related to the spectral response of the system is the periodic spectral response due to beam splitter etaloning. This problem can be overcome by replacing the mylar beam splitter with a wire mesh beam splitter, and replacing the

mirrors with retro-reflectors. This type of arrangement is used in the Grubbs-Parson Fourier transform spectrometer, and has a flat spectral response from $\approx$DC to 40 cm^{-1}. Implementing this solution would simplify the deconvolution of the system response from the signal.

Future experiments should also have a second broad band detector so that power fluctuations and spurious signals could be canceled from the interferometer signal. One approach to this problem, would use a second InSb detector and beam splitter to sample a portion of the incoming signal. This should give excellent operational results but adds a second liquid helium dewar to the overall system complexity. An alternative possible approach would be to redesigned electron beam monitor, so that it works over a wider microwave frequency range. Using two of these monitors, on either side of the electron beam, should allow cancellation of beam position changes.

Finally, a redesigned FTS would incorporate better grounding and RF shielding. In the current detector system, shielding and grounding were added only after interference and noise sources were discovered. A redesign would integrate the shielding with the design. In addition, all unused surfaces in the interferometer, should be covered with microwave absorbing material, so as to reduce EM transient echoes and spurious pickup by the InSb detector.

5.2 Alternative Measurement Techniques

Although the basic FTS proves in principle the validity of this technique, the basic FTS system suffers from being large and complicated. This section presents several alternative methods of implementing frequency domain techniques to measure picosecond electron bunches.

The simplest approach to making broad band power spectrum measurements is to have an array of detectors and filters, each sensitive to a different frequency range. Although a variety of detector technologies exist for MMSMM detectors, the simplest

approach would be to use GaAs Schottky diodes mounted at the end of waveguide filters. Such a system could have 5-10 bands, from 100 to 1000 GHz. Data from each receiver would be sampled in parallel, at the macro pulse generation rate. Because these detectors usually have high video bandwidth (> 100 MHz), real time pulse evolution could be measured across the pulse train. Because the detectors are easily damaged by radiation, considerable shielding would be required if this approach were used on the Mark III. Another drawback to this approach is expense; commercial detectors cost ≈$1000 a piece. An alternative to using an array of filters is to use a grating.

Another approach would be to use a interferometer implemented entirely in waveguide or planar transmission line. In this approach, the transient signal would be split onto two transmission lines or waveguides. One would have a fixed length while the either would have an adjustable electrical length. The signal would be recombined and the signal brought to a detector (any implementation of a broad band detectors would work). As the electrical length of the adjustable is varied, the output from the detector would yield the autocorrelation of the transient. To implement this system, one must be aware of the following problems. First, the adjustable length arm must produce a linear phase shift independent of frequency. The free space Michelson interferometer does this, however, near cutoff a waveguide implementation would see a frequency dependent phase shift, which would complicate the output signal and not yield an accurate autocorrelation.

An obvious problem inherent with autocorrelation/power spectrum techniques is that all phase information is lost. To obtain the phase information the transient must be sampled directly. As mentioned in §1.3.1 sampling systems with sub-picosecond time resolution are available. The fastest of these systems are driven by a femtosecond pulsed laser, whose output generates and synchronizes the events under study.

Unfortunately it is difficult to synchronize a femtosecond laser (typically operating at repetition rates of ≈100 MHz) directly to the klystron of the FEL (operating at ≈3 GHz). Currently, much research is focused on the synchronization problem. One possible solution is to use the doubled (or tripled) optical output from the FEL as the pulsed laser signal. Another solution to this problem is to use non-linear transmission line based systems [Marsland, et al., 1989; Van Der Weide, et al., 1992] , although their resolution is not as good as the femtosecond based approach.

An alternative approach to sampling is to use a heterodyne detection to demodulate the high frequency components of the transient. This project has shown that a 40 GHz spectrum analyzer has sufficient sensitivity to measure the low frequency spectrum. It would be simply a matter of obtaining the appropriate high frequency mixers to extend this measurement to high frequencies. Because heterodyning preserves phase, the phase of the individual spectral components could be measured by using a local oscillator with known phase and appropriate sampling hardware.

5.3 New Experiments

Without even modifying the current FTS equipment, a variety of new experiments should be tried. First, electron beam pickups should be inserted at other points along the beam line so that electron bunch evolution versus displacement can be studied. At very least, a pickup should be placed after the FEL wiggler, so post-wiggler electron bunches can be studied. Because the optical field in wiggler is thought to modulate the electron bunch, it is possible that a post-wiggler monitor will see radiation beyond that due to just the micro bunch structure.

After passing through the FEL, the electron bunches are dumping into the ground. Although not currently characterized, these electron bunches should still be short pulses, and useful for other applications. [Wang and Sessler, 1993] has used periodic structure as a means for coupling energy off a similar type of electron beam. This

experiment should be duplicated and extended using different types of interaction devices. Currently much effort is being devoted to designing appropriate interaction devices.

Finally, a series of experiments should be planned to measure the absolute power in contained in the transient produced by the electron bunches. Bunched electron beam systems would make excellent spectroscopic sources, and should have enough power to perform studies in the non-linear microwave behavior of materials. Also because the FEL optical output and the electron bunch transient are synchronized, pump-probe experiments using combined optical and millimeter/sub-millimeter radiation are possible.

Chapter 6
Conclusions

In summary, this project has demonstrates a variety of techniques for measuring the pulse length of relativistic, bunched electron beams. The Fourier transform spectrometer used in this work measured electron bunches with picosecond duration. The power spectra of these signals extends over 500 GHz. Based on the FTS response and the measured signals, pulse shapes have been estimated for the electron bunches. The current pulse shape estimates are limited due to the complicated spectral response resulting from frequency dependent losses in the FTS. Nonetheless, models indicate the pulse is not purely rectangular, but more rounded like a truncated inverted parabola.

We have also shown that the FTS is capable of resolving electron beam changes on both a day-to-day and minute-to-minute basis. Although the technique needs some refinement, we showed that electron bunches near the beginning of a macro pulse have different characteristics than bunches near the end of the macro pulse. Also we demonstrated that a simple high frequency detector can indicate electron bunch variations during the generation of a single macro pulse.

Finally, we have highlighted the limitations of the current measurement system implementation, and suggested improvements. In addition we have presented future areas for research.

Appendix 1 - Software models

The simulations for this project were done using the software package,

NumberCrunchII [Mahoney, 1993]. NumberCrunchII is a general purpose

computational environement much like Mathematica. Unlike Mathematica, it is small,

quick, and does not support symbolic computations. NumberCrunchII does handle

complex numbers, matrices, FFTs, and functional definitions, and is easy to learn. The

following listing are for the frequency domain filtering and analysis that generated the

pulse simulations and FTS system response models.

General Definitions

```
? # This is a test of the effect of high pass filtering on the autocorr sig. from the mark III
? #Basic Definitions
? gauss(x,t) = exp(-(x/t)^2);
? pS = 1e-12; GHz = 1e9; THz=1e12; mm = 1e-3;
? FixRoundOff(xx)=(xx+1)-1;FixRO(xx)=(xx+1)-1;
? # delF is passed the delta time increment per bin and the number of bins
? # and computes the size of delta F in the freq dom.
? delF(delT,numBin) = 1/(delT*numBin);
? delF(320/300 pS,1024)/GHz # should yield .9155 GHz
? # negF computes the neg ost freq bin inthe dom rep of an array
? negF(delT,numBin)= -delF(delT,numBin)*(numBin/2);
? negF(320/300 pS,1024)/GHz # should yield -468.75
? # freqArray returns an array containing the freq of each bin
? freqArray(negF,dF,numpts) = negF+(dF*[0..(numpts-1)]);
? # timeArray returns array of time values of width dT symetric with t=0 in the middle
? timeArray(dT,numpts)= dT*([0..(numpts-1)] - numpts/2);
? # timeArray(.1,8) #=> [-0.4, -0.3, -0.2, -0.1, 0, 0.1, 0.2, 0.3]
? # highpass returns 1 in the position of an array when |x[n]| >= fc, else it returns zero
? highpass(xarr,fc) = sign(sign(FixRoundOff(|xarr| - fc))+1);
? HighPass([-4..4],2) #returns [1, 1, 1, 0, 0, 0, 1, 1, 1]
? #lowpass returns an array with 1 at n, when |x[n]| <= fc, else 0
? LowPass(xarr,fc) = sign(sign(FixRoundOff(fc -|xarr|))+1);
? #LowPass([-4..4],2) #returns [0, 0, 1, 1, 1, 1, 1, 0, 0]
? Re(x)=Real(x);Im(x)=Imaginary(x);
```

Pulse Filtering Formulae

```
? # fftgp1=FFT(swapsides(gp1));
? # define the delT and numpts in this experiment:
? delT = .2 pS; numpts = 512;sqrnpts=sqrt(numpts);
?
? # now define the basic pulse shape and the freq array
? gT = FixRO( gauss(timearray(delT,numpts),.8 pS)); # note t=0 in array center...
? gF = FFT(swapsides(gT))*sqrt(numpts); # this is f=0 at gF[1]...
```

? gNegF = negF(delT,numpts); gDelF = delF(delT,numpts);
? gFreqs = freqArray(gNegF,gDelF,numpts); # freq=0 in array center...
? # Now lets apply a high pass filter to the signal
? gT2 = swapsides(InvFFT(swapsides(highpass(gFreqs,30 GHz))*gF/sqrt(numpts))); #
? gT2 = swapsides(InvFFT(|swapsides(highpass(gFreqs,70 GHz))*gF|^2));
#Autocorrelation
?
? #Note, that FFT(highpass) picks up a sqrt(numpts) to maintain total energy equality;
? #this cancels with sqrt(numpts in denominator and Acorr is scaled correctly...
? #Scaling relationships:
? sum(|gT|^2)
  5.0132565
?sum(|gF|^2)
  5.0132565
? sum(|highpass(gFreqs,30 GHz)|^2)
  505
? sum(|InvFFT(highpass(gFreqs,30 GHz))/sqrt(numpts)|^2)
  505
?
? #Defining a rect pulse
? rT = FixRO(lowpass(timearray(delT,numpts),.41 pS)); # note t=0 in array center...
? rF = FFT(swapsides(rT))*sqrnpts; # this is f=0 at gF[1]...
? rT2 = swapsides(InvFFT(|swapsides(highpass(gFreqs,150 GHz))*gF|^2)); #Autocorr

Waveguide Higher Order Mode Analysis
? Real1n(f,n,tt,tp) =((cos((nπ/2) - (π*f*(tt+tp))) - cos((nπ/2) - (π*f*(tt-tp))))/ ((2*π*f*tp)*(n*π - 2πf*tt))) + ((-cos((nπ/2) + (π*f*(tt+tp))) + cos((nπ/2) + (π*f*(tt-tp))))/ ((2*π*f*tp)*(n*π + 2πf*tt))) ;
? ReS1(f,tp)=(Real1n(f,0,6 pS,tp) * step(f,39.5 GHz)) + (Real1n(f,1,6 pS,tp) * step(f,88.22 GHz)) + (Real1n(f,2,6 pS,tp)*step(f,162 GHz));
?
? step(x,co)=sign(sign(x-co)+1); #this returns 0 if x<= co and 1 for x> co
? HOMf = ReS1(|gFreqs+.1|,3 pS);
? swapsides(HOMf)
  [0, 0.99296, … ,0.97205, 0.99296]
? HOMt = swapsides(InvFFT(swapsides(|HOMf|^2)/sqrt(numpts))); #wg response
? HOMt = swapsides(InvFFT(swapsides(| HOMf*FTSBB((|gFreqs|),.025,1.69) |^2)));
#wg response with bs and InSb
?

FTS and InSb Response Models
? # Now add in response of bs and InSb
? # This is beamsplitter models based on J. E. Chamberlain, et al, Infrared Physics,
? # vol. 6, pp. 195-203 (1966); all this copied from earlier NC version file BS#2 models
? # the actual dissertation plots were overlaid with the actual data in igor
? Deg2Rad(x) = x * π/180;
? ai=Deg2Rad(45); # This sets the angle of incidence
? R1=1;R2=1;nt=1.69; # mirror reflectivity, and BS index
? at=asin(sin(ai)/nt); #ai
? Rp=(sin(ai-at)/sin(ai+at))^2; #ai

```
? tp=1-Rp; #ai
? Rs=(tan(ai-at)/tan(ai+at))^2; #ai
? ts=1-Rs; #ai
? E(h,k,n)=4*(sin(2*π*h*k*n*cos(at)))^2;
? T_p(h,k,n)=2*((R1*R2)^0.5)*(Rp*tp*tp*E(h,k,n))/(tp*tp+(Rp*E(h,k,n)))^2;
? T_s(h,k,n)=2*((R1*R2)^0.5)*(Rs*ts*ts*E(h,k,n))/(ts*ts+(Rs*E(h,k,n)))^2;
? TT(h,k,n)=0.5*(T_p(h,k,n)+T_s(h,k,n)); #h in units of cm, k in cm-1,
? T_p(0.01,1,1.69)
  0.0133766
? GHz = 1e9; cm= 0.01;
?
? # this is model of detector response based on QMC data
? # sheet stating InSb bolometer is flat out to 600 GHz then has f^-2 rolloff to ≈3THz
?  InSbRes2(f) = 1/(1+ ((f)/(600 GHz))^5 );
? FTSBB(f,h,n) = (InSbRes2(f) * TT(h,f/(30 GHz),n)); # response for thck h, BS index
n
? FTSBB(lgFreqsl,.025,1.69)
  [ 2.3844e-4,  2.3803e-4, … , 2.3602e-4,  2.3803e-4]
?
```

References

J. A. Alvarez, R. E. Jennings and A. F. M. Moorwood, "Far infrared measurements of selected optical materials at 1.6°K.," Infrared Physics, **15** 45-9 (1975).

Analog Devices, "AD595 monolithic thermocouple amplifier with cold junction compensation data sheet," Analog Devices

Anon., "Entire Issue: 9th Int. FEL Conference, 1987," Nuclear Instruments and Methods in Physical Research, **A272** 1-610 (1988).

D. H. Auston, "Impulse response of photoconductors in transmission lines," IEEE Journal of Quantum Electronics, **QE-19** 639-48 (1983).

D. H. Auston, "Picosecond photoconductors: physical properties and applications" in Picosecond optoelectronic devices, ed. 73-117 (New York, Academic Press, 1984).

D. H. Auston, "Ultrafast Optoelectronics" in Ultrashort Laser Pulses and Applications, ed. W. Kaiser, 183-233 (New York, Springer-Verlag, 1988).

D. H. Auston and M. C. Nuss, "Electrooptic Generation and Detection of Femtosecond Electrical Transients," IEEE Journal of Quantum Electronics, **24** 184-197 (1988).

D. H. Auston and P. R. Smith, "Generation and detection of millimeter waves by picosecond photoconductivity," Appl. Phys. Lett., **13 (7)** 631-633 (1983).

M. R. Baggs, R. T. Eagles, W. Magulis, W. Sibbett and W. E. Sleat, "Subpicosecond chronoscopy using a Photochron IV Streak Camera," in Advances in Electronics and Electron Physics, ed. B. L. Morgan (London, Academic Press, 1985).

R. J. Bell, Introductory Fourier Transform Spectroscopy. Academic Press, New York: 1972.

S. V. Benson, J. M. J. Madey, J. Schultz, M. Marc, W. Wadensweiler, G. A. Westenskow and M. Velghe, "The Stanford Mark III Infrared Free Electron Laser," Nuclear Instruments and Methods in Physics Research, **A250** 39-43 (1986).

S. V. Benson, J. Schultz, B. A. Hooper, R. Crane and J. M. J. Madey, "Status Report on the Stanford Mark III Infrared Free Electron Laser," Nuclear Instruments and Methods in Physics Research, **A272** 22-8 (1988).

R. Bergere, A. Veyssiere and P. Daujat, "Linac Beam Position Monitor," Review of Scientific Instruments, **33** 1441-9 (1962).

P. Bhartia and I. J. Bahl, Millimeter Wave Engineering and Applications. John Wiley & Sons, New York: 1984.

M. G. Billing, "Beam Position Monitors for Storage Rings," Nuclear Instruments and Methods in Physics Research, **A266** 144-154 (1988).

J. M. Blea, W. F. Parks, P. A. R. Ade and R. J. Bell, "Optical properties of black polyethylene from 3 to 4000 cm-1," Journal of the Optical Society of America, **60** 603 (1970).

J. Bouchert, R. Dorsinville, P. Delfyett, S. Krimchansky and R. R. Alfano, "Determination of temporal correlation of ultrafast laser pulses using phase conjugation," Optical Communications, **52** 433-7 (1985).

R. W. Boyd, Radiometry and the detection of optical radiation. John Wiley & Sons, New York: 1983.

C. A. Brau, "Free-Electron Lasers," in Advances in Electronics and Electron Physics, ed. P. W. Hawkes (Boston, Academic Press, 1990).

E. L. Brodsky, K. J. Klemen, G. Rogers, D. Rioux, R. Patel and H. Hochst, "Implementation and test of a synchrotron radiation position monitor at a user beam line," Rev. Sci. Instrum., **63** 519-522 (1992).

A. B. Bronwell and R. E. Beam, Theory and Application of Microwaves. McGraw-Hill, New York: 1947.

J. E. Chamberlain, G. W. Chantry, F. D. Findlay, H. A. Gebbie, J. E. Gibbs, N. W. B. Stone and A. J. Wright, "The Spectral Transmission at Infra-red Wavelengths of Michelson Interferometers with dielectric film beam-dividers," Infrared Physics, **6** 195-203 (1966).

G. W. Chantry, Submillimetre Spectroscopy. Academic Press, London: 1971.

G. W. Chantry, H. M. Evans, J. W. Fleming and H. A. Gebbie, "TPX, a new material for optical components in the far infrared spectral region," Infrared Physics, **9** 31-3 (1969).

G. W. Chantry, J. W. Fleming, E. A. Nicol, H. A. Willis and M. E. A. Cudby, "Temperature effects and the observation of lattice bands in the far infrared spectrum of polytetraflouroethylene," Chemical Physics Letters, **16** 141-4 (1972).

G. W. Chantry, J. W. Fleming and P. M. Smith, "Far infrared and millimetre-wave absorption spectra of some low-loss polymers," Chemical Physics Letters, **10** 473-7 (1971).

P. D. Coleman, "Theory of the rebatron - a relativistic electron bunching accelerator for use in megavolt electronics," Journal of Applied Physics, **28** 927-35 (1957).

P. D. Coleman and M. D. Sirkis, "The harmodotron - a beam harmonic, higher-order mode device for producing millimeter and submillimeter waves," Journal of Applied Physics, **26** 1385-6 (1955).

R. E. Collin, Field Theory of Guided Waves. McGraw-Hill, New York: 1960.

R. E. Collin, Foundations for microwave engineering. McGraw-Hill, New York: 1966.

J. Connes, "Recheches sur la spectroscopie par transformation de Fourier," Revue D'Optique: Théorique et Instrumentale, **40** 45-79,116-140,171-190,231-265 (1961).

J. Connes and P. Connes, "Near-infrared planetary spectra by Fourier spectroscopy - I. Instruments and Results," Journal of the Optical Society of America, **56** 896-910 (1966).

R. W. Coombes and D. Neet, "Beam Monitors Based on Light Observation for the Beam Switchyard of the Stanford Two-Mile Linear Accelerator," IEEE Transactions on Nuclear Science, **14** 1111-1115 (1967).

F. C. De Lucia, "The generation of near millimeter radiation by picosecond pulse demodulation," Final Report DAAK70-79-C-0121; U.S. Army Night Vision and Electro-Optics Laboratory, Fort Belvoir, Virginia (1983).

F. C. De Lucia, B. D. Guenther and T. Anderson, "Microwave generation from picosecond demodulation sources," Applied Physics Letters, **47** 894-6 (1985).

J.-C. Denard, G. Oxoby, J.-L. Pellagrin and S. Williams, "Monitoring of the Stanford Linac Microbunches' Position," IEEE Transactions on Nuclear Science, **NS-30** 2364-2366 (1983).

A. G. Doukas, J. Bouchert and R. R. Alfano, "Picosecond laser techniques and design" in Biological Events Probed by Ultrafast Laser Spectroscopy, ed. 387-415 (London, Academic Press, 1982).

H. A. Enge, "Achromatic Magnetic Mirror for Ion Beams," The Review of Scientific Instruments, **34** 385-389 (1963).

H. Everitt and J. Hensley, MacStew Macintosh program, (Physics - Duke University, 1989).

E. V. Farinholt, Z. D. Farkas and H. A. Hogg, "Microwave Beam Position Monitors at SLAC," IEEE Transactions on Nuclear Science, 1127- 1131 (1967).

J. A. Giordmaine, P. M. Rentzepis, S. L. Shapiro and K. W. Wecht, "Two photon excitation of flourescence by picosecond light pulses," Applied Physics Letters, **11** 216-8 (1967).

M. J. E. Golay, "A pneumatic infra-red detector," Rev. Sci. Instr., **18** 357-62 (1947a).

M. J. E. Golay, "Theortetical consideration in heat and infra-red detection, with particular reference to the pneumatic detector," Rev. Sci. Instr., **18** 347-56 (1947b).

M. J. E. Golay, "The theoretical and practical sensitivity of the pneumatic infra-red detector," Review of Scientific Instruments, **20** 816-20 (1949).

B. I. Greene, J. F. Federici, D. R. Dykaar, R. R. Jones and P. H. Bucksbaum, "Interferometric characterization of 160 fS far-infrared light pulses," Applied Physics Letters, **59** 893-5 (1991).

W. M. Grove, "Sampling for oscilloscopes and other RF systems: DC through X-band," IEEE Trans. on Microwave Theory and Technique, **MTT-14** 629-35 (1966).

R. D. Guenther, Modern Optics. John Wiley & Sons, New York: 1990.

Hewlett-Packard, Test and Measurement Catalog. Hewlett-Packard, Santa Clara, CA: 1993.

J. Holton, Personal Communication, 22 March 1993.

S. P. Jachim, R. C. Webber and R. E. Shafer, "An RF Beam Position Measurement Module for the Fermilab Energy Doubler," IEEE Transactions on Nuclear Science, **NS-28** 2323-2325 (1981).

J. D. Jackson, Classical Electrodynamics. John Wiley & Sons, New York: 1975.

K. W. Johnson and J. F. Rabolt, "Far infrared measurements on the 19°C phase transition in polytetraflouroethylene," Journal of Chemical Physics, **58** 4536-8 (1973).

C. R. Jones, M. J. Peters and J. M. Dutta, "A compact relativistic electron beam source for generation of far infrared radiation," Proc. SPIE-The International Society for Optical Engineering, Conference Digest: 17th International Conference on Infrared and Millimeter Waves - 1992).

I. F. Kaufman and P. D. Coleman, "Design and evaluation of an S-band rebatron," Journal of Applied Physics, **28** 936-944 (1957).

K. J. Kleman, "Beam Diagnostics and Control at Aladdin," Nuclear Instruments and Methods in Physics Research, **A266** 172-176 (1988).

S. M. Kogan, "A photoconductivity theory based on variations of carrier mobility," Soviet Physics - Solid State, **4** 1386-9 (1963).

M. Kominami, D. M. Pozar and D. H. Schaubert, "Dipole and slot elements and arrays on semi-infinite substrates," IEEE Transactions on Antennas and Propagation, **AP-33** 600-7 (1985).

B. Kulke, H. Shay, F. Coffield, R. Frye and R. Holmes, "A Compact Beam Position Monitor for Use Inside a Free Electron Laser Wiggler," Nuclear Instruments and Methods in Physics Research, **A272** 241-246 (1988).

J. Mahoney, NumberCrunchII program, (Windham Software, PO Box 347, Marlboro VT, 05344, 1993).

S. Majumdar, P. Y. Key, M. Yaschelev, Y. Surdyuchenko, W. Seka, M. C. Richardson, P. Yaanimagi and R. Keck, "Evaluation of PV001 and P-100 tubes for multiple channel streak cameras," in Advances in Electronics and Electron Physics, ed. P. W. Hawkes (London, Academic Press, 1988).

R. A. Marsland, V. Valdivia, C. J. Madden, M. J. W. Rodwell and D. M. Bloom, "130 GHz GaAs monolithic integrated circuit sampling head," Applied Physics Letters, **55** 592-4 (1989).

D. H. Martin, "Polarizing (Martin-Pulpett) Interferometric spectrometers for the near- and submillimeter spectra," in <u>Infrared and Millimeter Waves</u>, ed. K. Button (New York, Academic Press, 1982).

J. Merkelo and R. D. Hall, "Broad-band thin-film signal sampler," IEEE Journal of Solid-State Circuits, **SC-7** 50-4 (1972).

H. Motz, "Application of the radiation from fast electron beams," Journal of Applied Physics, **22** 527-35 (1951).

H. Motz and K. B. Mallory, "Generation of submillimeter waves," Journal of Applied Physics, **26** 1384 (1955).

H. Motz, W. Thon and R. N. Whitehurst, "Experiments on radiation by fast electron beams," Journal of Applied Physics, **24** 826-33 (1953).

R. B. Neal, "The Stanford Two Mile Accelerator," in , ed. (New York, W. A. Benjamin, Inc, 1968).

R. C. Ohlmann, P. L. Richards and M. Tinkham, "Far Infrared Transmission through Metal Light Pipes," Journal of the Optical Society of America, **48** 531-3 (1958).

B. Peterson, "Spectrum Analysis Basics," Application Note #150 (PN 5952-0292); Hewlett-Packard (1 November 1989).

E. H. Putley, "Far infra-red photoconductivity," Physica Status Solidi, **6** 571-614 (1964).

E. H. Putley, "InSb submillimeter photoconductive detectors" in <u>Semiconductors and Semimetals</u>, ed. R. K. Willardson, 143-68 (new York, Academic Press, 1977).

QMC Instruments Ltd., "Data sheet for Type QFI/2 & QFI/3 InSb Hot Electron Detector System," in (1992).

S. Ramo, J. R. Whinnery and T. Van Duzer, <u>Fields and waves in communications electronics</u>. John Wiley & Sons, New York: 1984.

B. V. Rollin, "Detection of millimetre and sub-millimetre wave radiation by free carrier absorption in a semiconductor," Proceedings of the Physical Society (London), **77, pt. 5** 1102-3 (1961).

K. Sakai and J. Sakai, "Characteristics of n-InSb hot electron submillimeter detector," Japanese Journal of Applied Physics, **15** 1335-41 (1976).

K. L. Sala, G. A. Kenney-Wallace and G. E. Hall, "CW autocorrelation measurements of picosecond laser pulses," IEEE Journal of Quantum Electronics, **QE-16** 990-6 (1980).

R. J. Seymour and R. R. Alfano, "Time resolved measurement of the electron spin relaxation kinetics in GaAs," Applied Physics Letters, **37** 231-3 (1980).

R. E. Shafer, "Characteristics of Directional Coupler Beam Position Monitors," IEEE Transactions on Nuclear Science, **NS-32** 1933-1936 (1985).

L. C. Shen and J. A. Kong, Applied Electromagnetics. Brooks/Cole, Monterey, CA: 1983.

A. P. Sheppard, K. H. Breeden and A. McSweeney, "High resolution submillimeter measurements of atmospheric water vapor absorption" in Proceedings of the Symposium on Submillimeter Waves, ed. J. Fox, 452 (Brooklyn, NY, Polytechnic Press, 1970).

J. C. Sheppard, J. E. Clendenin, M. B. James, R. H. Miller and M. C. Ross, "Real Time Bunch Length Measurements in the SLC Linac," IEEE Transactions on Nuclear Science, **NS-32** 2006-2008 (1985).

K. Shivanandan, D. P. McNutt and R. J. Bell, "Spectral Response of n-type InSb in the sub-millimeter range," Infrared Physics, **15** 27-32 (1975).

J. D. Simpson (conference chair), "1985 Particle Accelerator Conference, Accelerator Engineering and Technology," IEEE Transactions on Nuclear Science, **NS-32** 1880-1950 (1985).

M. D. Sirkis and P. D. Coleman, "The harmodotron - a megavolt electronics millimeter wave generator," Journal of Applied Physics, **28** 944-50 (1957).

F. G. Stremler, Introduction to communication systems. Addison-Wesley, Reading, Massachusetts: 1982.

J. C. Swartz. "Frequency Domain Techniques to Characterize Picosecond Optical Pulses." Masters Degree Thesis, Duke University, 1989.

Tektronix, "Product Catalog," in (1993).

J. A. Valdmanis, "1 THz-bandwidth prober for high-speed devices and integrated circuits," Electronics Letters, **23** 1308-10 (1987).

J. A. Valdmanis and G. Mourou, "Subpicosecond electrical sampling and applications" in Picosecond Optoelectronic Devices, ed. pp. 249-270 (New York, Academic Press, 1984).

J. A. Valdmanis, G. Mourou and C. W. Gabel, "Subpicosecond electrical sampling," Proc. Picosecond Optoelectronics - Proceedings of the SPIE - San Diego, California, (SPIE, 1983).

D. W. Van Der Weide, J. S. Bostak, B. A. Auld and D. M. Bloom, "All-electronic subpicosecond pulses for terahertz signal generation and detection," Proc. SPIE-The International Society for Optical Engineering, Conference Digest: 17th International Conference on Infrared and Millimeter Waves - (SPIE, 1992).

B. C. Wadell, Transmission Line Design Handbook. Artech House, Boston: 1991.

C. Wang and A. M. Sessler, "An efficient microwave power source: The free-electron laser afterburner," J. Appl. Phys., **74** 4840-4844 (1993).

R. K. Wangsness, Electromagnetic Fields. John Wiley & Sons, New York: 1986.

G. A. Westenskow and J. M. J. Madey, "Microwave Electron Gun," Laser and Particle Beams, **2** 223-5 (1984).

D. E. Williamson, "Cone Channel Condensor Optics," Journal of the Optical Society of America, **42** 712-5 (1952).

A. Yariv, Optical Electronics. Holt Rinehart Winston, New York: 1985.

Biography

John C. Swartz was born March 30, 1963 in Chicago, IL. In June, 1985 he received his Bachelor's degree in Electrical Engineering from the Massachusetts Institute of Technology. From 1985 to August 1987 he worked for GenRad Inc. as a digital design engineer on the 2750 project. In September 1987, he entered the Department of Electrical Engineering at Duke University, where in the fall of 1989, he received his Master's degree in Electrical Engineering. His Master's thesis work involved characterizing picosecond optical pulses using frequency domain techniques. His current research involves ultrafast optical systems and millimeter and sub-millimeter microwave systems. He is also involved in the development of an opto-electric devices for ultrasound transducers. He is a member of the IEEE, OSA, and SPIE. Mr. Swartz has published the following papers:

B.D. Guenther, J.C. Swartz, F.C. De Lucia, "Frequency Domain Analysis of the Bunched Relativistic Electron Beam in a Free Electron Laser," Proceedings of the 19th Army Sciences Conference, June 1994, Orlando (US Army, Suffolk, VA).

P.J. Phillips, O.T. Von Ramm, B.D. Guenther, J.C. Swartz, "Optical transducer for reception of ultrasonic waves ," Journal of the Acoustical Society of America **93** (2) 1182-91, February 1993.

B.D. Guenther, J.C. Swartz (preparer), <u>Modern Optics Solutions' Manual</u>, John Wiley and Sons, New York, 1990.

J.C. Swartz, B.D. Guenther, J.M. Dutta, C.R. Jones, W. Guo, F.C. De Lucia, "Pulsed electron beam sources of far infrared radiation," Ohio State University International Symposium on Molecular Spectroscopy, June 14-18,1993, Columbus Ohio.

J.C. Swartz, B.D. Guenther, "Frequency domain techniques for analyzing ultrashort optical pulses," Meeting of the Southeastern Section American Physical Society, 11-13 November 1991, Durham, NC. (Bulletin APS, **36** (10) p.2742, Nov. 1991)

P.J. Phillips, O.T. Von Ramm, B.D. Guenther, J.C. Swartz, "Optical transducer for ultrasound imaging," Meeting of the Southeastern Section American Physical Society, 11-13 November 1991, Durham, NC. (Bulletin APS, **36** (10) p.2742, Nov. 1991)

J.C. Swartz, F. De Lucia, B.D. Guenther, "Applications of Frequency Domain Techniques for Tuning Pulsed Lasers," Proceedings of Topical Meeting on Picosecond Electronics and Optoelectronics, 8-10 March, 1989, Optical Society of America.